A Preliminary Mechanistic Evaluation of PCC Cross-Sections Using ISLAB2000 – A Parametric Study

Neeraj Buch, Ph.D.
Kaenvit Vongchusiri, M.S.

Michigan State University
Department of Civil and Environmental Engineering

Dennis Gilliland, Ph.D**.**

Michigan State University
Department of Statistics and Probability

Thomas Van Dam, Ph.D., P.E.

Michigan Technological University
Department of Civil and Environmental Engineering

Final Report
August 2004

DISCLAIMER

This document is disseminated under the sponsorship of the Michigan Department of Transportation (MDOT) in the interest of information exchange. The MDOT assumes no liability for its contents or use thereof.

The contents of this report may not necessarily reflect the views of the MDOT and do not constitute standards, specifications, or regulations.

1. Report No. Research Report RC-1441	2. Government Accession No.	3. MDOT Project Manager Curtis Bleech, P.E.
4. Title and Subtitle A Preliminary Mechanistic Evaluation of PCC Cross-Sections Using ISLAB2000 – A Parametric Study		5. Report Date August, 2004
7. Author(s) Neeraj Buch, Ph.D., Dennis Gilliland, Ph.D., Kaenvit Vongchusiri, M.S.Thomas Van Dam, Ph.D., P.E.		6. Performing Organization Code
9. Performing Organization Name and Address Michigan State University 3546 Engineering Building East Lansing, MI 48824		8. Performing Org Report No. 61-9522
12. Sponsoring Agency Name and Address Michigan Department of Transportation Construction and Technology Division P.O. Box 30049 Lansing, MI 48909		10. Work Unit No. (TRAIS) 11. Contract Number: 11(a). Authorization Number:
15. Supplementary Notes		13. Type of Report & Period Covered 14. Sponsoring Agency Code

16. Abstract

This report summarizes the impact of structural, environmental and loading factors on jointed concrete pavement responses. The report also highlights the sensitivity of pavement response to the interactions between these factors. As a part of the project, relevant issues that relate the implementation of pavement responses to engineering practice using the ISLAB2000 structural model are also discussed. To this end an experimental matrix was constructed based on the concept of complete factorial for all combinations of design inputs reflecting MDOT practice, climatic condition, and load configurations in Michigan. Several engineering principles and common knowledge were applied to modify the experimental matrix with the purpose of making the matrix more concise, but providing the same level of information. 43,092 combinations of parameters were identified for the preliminary parametric study. The ISLAB2000 structural model was used for the analysis. In addition to the analysis an interpolation scheme was developed to compute mechanistic responses for all combinations of the non-discrete inputs, not addressed in the final experimental matrix.

17. Key Words Pavement response, finite element, axle configuration, lateral support	18. Distribution Statement No restrictions. This document is available to the public through the Michigan Department of Transportation.		
19. Security Classification (report) Unclassified	20. Security Classification (Page) Unclassified	21. No of Pages	22. Price

TABLE OF CONTENTS

Executive Summary……1

Chapter I: Introduction……..4
1.1 Background……4
1.2 Research Objectives……5
1.3 Scope of Research……5
1.4 Organization of Report……..……7

Chapter II: Robustness and User Friendliness of ISLAB2000……9
2.1 Review of Westergaard Theory……..9
2.2 Review of FE Method……..14
2.3 Comparison of Published Results with ISLAB2000 Results……14
2.4 Summary Comparison of Published Results with ISLAB2000 Results……...15
2.5 Summary Comparison of Practical Engineering Results based on ISLAB2000 and EverFE ……17

Chapter III: Experimental Matrix……21
3.1 Data Collection……21
3.2 Preparation of Experimental Matrix……..23
3.3 Final Experimental Matrix……...29

Chapter IV: Parametric Study……30
4.1 Structural Model……...30
4.2 Analysis Process……..31
4.3 Documentation of Analysis Results……..36
4.4 Possible Application of Analysis Results……..46

Chapter V: Interpolation Scheme……47
5.1 Least-Squares Criteria……47
5.2 Development of Interpolation Scheme……48
5.3 Validation and Goodness of Fit……52
5.4 Example Use of Interpolation Scheme……58

TABLE OF CONTENTS
(CONTINUED)

Chapter VI: Potential Implementation of Study Results……..61
6.1 Mechanistic-Empirical Design Concept……61
6.2 Weigh-in-Motion (WIM) Data Synthesis……...64
6.3 Hourly Thermal Gradients……..……67
6.4 Mechanistic-Empirical Procedure for JCP – Example ……69

Chapter VII: Summary of Findings and Recommendations for Future Research ……..87
7.1 Summary of Findings……87
7.2 Recommendations for Future Research……..89

References ……90

Appendices

Appendix A: Review of the Kirchhoff plate theory
Appendix B: Comparison between ISLAB2000 results and Westergaard's solution
Appendix C: ISLAB2000 graphical results for the comparison with Westergaard's solution
Appendix D: Data collection
Appendix E: Validation of thermal strain gradients (the product $\alpha(\Delta T/D)$)
Appendix F: Documentation of pavement response
Appendix G: Impact of lateral placement on different lateral support conditions
Appendix H: Equivalent stress cross-sections
Appendix I: Catalog of pavement response
Appendix J: Hourly load spectra from WIM database
Appendix K: Hourly thermal gradient from EICM
Appendix L: Technology transfer package

LIST OF TABLES

Table 2-1: Required L/l ratio for FE solutions to satisfy Westergaard's assumptions…….….15
Table 2-2: Summary of results and percent variation of the results……..16
Table 2-3: Overall variation between Westergaard and FE solutions……..…….16
Table 3-1: Summary of design parameters from the 14 MDOT designs…….…..22
Table 3-2: Ranges of input parameters obtained from other sources……22
Table 3-3: Final experimental matrix……..…..29
Table 4-1: Summary of critical load locations……...……35
Table 4-2: Summary of interaction between parameters on stresses……...…..44
Table 5-1: Example prediction matrices……...….51
Table 5-2: Comparison of MSE, bias, and variance……..…58
Table 6-1: Summary of single axle load repetitions from SPS-2 section…….…….65
Table 6-2: Summary of tandem axle load repetitions from SPS-2 section……...….65
Table 6-3: Summary of tridem axle load repetitions from SPS-2 section…….……65
Table 6-4: Summary of quad axle load repetitions from SPS-2 section……66
Table 6-5: Summary of multi-axle (5) load repetitions from SPS-2 section……...…..66
Table 6-6: Summary of multi-axle (6) load repetitions from SPS-2 section…….……66
Table 6-7: Summary of multi-axle (7) load repetitions from SPS-2 section…….……67
Table 6-8: Summary of multi-axle (8) load repetitions from SPS-2 section……...……..67
Table 6-9: Design features and material properties for the SPS-2 sections…….…..67
Table 6-10: Seasonal backcalculated k-value obtained from LTPP database……...……68
Table 6-11: Summary of illustrative examples……...……73

LIST OF FIGURES

Figure 2-1: Idealization of dense liquid foundation……...…..9
Figure 2-2: Interior loading condition……..9
Figure 2-3: Edge loading condition……...……10
Figure 2-4: Corner loading condition……11
Figure 2-5: Dual tires simulation represented by a circular loading area…….…….12
Figure 2-6: Effect of temperature gradient on slab curling……..……..13
Figure 2-7: Finite slab stress correction factors……...…..14
Figure 2-10: Longitudinal stress at the bottom of the slab from ISLAB2000 for Problem 1……17
Figure 2-11: Longitudinal stress at the bottom of the slab from EverFE for Problem 1….....18
Figure 2-12: Longitudinal stress at the bottom of the slab from ISLAB2000 for Problem 2.....18
Figure 2-13: Longitudinal stress at the bottom of the slab from EverFE for Problem 2…….....19
Figure 2-14: Longitudinal stress at the bottom of the slab from ISLAB2000 for Problem 3…....19
Figure 2-15: Longitudinal stress at the bottom of the slab from EverFE for Problem 3…….....20
Figure 3-1: An overview of the development of experimental matrix for parametric study…….21
Figure 3-2: Combining base and subbase layers……...…….24
Figure 3-3: Variation in results for combined base/subbase and no subbase approaches…….....24
Figure 3-4: Combining CTE and thermal gradient……...…….25
Figure 3-5: Load configurations considered in the study……..26
Figure 3-6: Sensitivity trend due to the variation in base/subbase thickness……....27
Figure 3-7: Sensitivity trend due to the variation in modulus of subgrade reaction……..……28
Figure 3-8: Sensitivity trend due to the variation in thermal strain gradients……....28
Figure 4-1: Overview of structural model…….…30
Figure 4-2: Required components for the analytical tool…….....31
Figure 4-3: Procedure of determining critical load location……..32
Figure 4-4: Validation and determination of critical load location……....33
Figure 4-5: Example critical load location (bottom stresses, MI-9, 177-in. joint spacing) ……..34
Figure 4-6: Example critical load location (bottom stresses, MI-20, 177-in. joint spacing) ……35

LIST OF FIGURES
(CONTINUED)

Figure 4-7: Example sensitivity plots of longitudinal stresses at the bottom of the PCC slab…..38
Figure 4-8: Example sensitivity plots of longitudinal stresses at the top of the PCC slab……....39
Figure 4-9: Impact of lateral support condition……...…..40
Figure 4-10: Slab curling due to different types of thermal gradients……..…….41
Figure 4-11: Effect of longitudinal joint AGG factor on stress magnitude……...43
Figure 4-12: Example illustrations of equivalent stress sections……..….46
Figure 5-1: Interpolation process……...……51
Figure 5-2: Validation procedure……..……...……..52
Figure 5-3: Overview of validation process……..…….52
Figure 5-4: Validation results – stage 1…….……53
Figure 5-5: Validation results – stage 2…….……55
Figure 5-6: Validation results – stage 3 (single axle through multi-axle (8))……....57
Figure 6-1: Schematic illustration of damage calculation process……....62
Figure 6-2: Comparison of allowable repetitions based on different fatigue transfer functions...63
Figure 6-3: Comparison of fatigue damage based on different fatigue transfer functions……....63
Figure 6-4: Load spectrum from SPS2 sections for single axle in July, 1998……...……64
Figure 6-5: Load spectrum from SPS2 sections for tandem axle in July, 1998……64
Figure 6-6: Hourly thermal gradients generated by EICM for 8-in. sections in September……..68
Figure 6-7: Cumulative damage calculation process…….…69
Figure 6-8: Calibration process for the relationship between cumulative damage and distress…70
Figure 6-9: Example characteristic fatigue curve before calibration process……...….70
Figure 6-10: Example characteristic fatigue curve after calibration process…….71
Figure 6-11: Comparison of results for Example 1…….……..75
Figure 6-12: Comparison of results for Example 2…….…..77
Figure 6-13: Comparison of results for Example 3……...……79
Figure 6-14: Overview of analysis of joint faulting for Example 4……..….79
Figure 6-15: Slab deflection results for Example 4…….…..80

LIST OF FIGURES
(CONTINUED)

Figure 6-16: Predicted faulting for Example 4……..81
Figure 6-17: Differential elastic deformation energy for Example 5……...…….82
Figure 6-18: Predicted faultings for Example 5…….82
Figure 6-19: Predicted faultings and differential elastic deformation energy……...83
Figure 6-20: Differential elastic deformation energy for Example 6……..…..84
Figure 6-21: Ratio DE/k for Example 6…….84
Figure 6-18: Predicted faultings for Example 6……...……..85
Figure 6-19: Predicted faultings and ratio DE/k at the end of 20 years…….……85

Executive Summary

The responses of rigid pavements are influenced by three major factors: (i) structural, (ii) loading, and (iii) environmental. However, the interaction between these factors cannot be directly addressed by the current AASHTO 1993 design method. This report summarizes the preliminary findings of a two-year project to study rigid pavement response due to the variations in the above mentioned factors. The report also highlights the sensitivity of pavement response to the interactions between these factors. As a part of the project, relevant issues that relate the implementation of pavement responses to engineering practice using the ISLAB2000 structural model are also discussed.

The primary objectives of this study were to i) evaluate the robustness and user friendliness of the ISLAB2000 software, ii) perform a preliminary parametric study on current and anticipated Michigan Department of Transportation (MDOT) rigid pavement cross-sections, using design inputs consistent with Michigan loading, climatic conditions, materials, subgrade support and construction parameters, and iii) prepare and conduct a technology transfer workshop for MDOT pavement designers to familiarize them with the ISLAB2000 program.

The analysis was based on a sample of 14 "approved" designs for projects that were either recently constructed or were programmed for construction in the near future. These designs provided input parameters like pavement cross-sections, material properties, traffic and environmental conditions. The final experimental matrix for the preliminary parametric study contained 43,092 combinations of inputs. Some findings based on a sample of 14 designs are summarized below:

- The ISLAB2000 program is robust and user friendly. The results from the ISLAB2000 structural model compare well with the Westergaard solutions (after considering the relevant assumptions) and other widely accepted FE structural models.

- The critical load location is influenced by joint spacing and truck or axle configuration. The fractional factorial analysis indicated that the critical load location is generally not influenced by slab thickness, base/subbase thickness, modulus of subgrade reaction, lateral support condition, and thermal gradient or thermal strain gradient.

- For a flat slab condition, when the slab thickness changes from 9 to 12 in. the resulting stress is reduced by approximately 35%. For a constant thermal gradient, pavements constructed with different slab thickness have different temperature differentials, and therefore, the pavement responses could not be compared.

- For a flat slab condition, pavement cross-sections with thicker base/subbase thickness (from 4 to 26 in.) resulted in about 5-30% lower stresses and as the slab thickness increases the impact of base/subbase thickness becomes less significant.

- Pavements constructed with 27 feet joint spacing resulted in about 33% higher longitudinal stresses as compared to pavements constructed with 15 feet joint spacing for curled slab

conditions at a thermal strain gradient value of $+10x10^{-6}$ in.$^{-1}$. The severity depends on the level of thermal curling or thermal strain gradient.

- For the load located along the wheel path (approximately 20" from the traffic stripe), pavements constructed with PCC shoulders resulted in the lowest stresses among the three lateral support conditions (12' lane with tied PCC shoulders, 12' lane with AC shoulders and 14' lane with AC shoulders) that are considered in the study. Although the pavements were constructed with the same AC shoulder, the magnitudes of longitudinal stresses for pavements with 12-ft lane (standard lane) were higher than that for pavements with 14-ft lane (widened lane). As the wheel path shifted 2 ft towards the centerline for pavements with widened lane, a pseudo-interior loading condition was created, resulting in the reduction of stresses from edge loading. Pavements constructed with AC shoulders (12-ft lane with AC shoulder) resulted in about 13% and 9% higher longitudinal stress values than pavements constructed with PCC shoulder (12-ft lane with tied PCC shoulder) and widened lane (14-ft lane with untied AC shoulder), respectively.

- Lateral wander (or lateral placement) of traffic load resulted in higher edge stresses as the load moves from the wheel path towards lane/shoulder longitudinal joint (about 10% for tied PCC shoulder and 30% for AC shoulder).

- The experimental matrix only included three levels of non-discrete inputs (base/subbase thickness, modulus of subgrade reaction and thermal strain gradients), therefore the application of interpolation was employed to capture combinations of non-discrete inputs not included in the experimental matrix. In the validation process considering all axle types, the bias (average error), variance, and mean square of errors (MSE) of the best scheme (scheme 16) were 0.51 psi, 8.63 psi^2, and 8.89 psi^2, respectively, indicating that the interpolation scheme was highly accurate and precise in computing pavement response as compared with the results directly obtained from the ISLAB2000 program.

The pavement response plays a significant role in the mechanistic-empirical (M-E) design process; however, it is necessary to integrate the pavement response with several other components. For the M-E process to be implemental and reflect Michigan practice, the following issues need to be investigated:

1) The coefficient of thermal expansion (CTE) values for concrete mixes and also aggregate (as concrete making material) used in paving Michigan roads need to be determined and cataloged, since CTE plays a critical role in the thermal analysis of jointed concrete pavements. The slab movement and joint opening are also influenced by the CTE of concrete.

2) An extensive traffic database, e.g. WIM database, should be made available for the pavement network as hourly axle spectra is a key input for damage computations. The hourly axle spectra allow for calculation of pavement responses that account for daily and seasonal conditions of climate, roadbed and material. The axle repetitions from the axle spectra and the corresponding pavement responses are the inputs to the cumulative damage calculation.

3) Develop and calibrate transfer functions for key jointed concrete pavement distresses that reflect Michigan practice. The process involves statistical correlation of the cumulative damages to the measured distresses corresponding to the time periods to obtain a calibrated model that can be used for Michigan jointed concrete pavement design.

Chapter I

INTRODUCTION

1.1 Background

The design of rigid pavements in the State of Michigan has changed over time. For the most part, the design process is based on the AASHTO 1993 method, with modifications to reflect the Michigan Department of Transportation (MDOT)'s experience and observations of pavement performance. In general, the rigid pavement cross-sections are comprised of a concrete slab 230 to 280 mm (9 to 11 in.) thick, a 100 mm (4 in.) aggregate base (OGDC or otherwise), a separator layer (either a 100 mm (4 in.) dense graded or a geotextile interlayer) all on a 250 to 300 mm (10 to 12 in.) sand subbase. The final cross-section selection is based on various considerations including the following:

- Traffic volumes, commercial trucks and load;
- Roadbed soil, including frost susceptibility;
- Drainage;
- Initial and life cycle costs;
- Joint spacing;
- Load transfer and reinforcement; and
- Life cycle cost analysis.

Current practice is to select the final cross-section based on the guidelines presented in the 1986/1993 AASHTO Guide for the Design of Pavement Structures. However, this design practice is most highly correlated to pavement ride quality, but does not necessarily assure structural integrity, nor does it directly account for the effects of pavement type (JPCP versus JRCP), joint spacing, lane width, variation in material properties along a project, environmental impact and joint design (aggregate interlock versus dowel bars) on pavement design. Further, it does not effectively address the impact of the heavy, multi-axle "Michigan Truck" on the performance of rigid pavements.

Realizing that the only way to address the multiple factors influencing rigid pavement response is through a more mechanistic approach, MDOT and Minnesota Department of Transportation (MnDOT) jointly funded a study to enhance the ILLISLAB 2-D FEM rigid pavement analysis program (Tabatabaie and Barenberg, 1980). ILLISLAB is widely recognized as the most versatile state-of-the-practice rigid pavement analysis software available. Unfortunately, its application was highly limited because of the poor user interface and limitations on the complexity of the problems that it could evaluate. The enhancement entailed the complete rewriting of the code to remove inefficiencies, significantly improving the computational ability of the software. It also included the employment of a graphical user interface (GUI) both for inputting data and examining the output. The use of ISLAB2000 allows the user to assess pavement response due to temperature, cross-section, loading and construction variables.

1.2 Research Objectives

The objective of the project was to study the impact of various parameters and their interrelationship on mechanistic responses of jointed concrete pavement (JCP) using the ISLAB2000 structural model. The primary objective was achieved in the project by i) evaluating the ISLAB2000 software and provide feedback to the developers, ii) performing a preliminary parametric study on current and anticipated MDOT rigid pavement cross-sections, using design inputs consistent with Michigan loading, climatic conditions, materials, subgrade support and construction parameters, and iii) preparing and conducting a technology transfer workshop for MDOT pavement designers to familiarize them with the ISLAB2000 program.

1.3 Scope of Research

The research plan was divided into five tasks to achieve the research objectives and to provide a better understanding of each phase of this project and the connection among them.

Task 1: Determine the robustness and friendliness of ISLAB2000

Various scenarios will be systematically evaluated to establish the robustness of the software and the comparability of the analysis results to the Westergaard's closed form solutions. The results will be compared to known design examples illustrated in the textbook "Pavement Analysis and Design" (Huang, 1993). The user friendliness of the graphical user interface (GUI) will also be assessed.

Task 2: Conduct the parametric study and sensitivity analysis

A parametric study will be designed and conducted using statistically sound practices to evaluate the impact of the following variables on pavement performance:

- Pavement thickness;
- Slab geometry;
- Load transfer;
- Support conditions;
- Axle loading, configurations, and locations;
- Temperature gradient;
- Variable material characteristics; and
- Variable support conditions.

The ISLAB2000 program will be used to calculate response (stress, strain and deflection) of a sample of pavement cross-sections. This information will be evaluated to determine design features that impact pavement response.

Task 3: Create an MDOT specific on-line help feature

To increase the usefulness of the ISLAB2000 program, an MDOT specific on-line help feature will be created. Using this feature, the user will be able to find guidance in generating the various inputs on-line. Typical values for Michigan conditions will be presented, as well as background information to assist the user in making decisions. The full user manual will also be developed and included on the CD-ROM for an easy access, including a search feature to assist the user in finding desired information.

Task 4: Conduct technology transfer workshop

A full-day technology workshop will be developed and presented to MDOT pavement designers and researchers who are the anticipated users of the ISLAB2000 program. The workshop will include:

- An introduction to the theory behind the ISLAB2000 program and mechanistic design;
- A description of the various required inputs and how reasonable values for these inputs can be obtained;
- A demonstration of how to prepare a complete input file;
- A discussion of the results, including example of transfer functions that will enhance the meaningfulness of the output; and
- Hand-on exercises that will allow each participant to develop the input and analyze the output of the problems that are of concern to them.

Each workshop participant will be provided an ISLAB2000 user's guide and a participant's workbook for future reference, as well as a CD-ROM containing the ISLAB2000 program, example problems, and electronic copies of the ISLAB2000 user's guide, participant's workbook, and copies of the presentations used during the workshop.

Task 5: Complete the final report

At the conclusion of the study the PI will submit a draft copy (multiple copies will be submitted if the PM so requests) of the final report documenting the results of the study. It is expected that the PM will review the draft final report and provide feedback within one month after receiving the report. The PI will incorporate the changes and submit the final revised report within one month of receiving the comments. The final submission will consist of 50 double-sided bound copies and one copy single-sided unbound copy`. Furthermore, a CD containing the entire report will also be submitted.

1.4 Organization of Report

This report contains background information on the parametric study of mechanistic responses of JCP using ISLAB2000, a discussion of the analyses performed and the results obtained from the parametric study, and a summary of the conclusions and recommendations derived from this study. A more detailed breakdown of the contents of individual chapters is as follows. Chapter II includes: background on the robustness and accuracy of ISLAB2000 are determined, a summary of Westergaard Theory and a summary of finite element (FE) method used in ISLAB2000. Chapter III provides an overview of the data collection process and how the final experimental matrix for the parametric study is obtained. A detailed analysis process of the parametric study is given in Chapter IV. This chapter also includes documentation and interpretation of the analysis results. The application of 'Interpolation Scheme' in quantifying the magnitude of mechanistic response at the combinations of parameters that are not addressed in the experimental matrix and its validation including the goodness of fit are elaborated in Chapter V. In addition, example use of interpolation scheme and a catalog of mechanistic responses based on the use of this interpolation scheme are also included in this chapter. Chapter VI presents a demonstration of a future step to potentially implement the product of this project into a mechanistic-empirical design process with existing transfer functions. A summary of findings and recommendations for future research arising from the analyses performed in this study as well as a listing of future research needs related to mechanistic analysis and mechanistic-empirical design of JCP are contained in Chapter VII.

Thirteen appendices are also included in this report, which are listed as follows:

Appendix A: Review of the Kirchhoff plate theory
Appendix B: Comparison between ISLAB2000 results and Westergaard's solution
Appendix C: ISLAB2000 graphical results for the comparison with Westergaard's solution
Appendix D: Data collection
Appendix E: Validation of thermal strain gradient (the product $\alpha(\Delta T/D)$)
Appendix F: Documentation of pavement response
Appendix G: Impact of lateral placement on different lateral support conditions
Appendix H: Equivalent stress cross-sections
Appendix I: Catalog of pavement response
Appendix J: Hourly load spectra from WIM database
Appendix K: Hourly thermal gradient from EICM
Appendix L: Michigan ISLAB2000 (submitted in a CD)
Appendix M: Technology transfer package

Chapter II

ROBUSTNESS AND USER FRIENDLINESS OF ISLAB2000

The robustness and user friendliness of ISLAB2000 program are investigated in this chapter based on two approaches: i) comparison of published results with ISLAB2000 results and ii) comparison of results based on ISLAB2000 program with another FE program for JCP, called EverFE (Davids and Mahoney, 1999). Several types of problems from the textbook "Pavement Analysis and Design" (Huang, 1993) are used for the first approach, while selected MDOT designs are used for the second approach.

2.1 Review of Westergaard Theory

Mechanistic analysis of rigid pavement was first introduced in the 1920's by Westergaard. Since then, mechanistic analysis has been a crucial part of the analysis and design of rigid pavement. The closed-form equations by Westergaard, however, rely on several assumptions (Westergaard, 1926) and they include:

- Infinite slab dimension,
- Full contact interface between slab and subgrade,
- Single layer (no base or subbase layers),
- Single slab (free edge boundary),
- Semi-infinite foundation,
- Single tire print,
- Circular or semi-circular loading area only,
- Dense liquid foundation (Winkler foundation).

The review of the Westergaard theory in this chapter includes information about the Winkler foundation, load cases considered in the Westergaard analysis and the Bradbury thermal curling stress formulation.

Winkler foundation

The Winkler foundation, also referred to as the Dense Liquid foundation (DL), has been traditionally used as a subgrade idealization in rigid pavement design and analysis. This idealization is based on assumptions that the subgrade cannot transfer shear stress and the slab is subjected to vertical reaction pressure equal to deflection times a constant k (modulus of subgrade reaction). In other words, the subgrade will deflect only under the area of applied load. According to McCullough (McCullough and Boedecker, 1968), the Winkler foundation model used in Westergaard's theory is a dense liquid with a density equal to k times the deflection under the load, or a bed of spring with spring constant k as illustrated in Figure 2-1.

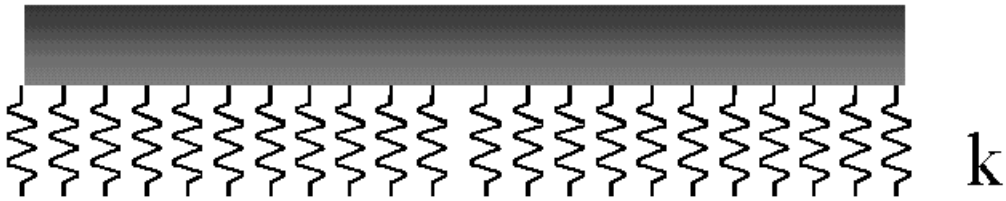

Figure 2-1: Idealization of dense liquid foundation

Load Cases

In addition to the several assumptions and the dense liquid foundation, the Westergaard's closed from solutions are also limited to only three loading conditions: interior, edge, and corner (stress at the top of the slab).

Interior loading condition (Load Case I)

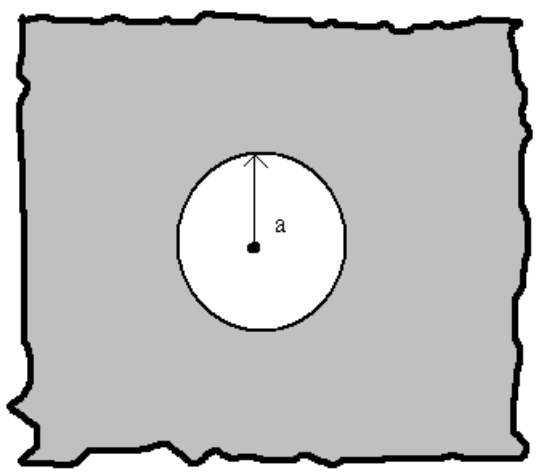

Figure 2-2: Interior loading condition

Interior loading condition is the case of a wheel load at a considerable distance from the edges. The loading stress equation was the earliest formula developed by Westergaard in 1926, (Westergaard, 1926) as illustrated in Figure 2-2. The stress at the bottom of the Portland Cement Concrete (PCC) slab due to a circular loaded area of radius "a" is computed as:

$$\sigma_i = \frac{3 \cdot (1+\mu) \cdot P}{2 \cdot \pi \cdot D^2} \cdot \left(\ln \frac{l}{b} + 0.6159 \right) \qquad (2\text{-}1)$$

Where b = a when $a \geq 1.724 \cdot D$

= $\sqrt{1.6 \cdot a^2 + D^2} - 0.675 \cdot D$ when $a < 1.724 \cdot D$

ℓ = radius of relative stiffness

$$l = \sqrt[4]{\frac{E_c \cdot D^3}{12 \cdot \left(1-\mu^2\right) \cdot k}} \qquad (2\text{-}2)$$

D = concrete slab thickness, in.
E_c= modulus of elasticity of concrete slab, psi
k = elastic modulus of subgrade support, psi/in.
μ = Poisson's ratio for concrete (0.15-0.20 as typical values)

For the same loading condition as shown in Figure 2-2, deflection of the PCC slab underneath the loading area can be calculated using the following equation.

$$\delta_i = \frac{P}{8 \cdot k \cdot l^2} \cdot \left\{ 1 + \frac{1}{2 \cdot \pi} \cdot \left[\ln\left(\frac{a}{2 \cdot l}\right) - 0.673 \right] \cdot \left(\frac{a}{l}\right)^2 \right\} \qquad (2\text{-}3)$$

Edge loading condition (Load Case II)

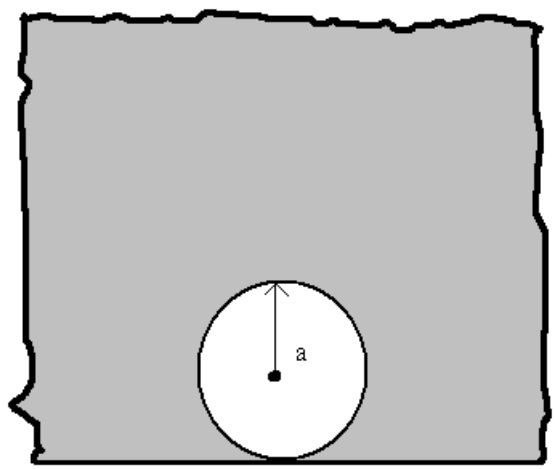

Figure 2-3: Edge loading condition

As illustrated in Figure 2-3, edge loading condition is the case in which the wheel load is at the edge, but at a considerable distance from any corner. Westergaard presented the edge loading stress equation in 1926 (Westergaard, 1926). This loading condition is important in that it results in the most critical stress at bottom of PCC slab of all three loading condition according to Westergaard. The stress and deflection formulation is as follows:

$$\sigma_e = \frac{3 \cdot (1+\mu) \cdot P}{\pi \cdot (3+\mu) \cdot D^2} \cdot \left[\ln\left(\frac{E_c \cdot D^3}{100 \cdot k \cdot a^4}\right) + 1.84 - \frac{4 \cdot \mu}{3} + \frac{1-\mu}{2} + \frac{1.18 \cdot (1+2 \cdot \mu) \cdot a}{l} \right] \qquad (2\text{-}4)$$

$$\delta_e = \frac{\sqrt{2+1.2 \cdot \mu} \cdot P}{\sqrt{E_c \cdot D^3} \cdot k} \cdot \left[1 - \frac{(0.76+0.4 \cdot \mu) \cdot a}{l} \right] \qquad (2\text{-}5)$$

Corner loading condition (Load Case III)

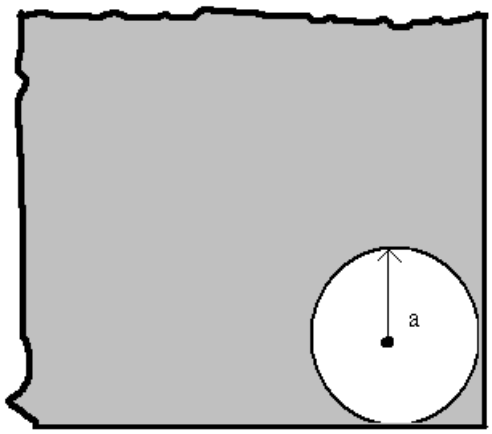

Figure 2-4: Corner loading condition

Corner loading condition is the case in which the wheel load is at a corner of the slab. Even though an equation for determining stress due to the corner loading condition was developed by Goldbeck (1919) and Older (1924) earlier, Westergaard was the first to discover that the maximum stress due to corner loading condition is not at the slab corner, but is at a distance of $2.38\sqrt{al}$ from the corner. Westergaard also included this correction into his formulas for determining stress and deflection in 1926 as shown below, respectively.

$$\sigma_c = \frac{3 \cdot P}{D^2} \cdot \left[1 - \left(\frac{a \cdot \sqrt{2}}{l} \right)^{0.6} \right] \tag{2-6}$$

$$\delta_c = \frac{P}{k \cdot l^2} \cdot \left[1.1 - 0.88 \cdot \left(\frac{a \cdot \sqrt{2}}{l} \right) \right] \tag{2-7}$$

The corner loading condition according to Westergaard's produces the most critical deflection of all three Westergaard loading conditions. It should also be noted that the maximum stress due to this loading condition is located at the top of PCC slab (not bottom as edge and interior loading conditions).

Among the three loading conditions by Westergaard, the corner loading condition is the most obscure. It should be noted that fully contacted interface between layers is one of the assumptions used in Westergaard's formulations and this assumption is not realistic because it leads to underestimation of stresses and deflections at top of PCC layer. In other words, the incapability of simulating the lack of support in Westergaard's formulation causes the variation between Westergaard's and FE solutions for corner loading condition, at which the lack of support has a significant impact on stresses and deflections. Stress and deflection equations for the corner loading condition based on the FE method were suggested as shown below (Ioannides et al, 1985).

$$\sigma_c = \left(\frac{3 \cdot P}{h^2}\right) \cdot \left[1.0 - \left(\frac{c}{l}\right)^{0.72}\right] \tag{2-8}$$

$$\delta_c = \left(\frac{P}{k \cdot l^2}\right) \cdot \left[1.205 - 0.69 \cdot \left(\frac{c}{l}\right)\right] \tag{2-9}$$

Results based on equations recommended by Ioannides et al (1985) were also compared with ISLAB2000 results.

Dual tires simulation

Since all Westergaard's loading stress equations for a single tire print are circular loading area based. It is necessary to convert dual tires into a single circular loading area. Equation 2-10 allows for the conversion from dual tires to a single tire (Huang, 1993).

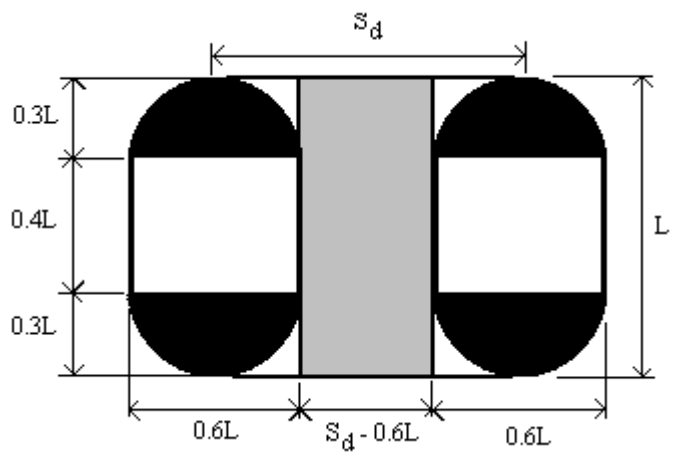

Figure 2-5: Dual tires simulation represented by a circular loading area

$$a = \sqrt{\frac{0.8521 \cdot P_d}{q \cdot \pi} + \frac{S_d}{\pi} \cdot \left(\frac{P_d}{0.5227 \cdot q}\right)^{\frac{1}{2}}} \tag{2-10}$$

Where P_d = load on one tire
q = contact pressure (one tire)
S_d = dual spacing (center to center)

Curling stress formulation

The environmental effects on rigid pavements can be accounted for in terms of temperature differential between top and bottom layers of PCC. Positive temperature gradient (top layer is warmer than bottom layer) contributes to downward curling, whereas negative temperature gradient (bottom layer is warmer than top layer) contributes to upward curling. This is illustrated in the Figure 2-6.

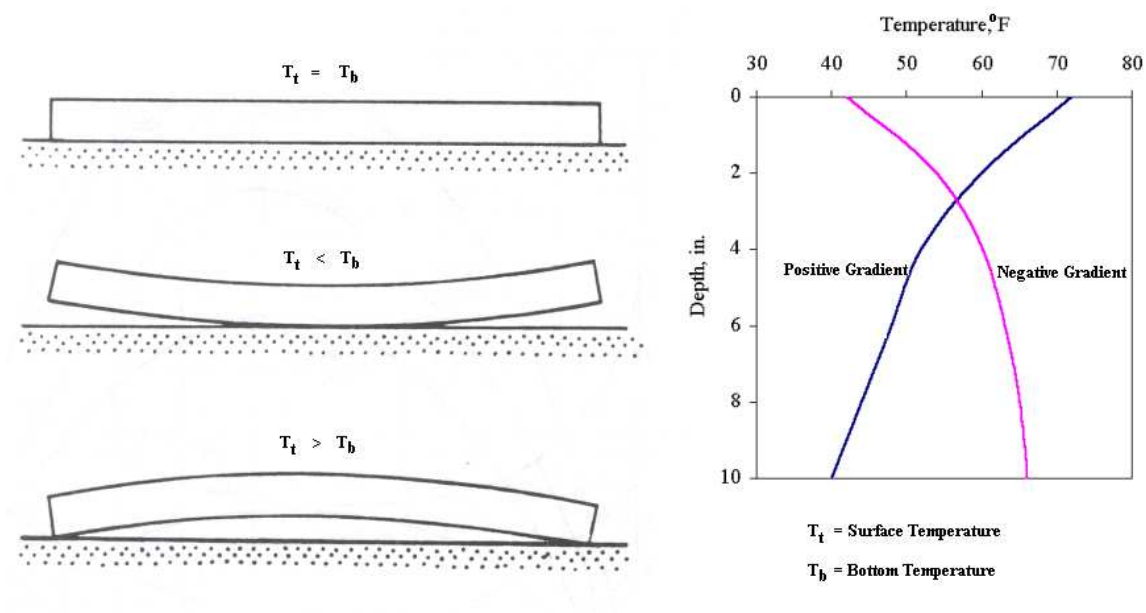

Figure 2-6: Effect of temperature gradient on slab curling

For upward curling, the top layer of PCC contracts while the bottom layer expands with respect to the neutral axis; however, the concrete slab weight will try to move the corners of slab down. Negative moment due to slab weight will cause tension at top of PCC layer and compression at bottom of PCC layer. In contrast, for downward curling, top of PCC layer expands while bottom of PCC layer contracts with respect to the neutral axis; corners of slab will move down but slab center will lift up. Consequently, slab weight will try to move its center down and this causes tension at bottom and compression at top of PCC layer. The following are the curling stress equations by Bradbury.

$$\sigma_{ix} = \frac{E_c \cdot \alpha_t \cdot \Delta t}{2 \cdot \left(1 - \mu^2\right)} \cdot \left(C_x + \mu \cdot C_y\right) \tag{2-11}$$

$$\sigma_{iy} = \frac{E_c \cdot \alpha_t \cdot \Delta t}{2 \cdot \left(1 - \mu^2\right)} \cdot \left(C_y + \mu \cdot C_x\right) \tag{2-12}$$

$$\sigma_e = \frac{C \cdot E_c \cdot \alpha_t \cdot \Delta t}{2} \tag{2-13}$$

Where σ_{ix} = interior curling stress in x-direction
σ_{iy} = interior curling stress in y-direction
σ_e = edge curling stress (can be used for x and y-direction)
α_t = coefficient of thermal expansion
Δt = temperature differential
C_x, C_y = finite slab correction factor in x and y-direction

From slab dimension and radius of relative stiffness, finite slab correction factors for both x and y-direction can be approximated using the following chart.

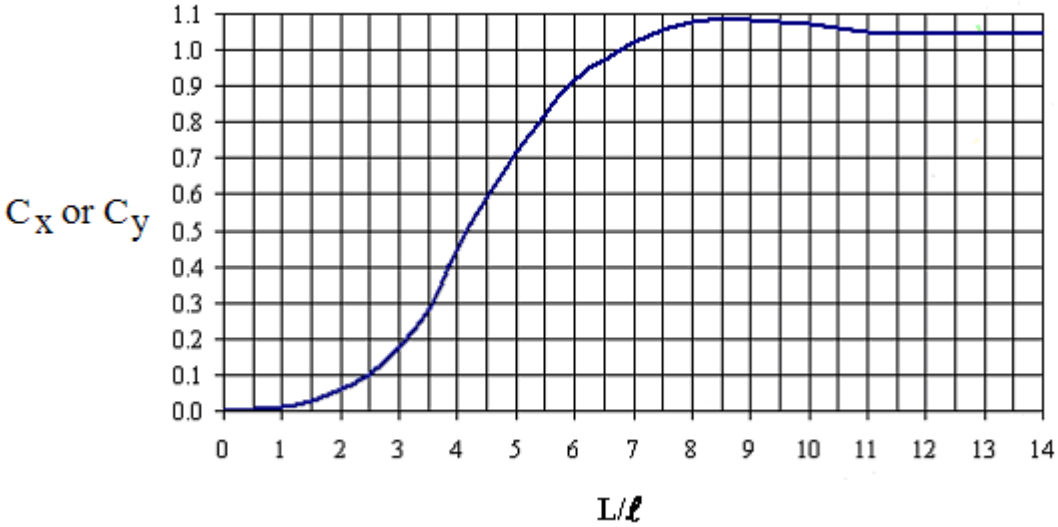

Figure 2-7: Finite slab stress correction factors (Huang, 1993)

2.2 Review of FE Method

Kirchhoff plate theory, which is the theory behind ISLAB2000 FE model, is reviewed, including the Winkler foundation in FE, element discretization, and FE global system. The details of the Kirchhoff plate theory can be found in Appendix A.

2.3 Comparison of Published Results with ISLAB2000 Results

Several examples and problems in chapter 4 (Stresses and Deflections in Rigid Pavements) of the textbook "Pavement Analysis and Design" by Yang H. Huang were solved using ISLAB2000. The software was used to simulate traffic loads, temperature gradients, pavement features such as PCC thickness, joint spacing, and subgrade soils as listed in the textbook. The results obtained from the ISLAB2000 model and Westergaard solutions were compared. It has to be noted that in order to simulate problems using ISLAB2000, two assumptions need to be made: slab size requirements to simulate infinite slab behavior and square load contact area to simulate circular load contact area as indicated in Westergaard's theory.

The following are slab size requirements for Westergaard responses based on the FE method, (Ioannides et al, 1985), in terms of L/ℓ when L is least slab dimension and ℓ is radius of relative stiffness.

Table 2-1: Required L/l ratio for FE solutions to satisfy Westergaard's assumptions (Ioannides et al, 1985)

Response	Load Placement		
	Interior	Edge	Corner
Maximum Deflection	8.0	8.0	5.0
Maximum Bending Stress	3.5	5.0	4.0

The problems can be categorized into three groups:

1. curling (temperature) stress only,
2. corner, interior, and edge stresses and deflections due to wheel load(s),
3. combined temperature and loading stresses.

Each problem was divided into two parts: the textbook solution, and the ISLAB2000 solution (FE solution). The textbook solution consists of the problem statement, an illustration of the problem, and solution based on Westergaard's equations, while the FE solution consists of the summary of inputs, illustration of the mesh and loading used in problem, followed by a short explanation if necessary, and numerical and graphical outputs in Appendices B and C, respectively. Out of the nine problems selected from the textbook, four problems were solved for four mesh sizes (3, 6, 12, and 24 in.) using ISLAB2000. The difference of the results based on 3 in. and 6 in. mesh sizes was found to be negligible. Therefore, the other five problems were solved only for three mesh sizes (6, 12, and 24 in.). It should also be noted that the mesh aspect ratio of 1 (square mesh) was used for all the problems.

2.4 Summary Comparison of Published Results with ISLAB2000 Results

In summary, the variations between the published results based on the Westergaard solutions and the ISLAB2000 results are shown in Table 2-2. The results suggest that responses obtained from the ISLAB2000 program and from the Westergaard theory are comparable with the exception of the corner loading condition. Relatively large variations were observed for corner stress and deflection results. However, the difference in the results between the two approaches has been reported, (Ioannides et al, 1985). After applying the equations suggested by Ioannides et al (1985), the ISLAB2000 results and the results based on the closed form solutions appear to be more comparable. Table 2-3 summarizes the overall percent variation between the closed form and the ISLAB2000 results.

Table 2-2: Summary of results and percent variation of the results

Problem	Response Type	Textbook Results	Unit	FE Results				Percent Variation			
				ISLAB2000 with Various Mesh Sizes				ISLAB2000 with Various Mesh Sizes			
				24"	12"	6"	3"	24"	12"	6"	3"
1	Int. Stress	238.0	psi	231.6	230.1	230.3	230.5	2.69	3.31	3.25	3.14
	Edg. Stress	214.0	psi	219.0	220.1	220.3	219.8	2.35	2.87	2.95	2.72
2	Cor. Stress	186.6	psi	198.4	197.9	195.8	195.8	6.32	6.06	4.93	4.93
	Cor. Stress*	190.2	psi	198.4	197.9	195.8	195.8	4.29	4.03	2.93	2.93
3	Int. Stress	143.7	psi	140.6	159.0	151.9	144.2	2.16	10.65	5.69	0.35
4	Edg. Stress	279.4	psi	285.9	306.5	294.9	287.2	2.33	9.70	5.54	2.79
5	Cor. Stress	166.8	psi	182.3	178.1	177.6	-	9.29	6.77	6.47	-
	Int. Stress	130.8	psi	135.5	144.2	132.8	-	3.59	10.24	1.54	-
	Edg. Stress	244.2	psi	263.8	267.6	255.2	-	8.03	9.58	4.50	-
6	Int. Stress	282.4	psi	296.6	296.3	296.2	-	5.03	4.92	4.89	-
	Edg. Stress	240.0	psi	244.2	244.9	245.4	-	1.74	2.05	2.23	-
	Pt. A	211.4	psi	197.3	195.3	194.8	-	6.69	7.62	7.87	-
	Pt. B	198.0	psi	197.8	196.3	196.0	-	0.09	0.86	1.04	-
	Pt. C	57.6	psi	50.4	49.9	49.7	-	12.55	13.42	13.65	-
7	Cor. Stress	172.8	psi	171.1	166.5	164.5	-	0.98	3.65	4.80	-
8	Int. Stress	139.7	psi	137.6	134.1	123.3	-	1.50	4.01	11.74	-
9	Edg. Stress	252.5	psi	247.7	237.9	227.4	-	1.90	5.78	9.94	-
2	Cor. Defl.	0.0502	in.	0.0562	0.0563	0.0563	0.0563	11.95	12.15	12.15	12.15
	Cor. Defl.*	0.0560	in.	0.0562	0.0563	0.0563	0.0563	0.36	0.54	0.54	0.54
3	Int. Defl.	0.0067	in.	0.0068	0.0069	0.0069	0.0069	1.94	3.28	2.99	2.84
4	Edg. Defl.	0.0207	in.	0.0211	0.0212	0.0212	0.0212	2.08	2.32	2.42	2.42

* Remarks: the comparison is based on Ioannides's approach

Table 2-3: Overall variation between Westergaard and FE solutions

Response Type and Location	Variation (%)
Interior Loading Stress	3.84
Interior Loading Deflection	2.99
Edge Loading Stress	4.09
Edge Loading Deflection	2.42
Corner Loading Stress*	2.93
Corner Loading Deflection*	0.54

* Remarks: the comparison is based on Ioannides's approach

2.5 Summary Comparison of Practical Engineering Results based on ISLAB2000 and EverFE

The capability of the ISLAB2000 program to provide comparable results with the closed form solutions has been demonstrated in the previous section; however, the load configurations and the structural conditions in the closed form solutions are not realistic. It is also important to ensure that the ISLAB2000 is also able to provide accurate results for practical engineering problems. To achieve this, the ISLAB2000 program and EverFE program are used to analyze selected MDOT designs. The comparability of the results based on these two FE programs is investigated through following engineering problems:

Problem 1: A pavement system with 11.8-in. PCC slab, 15.7-in. aggregate base, 99-psi/in. roadbed, 315-in. joint spacing, 12-ft lane, and tied PCC shoulder is given (an MDOT design on I-75 (C.S. 82191 & 82194 and J.N. 45699) submitted on June 12, 2001 as the second design alternative). Analyze this pavement system for longitudinal stress at the bottom of the slab under the impact of 18-kips single axle edge loading using the ISLAB2000 and EverFE program.

Solution: The same mesh size (12 in. by 12 in.) is used for both ISLAB2000 and EverFE program. The results obtained from the ISLAB2000 and EverFE program are 87.1 psi and 97.4 psi, respectively. Figures 2-10 and 2-11 illustrate the graphical results obtained from both programs. It can be seen that the peak stress magnitudes and locations obtained from these models are comparable.

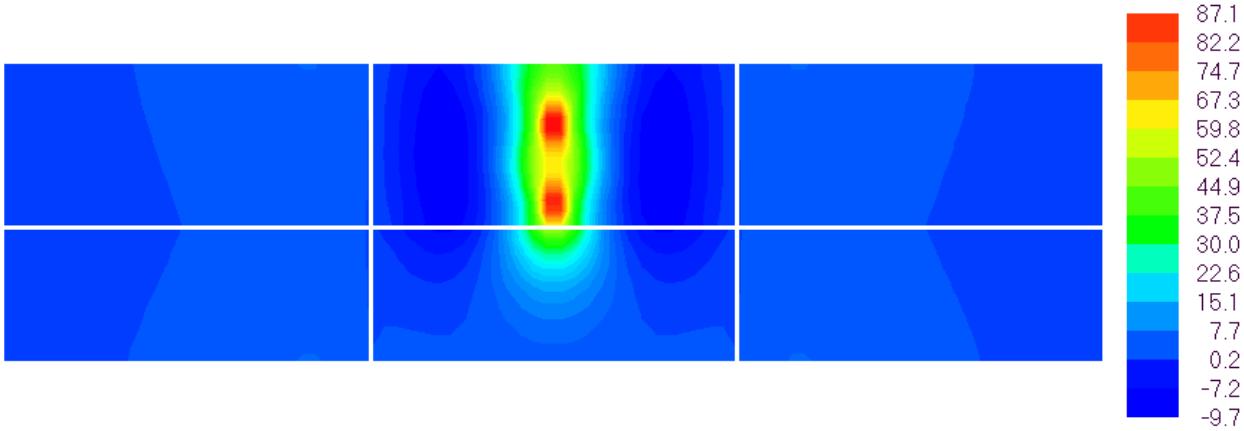

Figure 2-10: Longitudinal stress at the bottom of the slab from ISLAB2000 for Problem 1

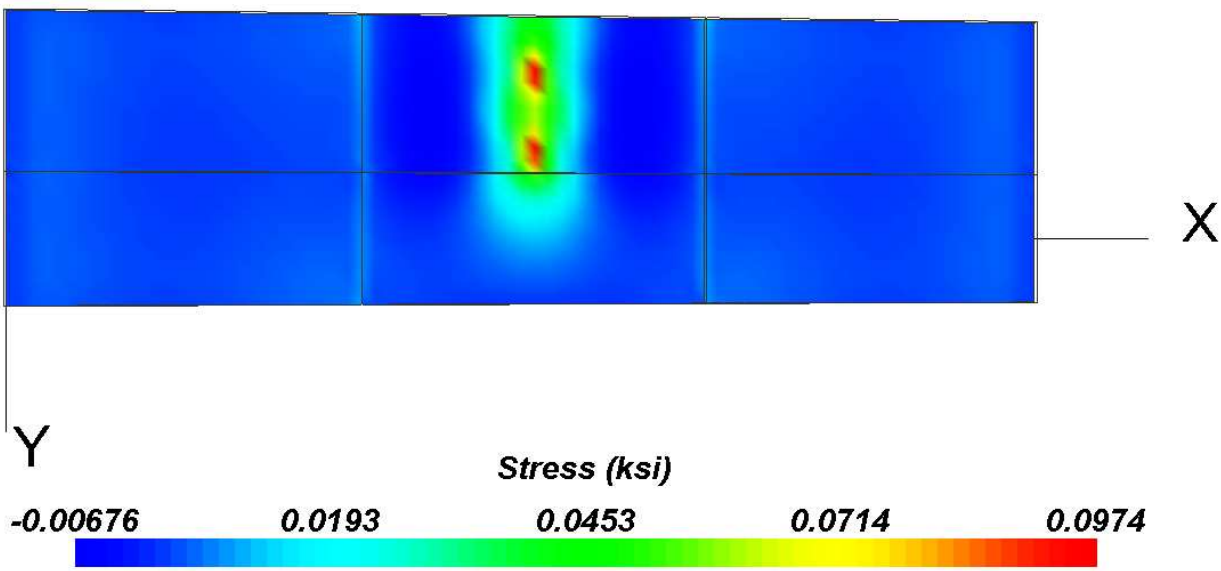

Figure 2-11: Longitudinal stress at the bottom of the slab from EverFE for Problem 1

Problem 2: A pavement system with 11.0-in. PCC slab, 3.9-in. aggregate base, 169-psi/in. roadbed, 177-in. joint spacing, 14-ft lane, and untied AC shoulder is given (an MDOT design on M-39 (C.S. 82192 and J.N. 45702) submitted on July 5, 2000 as the second design alternative). Analyze this pavement system for longitudinal stress at the bottom of the slab under the impact of 18-kips single axle edge loading using the ISLAB2000 and EverFE program.

Solution: The same mesh size (12 in. by 12 in.) is used for both ISLAB2000 and EverFE program. The results obtained from the ISLAB2000 and EverFE program are 97.1 psi and 104 psi, respectively. Figures 2-12 and 2-13 illustrate the graphical results obtained from both programs. It can be seen that the peak stress magnitudes and locations obtained from these models are comparable.

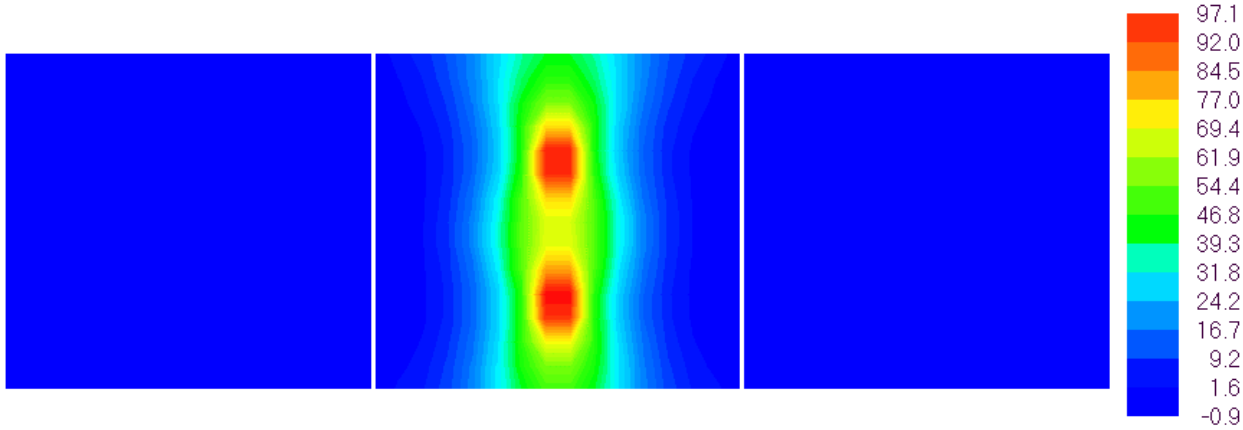

Figure 2-12: Longitudinal stress at the bottom of the slab from ISLAB2000 for Problem 2

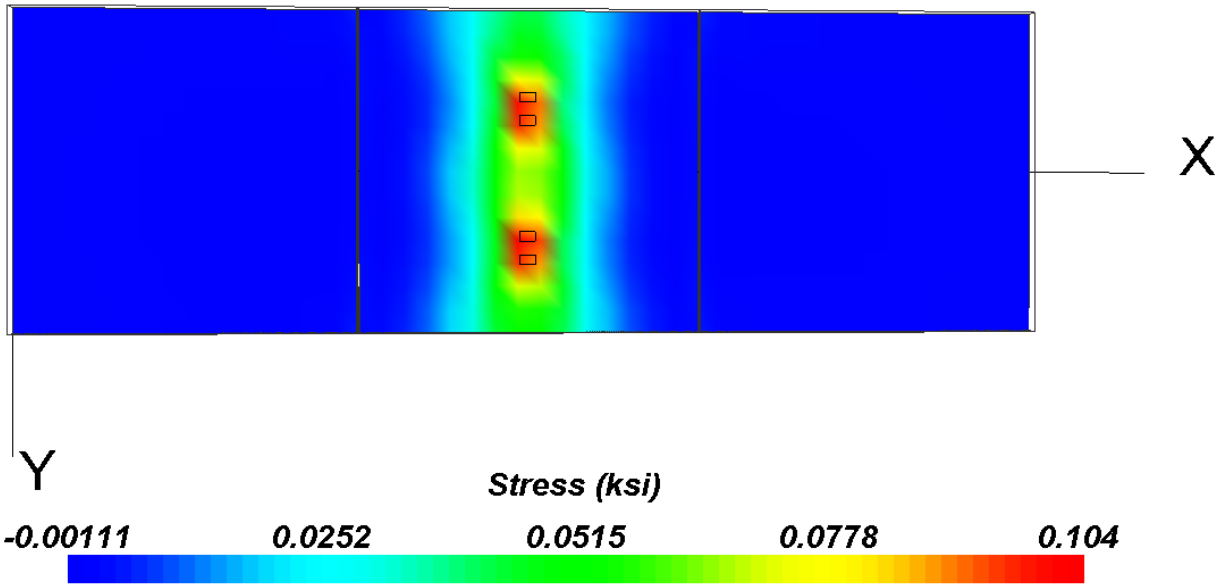

Figure 2-13: Longitudinal stress at the bottom of the slab from EverFE for Problem 2

It should be noted that unlike ISLAB2000, EverFE is not capable of modeling slabs with more than one material in the same system. Therefore, the untied AC shoulder is modeled by having no shoulder for both analyses.

<u>Problem 3</u>: Repeat Problem 1, but also consider a positive thermal gradient of 4 ^{o}F/in.

Solution: The same mesh size (12 in. by 12 in.) is used for both ISLAB2000 and EverFE program. The results obtained from the ISLAB2000 and EverFE program are 557.5 psi and 571 psi, respectively. Figures 2-14 and 2-15 illustrate the graphical results obtained from both programs. It can be seen that the peak stress magnitudes and locations obtained from these models are comparable.

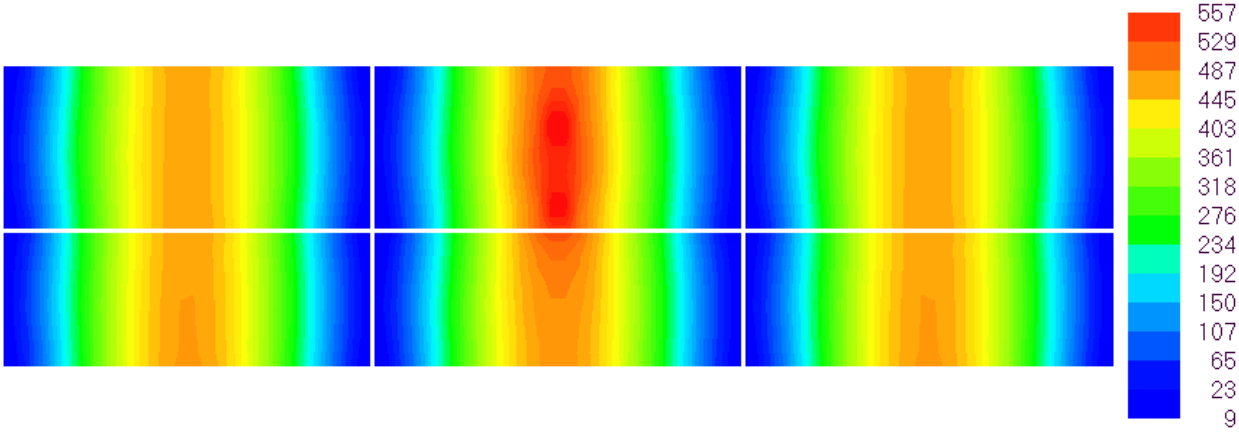

Figure 2-14: Longitudinal stress at the bottom of the slab from ISLAB2000 for Problem 3

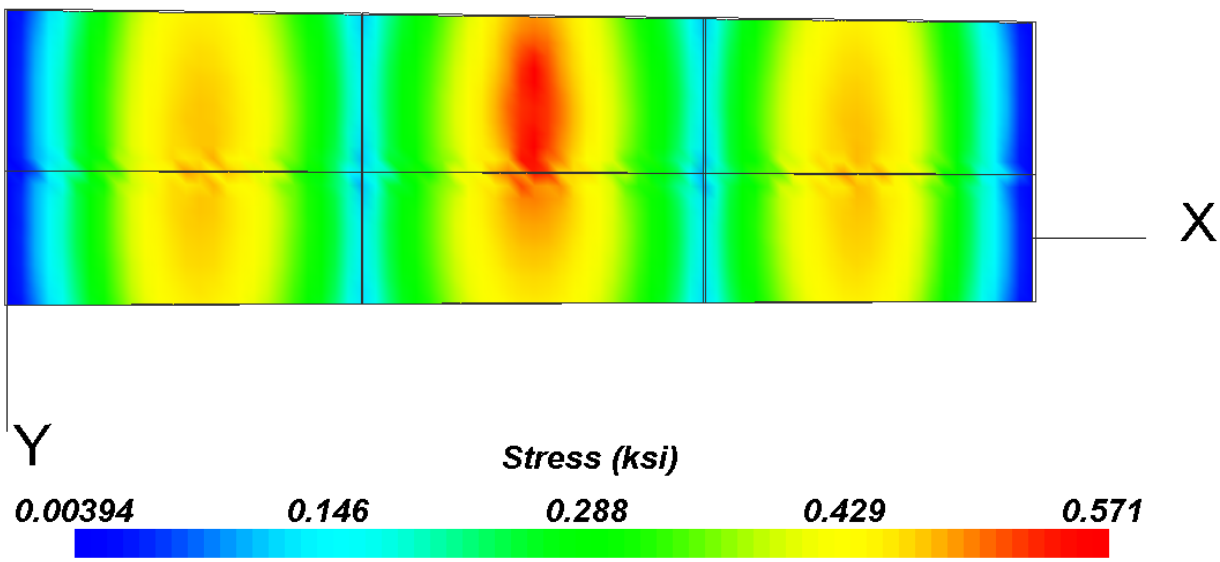

Figure 2-15: Longitudinal stress at the bottom of the slab from EverFE for Problem 3

It is important to note that due to their difference in structural models in that the ISLAB2000 program is a 2-D FE program, while the EverFE program is a 3-D FE program, the results obtained from these programs are not expected to perfectly match. However, according to these three practical engineering problems, the ISLAB2000 appears to provide similar results, when compared with results obtained from EverFE, which is another independent analysis approach. Therefore, this proves that the ISLAB2000 program is capable of providing reasonable analysis results for practical engineering problems.

Chapter III

EXPERIMENTAL MATRIX

An experimental matrix was constructed based on the concept of complete factorial for all combinations of design inputs reflecting MDOT practice, climatic condition, and load configurations in Michigan. Several engineering principles and common knowledge were applied to modify the experimental matrix with the purpose of making the experimental matrix more concise, but providing the same level of information. An overview of the process is illustrated in Figure 3-1.

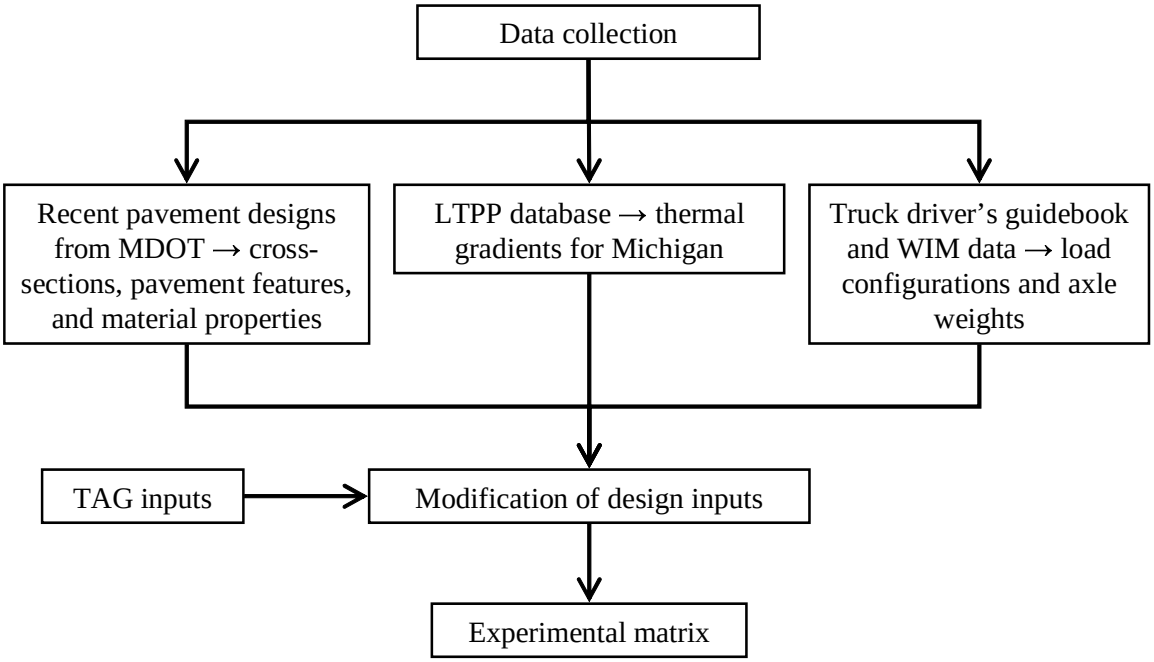

Figure 3-1: An overview of the process of development of experimental matrix for parametric study

3.1 Data Collection

The MDOT Technology Advisory Group (TAG) provided 14 "approved" designs for projects that were either recently constructed or were programmed for construction in the near future. These designs provided the structural parameters used for Michigan rigid pavements, e.g., cross-sections, pavement features, material properties, and etc. The ranges of inputs obtained from the MDOT designs are summarized in Table 3-1. Additional details are summarized in Appendix D.

Table 3-1: Summary of design parameters from the 14 MDOT designs

Inputs	Min.	Max.
PCC thickness	240 mm (9.5 in.)	300 mm (12.0 in.)
Base thickness	100 mm (4.0 in.)	400 mm (16.0 in.)
Subbase thickness	No subbase	300 mm (12.0 in.)
Joint spacing	4.5 m (177 in.)	8.0 m (315 in.)
Lane width	3.6 m (12 ft)	4.2 m (14 ft)
Lateral support condition	PCC shoulder, AC shoulder Widened lane	
Joint design	Doweled (1.25 in. diameter at 12 in. spacing center to center)	
E_{pcc}	$29x10^6$ kPa ($4.2x10^6$ psi)	
Modulus of subgrade reaction	24 kPa/mm (90 psi/in.)	60 kPa/mm (220 psi/in.)

In addition to the above mentioned input parameters, the analytical model required the following additional parameters (i) coefficient of thermal expansion (CTE) of the concrete, (ii) thermal gradients, (iii) axle and truck configurations, (iv) Poisson's ratio and unit weight. Based on the review of the literature (Klieger and Lamond, 1994), LTPP database, Truck driver's guidebook for Michigan (Michigan Center for Truck Safety, 2001), and conversations with the TAG, ranges for these additional input parameters were established and are summarized in Table 3-2.

Table 3-2: Ranges of input parameters obtained from other sources

Input variables	Ranges
Concrete unit weight	0.0087 lb/in.^{3}
Concrete Poisson's ratio	0.15 - 0.20
Aggregate base unit weight	0.0061 lb/in.^{3}
Aggregate base Poisson's ratio	0.35
Thermal gradient	-4 - +4 ^{o}F/in.
Coefficient of thermal expansion	$3x10^{-6}$ - 9 x 10^{-6} in./in./^{o}F
Location of stress	Top and bottom
Load configuration	Single axle, tandem axle,… Multi-axle (8), MI-1, MI-2,… MI-20

3.2 Preparation of Experimental Matrix

An important first step in data analysis is to ensure that the project objectives can be accomplished within the limitations of time and funds. If every combination of input parameters is to be considered, the complete factorial experimental matrix would result in millions of FE runs. Hence, the experimental matrix size must be reduced, while the final product still serves the primary objectives. The preparation of the final matrix was achieved by carrying out the following strategies: combining variables, considering only frequently seen load configurations, and adjusting increments for non-discrete inputs.

Combining Variables

Two variables are combined into one variable to reduce the number of input combinations in the experimental matrix based on an assumption that the mechanistic response computed considering the combined variable would be the same or approximately the same as that computed considering the two variables, separately. The variables to be combined are base thickness and subbase thickness, which are combined into base/subbase thickness, and CTE (α) and thermal gradient ($\Delta T/D$), which are combined into thermal strain gradient.

Figure 3-2 illustrates how base thickness and subbase thickness can be combined. It is assumed that the two layers have an unbonded interface, one elastic modulus represents the combined layer, and the Poisson's ratios of the two layers are approximately the same (Khazanovich and Yu, 2001). Sensitivity study of the accuracy of the combined base/subbase thickness was conducted for the 14 MDOT designs by comparing the mechanistic responses computed based on the two-layer system (PCC and combined base/subbase layers on the top of subgrade) and that based on the three-layer system (PCC, base and subbase layers on the top of subgrade). In this sensitivity study, for the three-layer system approach, an unbonded interface condition and Totski interface model (ERES Consultants, 1999) were considered between base and subbase layers and between PCC and base layers, respectively. An unbonded interface condition was considered for the two-layer system approach. It was found that the difference in the magnitudes of stresses between the two approaches is less than 4%. The results from the sensitivity study are illustrated in Figure 3-3 as compared with the results based on no subbase for the 14 MDOT design.

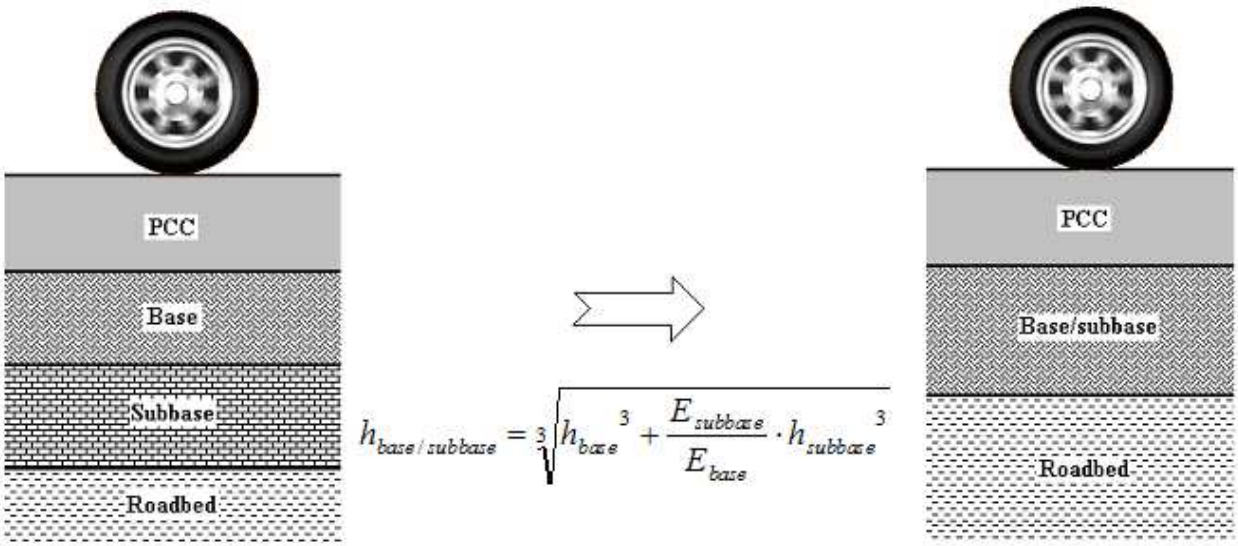

$$h_{base/subbase} = \sqrt[3]{h_{base}^{3} + \frac{E_{subbase}}{E_{base}} \cdot h_{subbase}^{3}}$$

Figure 3-2: Combining base and subbase layers

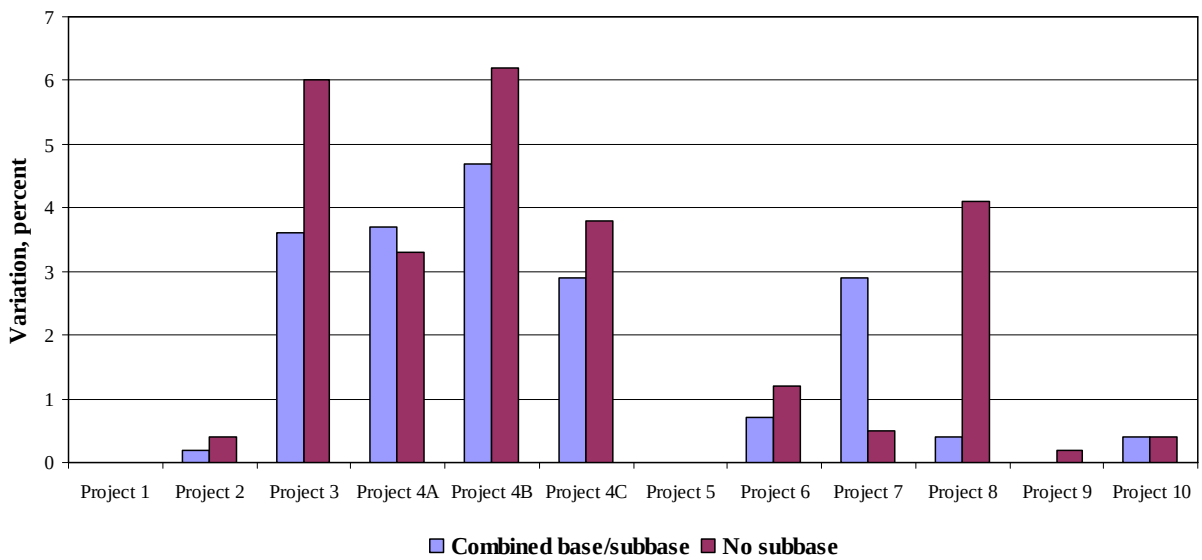

Figure 3-3: Comparison of variation in results for combined base/subbase and no subbase approaches

*Remarks: there is no subbase layer for projects 1 and 5

The CTE and thermal gradient are simultaneously accounted for in terms of the product of the two variables, $\alpha(\Delta T/D)$ or thermal strain gradient. Figure 3-4 illustrates the sensitivity plots to validate this assumption. The sensitivity study was conducted for nine cases by comparing the mechanistic responses computed based on two analysis approaches. Analysis approach 1 consists of varying CTE, while keeping thermal gradient constant. Analysis approach 2 consists of keeping CTE constant, while varying thermal gradient.

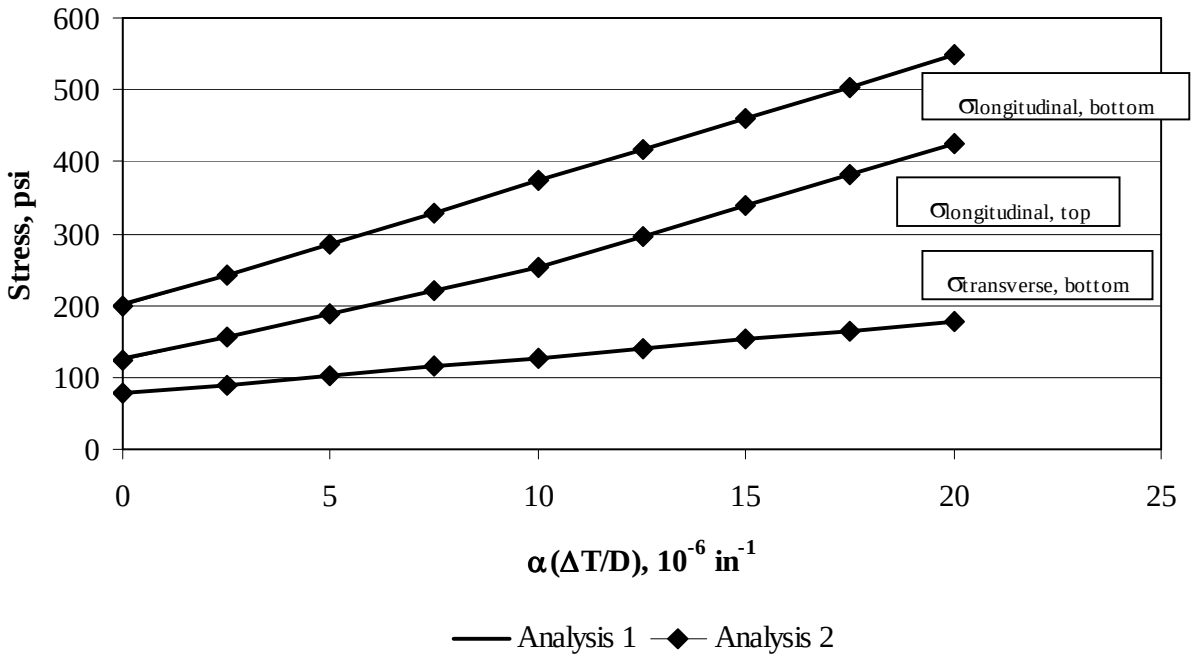

Figure 3-4: Combining CTE and thermal gradient

* Analysis 1: Constant temperature gradient (+2 ^{o}F/in.) with variation of CTE (0.1×10^{-6} to 10×10^{-6} in./in./^{o}F)
Analysis 2: Constant CTE (5×10^{-6} in./in./^{o}F) with variation of temperature gradient (0 to +4 ^{o}F/in.)

** PCC shoulder, 10-in. PCC thickness, 16-in. base/subbase thickness, 100-psi/in. k-value, single axle loading, 177-in. joint spacing

It was found that the mechanistic responses computed based on the two approaches are identical. A statistical experiment to illustrate the validity of combining CTE and thermal gradient was conducted by repeating this process for eight more combinations of pavement parameters selected based on a fractional factorial (Appendix E). It should be noted that pavements with different slab thickness with the same thermal strain gradient is not valid for comparison since the pavements are subjected to different temperature differentials. Comparison of pavement responses under a curled slab condition, therefore, should only be made within the same slab thickness.

Considering Only Frequently Seen Load Configurations

Several axle and truck configurations are contained in the Truck driver's guidebook for Michigan (Michigan Center for Truck Safety, 2001). Based on the TAG's recommendations, certain axle and truck configurations, not existent or not frequently seen, could presumably be omitted. Only 8 axle configurations and 11 truck configurations are selected for the experimental matrix. Figures 3-5 (a) and (b) illustrate the axle and truck configurations included in the parametric study.

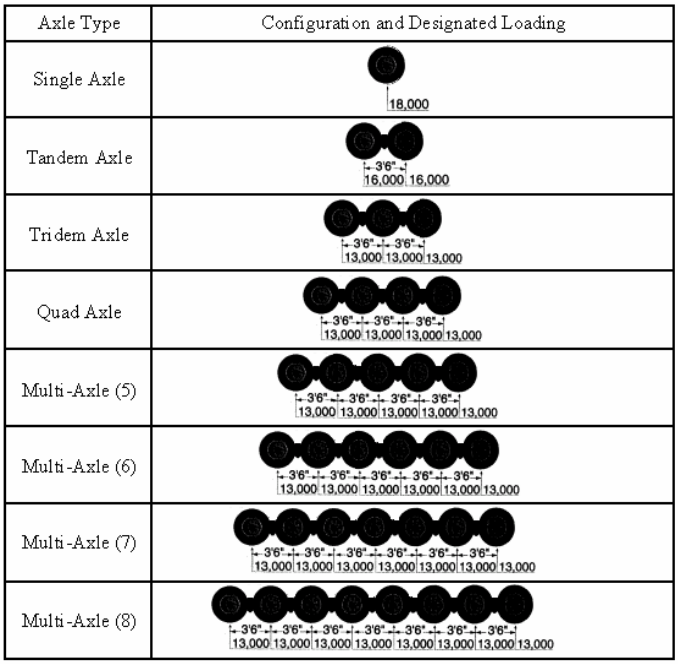

(a) Axle configurations

Figure 3-5: Load configurations considered in the study

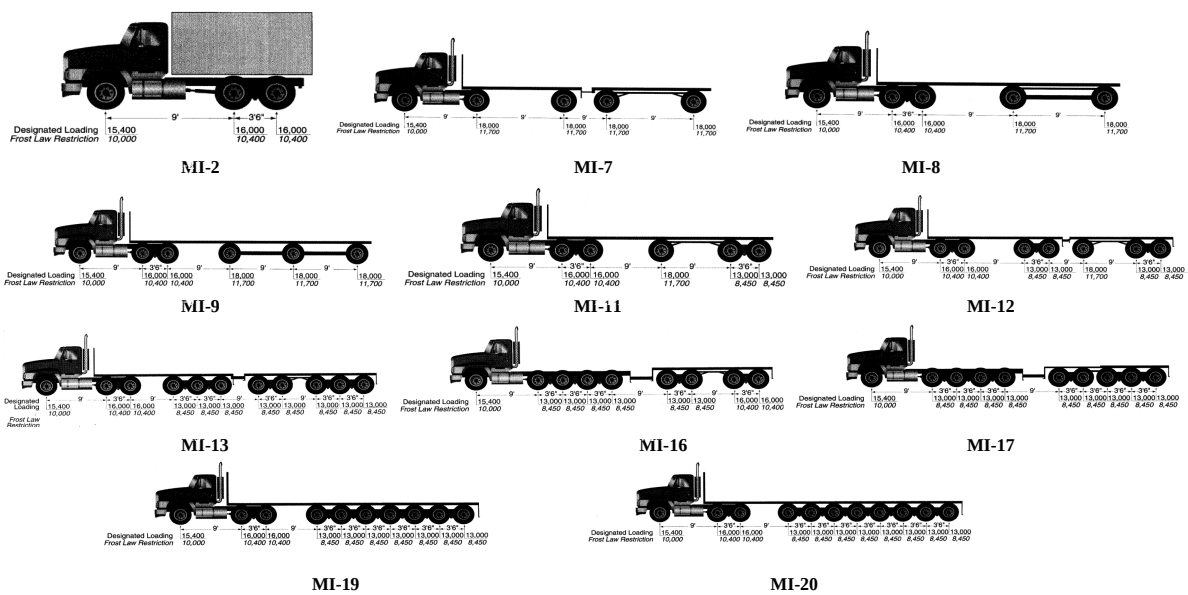

(b) Truck configurations

Figure 3-5: Load configurations considered in the study (continued)

Adjusting Increments for Non-Discrete Inputs

Input increments need to be carefully considered for non-discrete variables, in this case, these included base/subbase thickness, modulus of subgrade reaction (k-value), and thermal strain gradient. The finer increments can better capture trends of the mechanistic responses, but will

also result in increased number of FE runs. Therefore, it is crucial to capture trends of the mechanistic responses with large increments of input parameters as possible. Five values of each non-discrete variable were used in the sensitivity study of input increments. Based on this "mini analysis", it was determined that response trends could be adequately captured by using three values for each non-discrete variable. These values for the base/subbase thickness, k-value, and thermal strain gradient are 4, 16, 26 in., 30, 100, 200 psi/in., and 0, ±10, ±20x10^{-6} in.$^{-1}$, respectively. It should be noted that positive thermal gradients are considered for analysis of stresses at the bottom of the PCC slab, while negative thermal gradients are considered for analysis of stresses at the top of the PCC slab, since the critical stress locations correspond with the types of thermal gradient. Figures 3-6 through 3-8 illustrate the trends of stresses with variations of base/subbase thickness, modulus of subgrade reaction, and thermal strain gradient, respectively. Note that if not specified, the parameters for these sensitivity plots are 10-in. PCC slab, 16-in. base/subbase, 100-psi/in. modulus of subgrade reaction, PCC shoulder, 177-in. joint spacing, 18-kips single axle, and thermal strain gradient of zero.

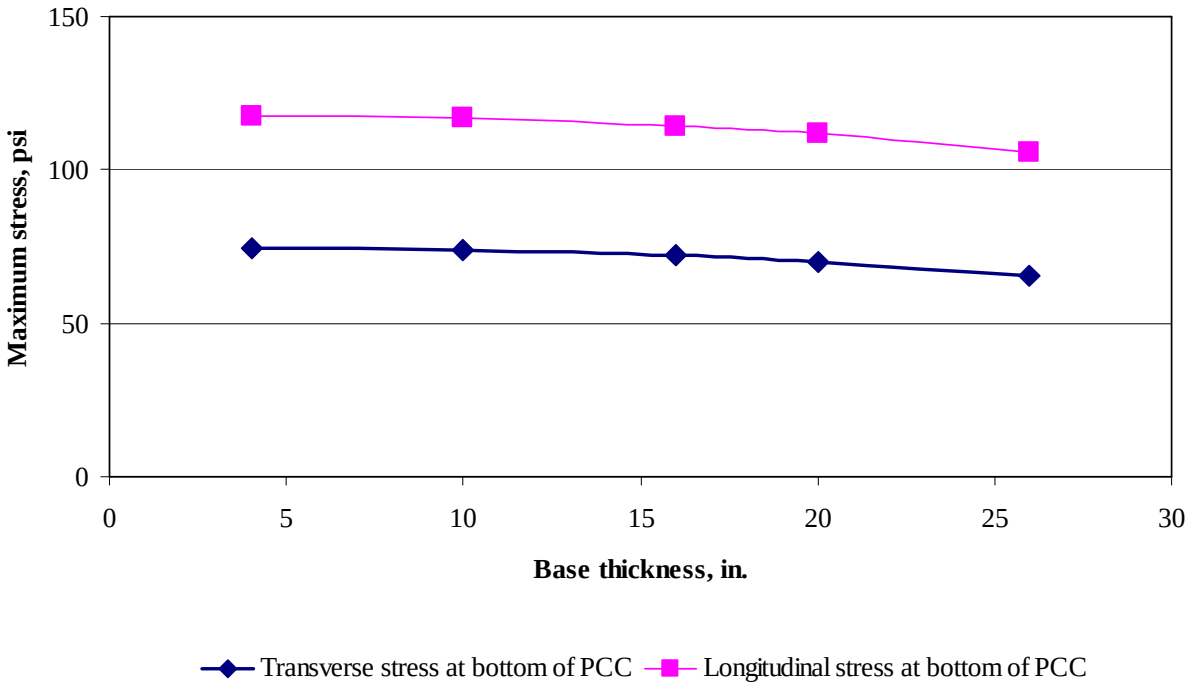

Figure 3-6: Sensitivity trend due to the variation in base/subbase thickness

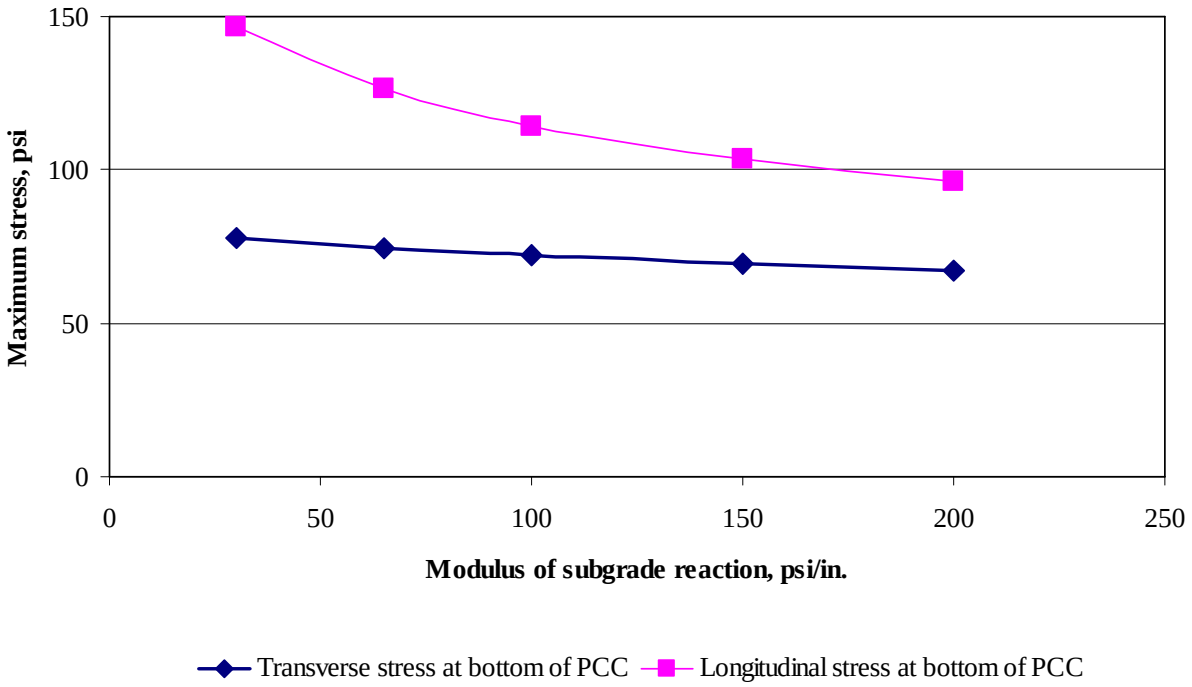

Figure 3-7: Sensitivity trend due to the variation in modulus of subgrade reaction

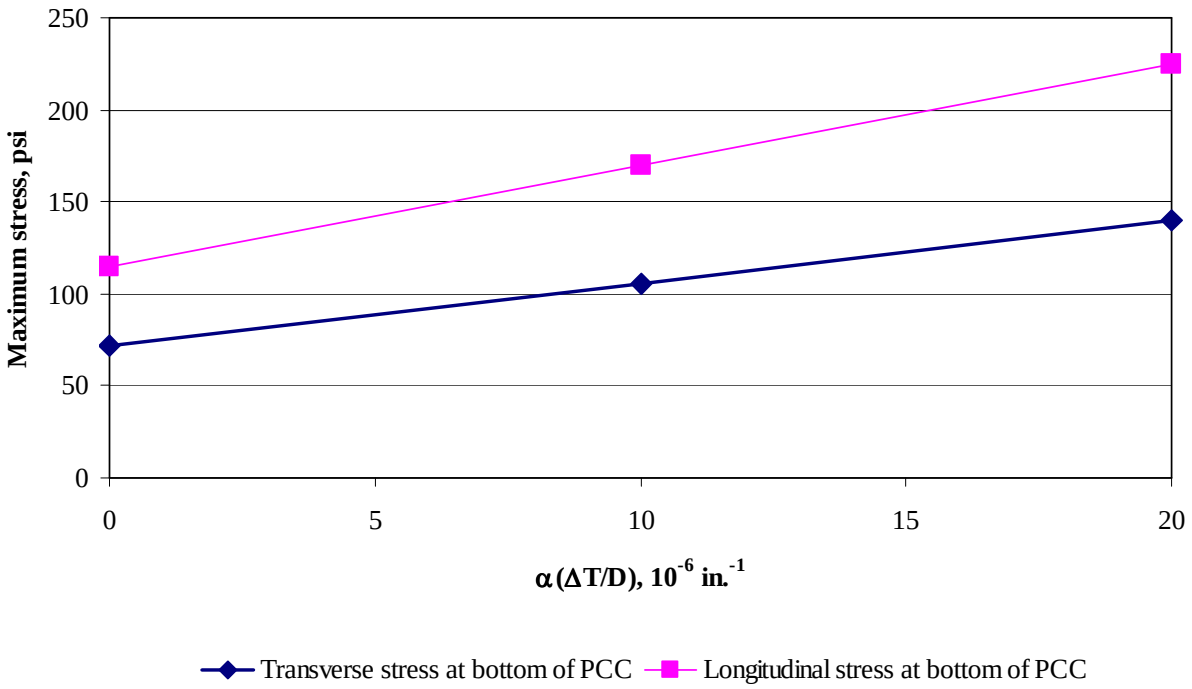

Figure 3-8: Sensitivity trend due to the variation in thermal strain gradient

3.3 Final Experimental Matrix

In addition to the above mentioned strategies, locations of stresses (at the bottom and the top of the PCC slab) are also effectively selected to reduce the number of runs. For positive thermal gradients, only stresses at the bottom of the PCC slab are considered, while stresses at the top of the PCC slab are considered for negative thermal gradients. The experimental matrix size has been reduced to 43,092 FE runs as illustrated in Table 3-3. It should be noted that all possible input parameters for all discrete variables and three levels of each non-discrete variable are addressed in this final experimental matrix. However, the combinations of non-discrete variables that are not addressed in this final experimental matrix are still of interest and will be obtained through the interpolation scheme, which is to be discussed later.

Table 3-3: Final experimental matrix

Input variables	Number of cases
PCC slab thickness	7 (6, 7,… 12 in.)
Base/subbase thickness	3 (4, 16, 26 in.)
Modulus of subgrade reaction	3 (30, ,100, 200 psi/in.)
Slab length (joint spacing)	2
Joint design	1
Shoulder type	3
$\alpha.\Delta T/D$	3 (0, ±10, ±20x10^{-6} in^{-1})
Location of stress	2
Load configuration	19
Total combinations	43,092

Chapter IV

PARAMETRIC STUDY

Based on a complete factorial of 43,092 combinations of parameters identified in the previous chapter, a preliminary parametric study is conducted by performing a series of FE analyses using the ISLAB2000 program. The results obtained from this parametric study are included in this chapter. The parametric study will be presented in four parts: structural model, analysis process, documentation of analysis results and interpretation of analysis results.

4.1 Structural Model

The pavement system for this analysis typically comprises of three to six PCC slabs, depending on the length of the load configuration. This is to ensure that the first and last PCC slabs are unloaded as recommended in Report 1-26 (NCHRP, 1990) to analyze the pavement system with extended slabs in order to reflect realistic boundary conditions that all the slabs are bounded by two slabs on both directions. Two lane widths (12 and 14 ft) and two shoulder types (untied AC and tied PCC) are considered. The study focuses on the analysis of the mechanistic responses in the outer lane (the truck lane), which is traditionally the design lane. Two joint spacings (177 and 315 in.) are considered. The structural model with two traffic lanes was not found to result in different pavement response in the outer wheel path as compared to the results obtained from the structural model with one traffic lane. Therefore, the second traffic lane is not included in the structural model to reduce the structure size and consequently analysis time. The wheel path considered in this study is 20 in. from center of outer wheel to the traffic stripe, similar to the pavement model used by Darter et al, 1994. Mesh size of 12x12 in. is used as a standard mesh size. This mesh size was found to achieve both satisfactory convergence and reasonable runtime. Figure 4-1 illustrates the typical slab structure layout as modeled using ISLAB2000.

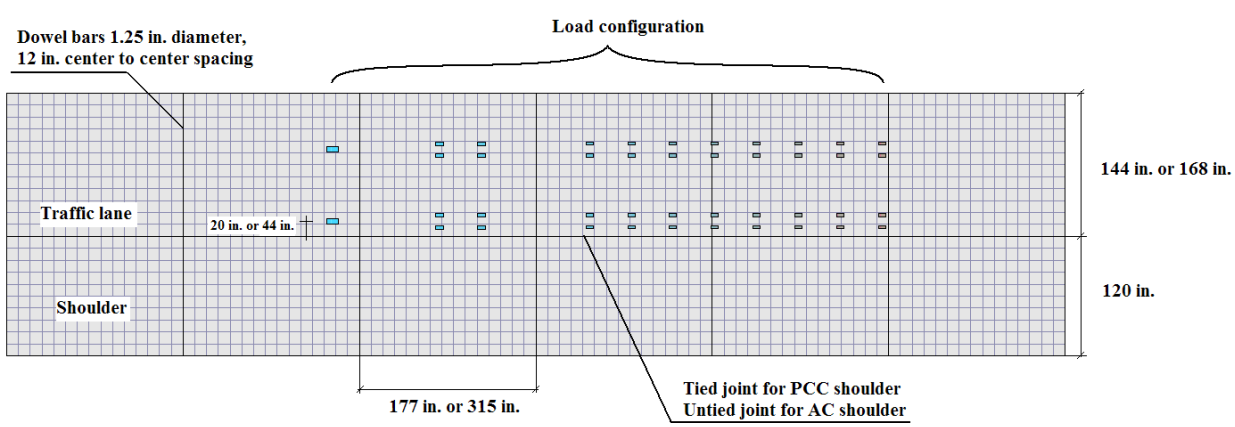

Figure 4-1: Overview of structural model

4.2 Analysis Process

The flow chart in Figure 4-2 illustrates the required components for the FE analysis. It can be seen that all structural and environmental factors have been addressed in the final experimental matrix. However, the critical load location needs to be derived first before the creation of the stress catalog. The critical load location is defined by the load location along the wheel path that results in the most critical mechanistic response, the highest value of the maximum responses for each load location.

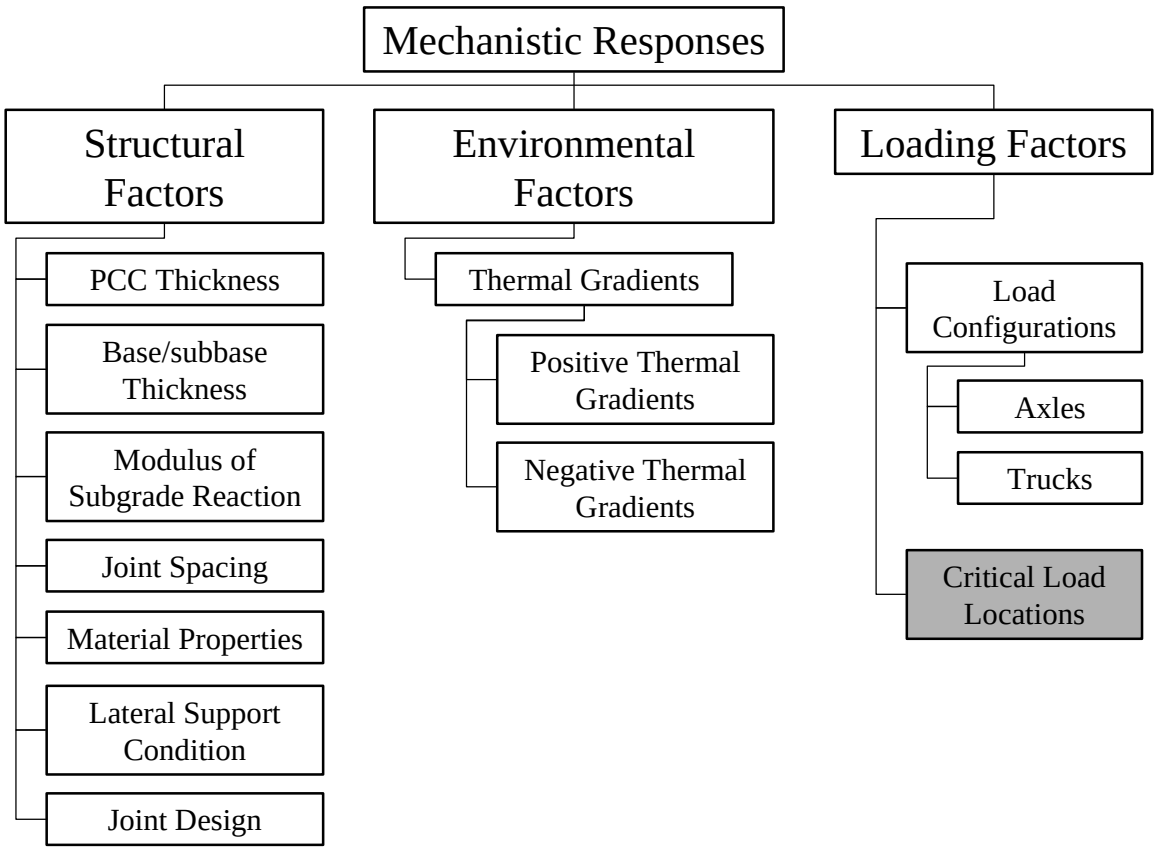

Figure 4-2: Required components for the analytical tool

Procedure of determining critical load location

The procedure for determining critical load location is illustrated in Figure 4-3. The procedure involves the computation of stresses at every load location along the wheel path along the slab length for a given set of conditions. The load location that results in the most critical (maximum) stress will be considered as the critical load location.

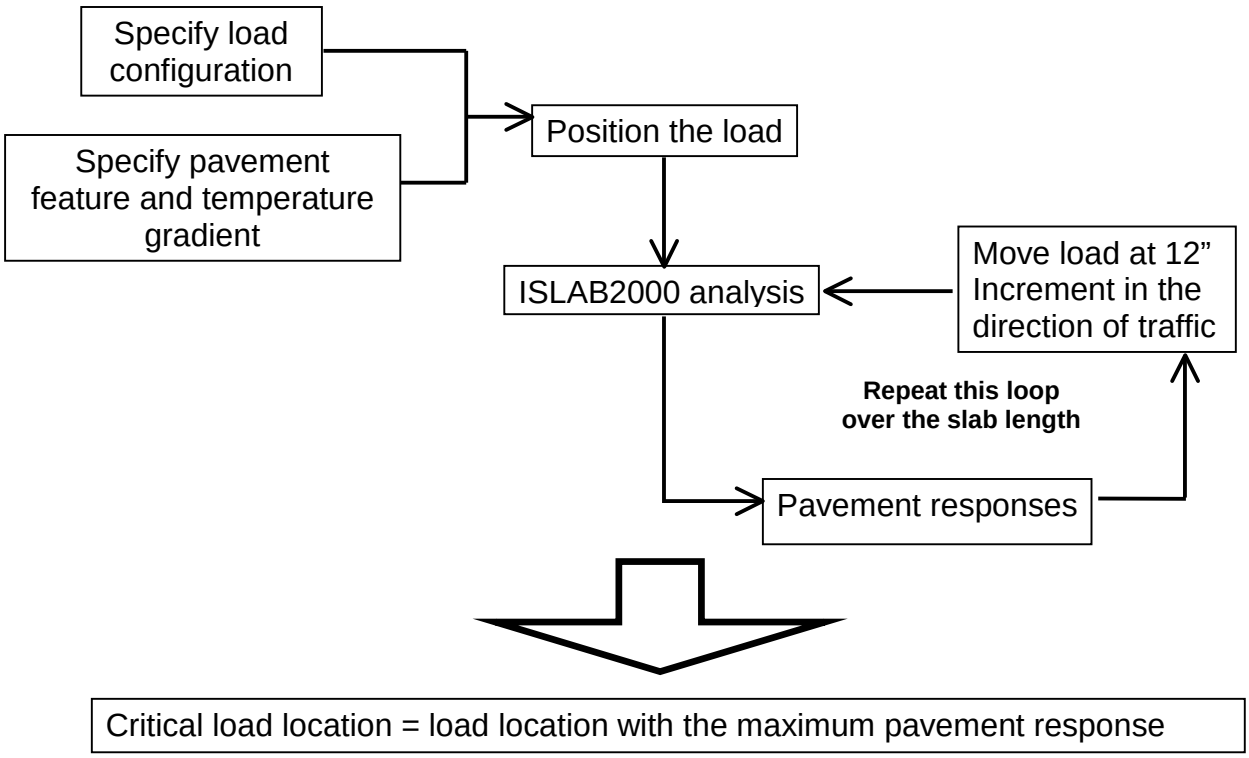

Figure 4-3: Procedure of determining critical load location

Assumptions and validation process

The procedure for determining critical load location is a time consuming process and is impractical to be performed for all possible combinations of input parameters in the final experimental matrix. It was assumed that variations in the following variables do not affect critical load locations:

- PCC thickness,
- Base/subbase thickness,
- k-value,
- Lateral support condition and
- Thermal strain gradient.

Validation of these assumptions was conducted to show that the critical load location is constant with the variation of the five non-influential variables. The fractional factorial design of $\frac{1}{3^3} \cdot 3^5 = 9$ is the method used to study the impact of variables within a practical size of validation matrix. The validation matrix used for all trucks and axles is summarized in Figure 4-4 (a). Note that fractional factorial design is a statistical method that allows for fractionation of a complete experimental factorial, while still balancing the fraction.

	Validation#1	Validation#2	Validation#3	Validation#4	Validation#5	Validation#6	Validation#7	Validation#8	Validation#9
Shoulder Type	PCC	AC	Widened Lane	PCC	AC	Widened Lane	PCC	AC	Widened Lane
PCC thickness, in.	10"	10"	10"	12"	12"	12"	8"	8"	8"
Base/subbase thickness, in.	16"	26"	4"	26"	4"	16"	4"	16"	26"
k-value, psi/in.	100	30	200	200	100	30	30	200	100
$\alpha.\Delta T/D$, $x10^{-6}$ in^{-1}	10	5	15	10	5	15	10	5	15
Location increment, in.	12	24	24	24	24	24	24	24	24

(a) Validation matrix

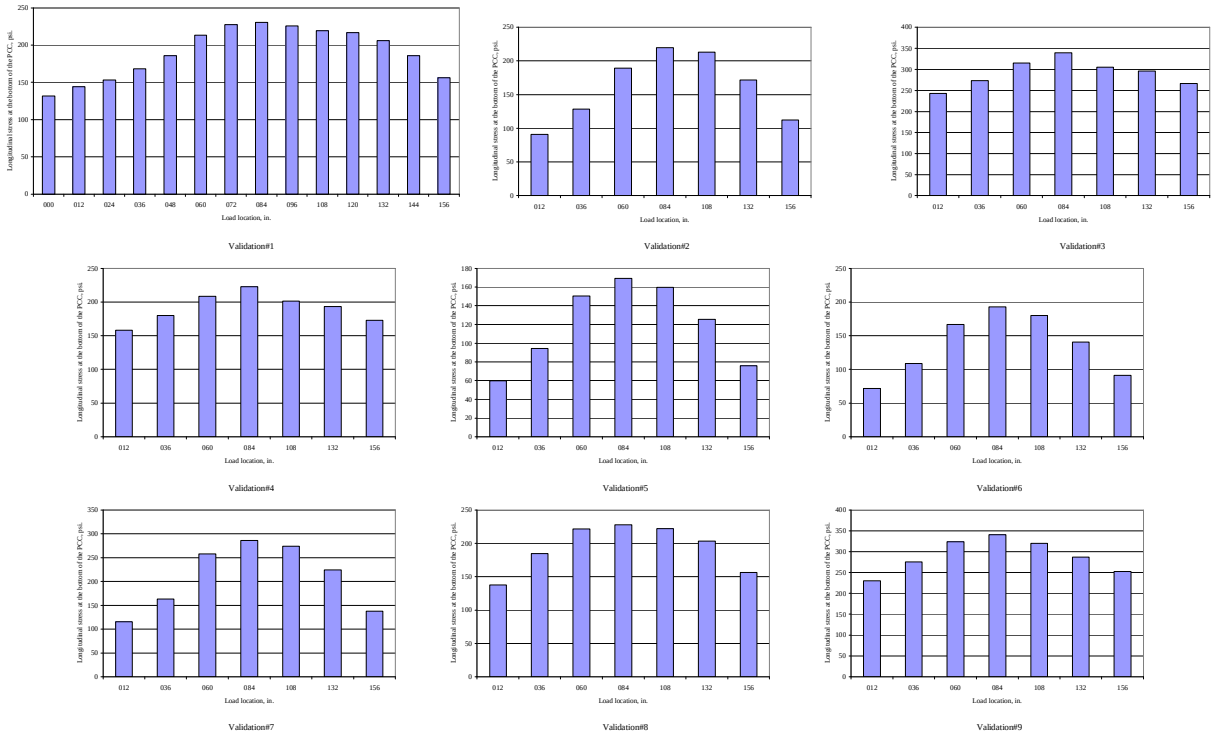

(b) Example validation and determination (bottom stresses, MI-16, 177-in. joint spacing)

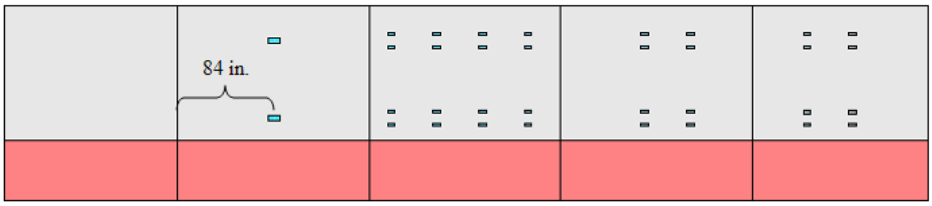

(c) Physical meaning of determined critical load location

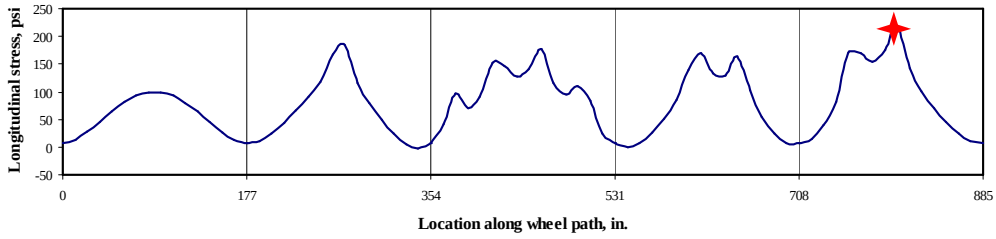

(d) Longitudinal stress profile and location of critical stress at critical load location for validation case 1

Figure 4-4: Validation and determination of critical load location

Figure 4-4 (b) illustrates an example of the assumption validation process used in the determination of the critical load location for bottom stresses for MI-16 on 177-in. joint spacing pavements. Stresses were computed for load locations along the wheel path for the nine validation cases as identified in Figure 4-4 (a). From the analysis results in Figure 4-4 (b), the non-influential variables were found to impact the stress magnitude; however, the non-influential variables did not significantly impact critical load location. For this example, the critical load location was approximately 84 in. for all the nine cases irrespective of the variation of the non-influential factors. Figure 4-4 (c) illustrates the physical meaning of the computed critical location in Figure 4-4 (b). An example stress profile for validation case 1 and the corresponding critical stress location are illustrated in Figure 4-4 (d). More example illustrations can be seen in Figures 4-5 and 4-6.

Figure 4-5: Example validation and determination (bottom stresses, MI-9, 177-in. joint spacing)

Figure 4-6: Example validation and determination (bottom stresses, MI-20, 177-in. joint spacing)

Table 4-1: Summary of critical load locations

Load configuration	For critical stress at the bottom of the PCC		For critical stress at the top of the PCC	
	177 in. joint spacing	315 in. joint spacing	177 in. joint spacing	315 in. joint spacing
Single axle	axle center at the midslab	axle center at the midslab	axle at the joint	axle at the joint
Tandem axle	axle center at the midslab	axle center at the midslab	1st set of two wheels at the joint	1st set of two wheels at the joint
Tridem axle	axle center at the midslab	axle center at the midslab	1st set of two wheels at the joint	3rd set of two wheels at the joint
Quad axle	axle center at the midslab	axle center at the midslab	1st set of two wheels at the joint	4th set of two wheels at the joint
Multi-axle 5	axle center at the midslab	axle center at the midslab	1st set of two wheels at the joint	5th set of two wheels at the joint
Multi-axle 6	axle center at the midslab	axle center at the midslab	1st set of two wheels at the joint	6th set of two wheels at the joint
Multi-axle 7	axle center at the midslab	axle center at the midslab	1st set of two wheels at the joint	7th set of two wheels at the joint
Multi-axle 8	axle center at the midslab	axle center at the midslab	1st set of two wheels at the joint	8th set of two wheels at the joint
MI-2	108 in. from the joint	48 in. from the joint	24 in. from the joint	240 in. from the joint
MI-7	at the joint	36 in. from the joint	96 in. from the joint	192 in. from the joint
MI-8	60 in. from the joint	96 in. from the joint	60 in. from the joint	264 in. from the joint
MI-9	132 in. from the joint	at the joint	60 in. from the joint	264 in. from the joint
MI-11	144 in. from the joint	36 in. from the joint	60 in. from the joint	264 in. from the joint
MI-12	144 in. from the joint	48 in. from the joint	48 in. from the joint	264 in. from the joint
MI-13	144 in. from the joint	156 in. from the joint	48 in. from the joint	264 in. from the joint
MI-16	84 in. from the joint	252 in. from the joint	156 in. from the joint	180 in. from the joint
MI-17	72 in. from the joint	156 in. from the joint	144 in. from the joint	180 in. from the joint
MI-19	144 in. from the joint	36 in. from the joint	48 in. from the joint	276 in. from the joint
MI-20	144 in. from the joint	36 in. from the joint	48 in. from the joint	252 in. from the joint

It is important to note that this process needs to be repeated for every axle and truck configuration, joint spacing, and stress location (top and bottom of the PCC slab) as these factors are considered influential in affecting critical load locations. Critical load locations for all eight axle configurations and 11 truck configurations are summarized in Table 4-1. Critical load locations for axle configurations were found to be in the vicinity of the middle of the slab and the transverse joint for stresses at the bottom and top of the PCC slab, respectively. However, no typical location was found for critical load locations for truck configurations due to the complex combinations of the axles and axle spacings within truck configurations.

4.3 Documentation of Analysis Results

Impact of structural factors, environmental factors, loading factors, and interaction between these factors on three types of mechanistic responses: longitudinal stress at the bottom of the PCC slab, transverse stress at the bottom of the PCC slab, and longitudinal stress at the top of the PCC slab is investigated.

Impact of structural factors

Figures 4-7 (a) through (f) are example illustrations of the impact of structural features on the longitudinal stress at the bottom of the PCC slab under various conditions as stated in the figures. Note that these figures represent MI-16 loading (see Figure 4-7 (c) for configuration), 16-in. base/subbase, 100-psi/in. k-value, PCC shoulder, and 177-in. joint spacing unless identified otherwise. All the figures show that PCC thickness has a significant impact in reducing stresses. In addition, the figures show that the changes in stresses due to changes in base/subbase thickness, k-value, and lateral support condition appear to be less relevant as the PCC slab becomes thicker. Also, joint spacing does not appear to have significant impact on edge stresses. Impact of lateral support condition will be discussed in detail later. Figures 4-7 (d) and (f) show an interaction of k-value and joint spacing with thermal gradients, which is to be discussed later. Although the magnitude of longitudinal stress at the bottom of the PCC slab were found to vary with combinations of input parameters, similar trends were observed in sensitivity plots over the entire experimental matrix. Similar trends were observed for the transverse stress at the bottom of the PCC slab with the exception of the impact of joint spacing, which was found to have no significant impact on the transverse stresses, even under the influence of a thermal gradient. An example critical location of stress is illustrated in Figure 4-7 (g).

The impact of structural features on longitudinal stress at the top of the PCC slab is illustrated in Figures 4-8 (a) through 4-8 (f). Note that these figures represent MI-16 loading (see Figure 3-4 (b) for configuration), 16-in. base/subbase, 100-psi/in. k-value, PCC shoulder, and 177-in. joint spacing the same conditions as previous parts unless identified otherwise. It can be seen in these figures that the magnitudes of longitudinal stresses at the top of the PCC slab are lower than the longitudinal stresses at the bottom of the PCC slab illustrated in the previous part. However, the trends observed for these stresses are similar. It should be noted that negative thermal gradients are considered in Figures 4-8 (d) and 4-8 (f), since the critical location of stresses is at the top of the PCC slab in these figures. An example critical location of stress is illustrated in Figure 4-8 (g).

Impact of loading factors

Figures 4-7 (h) and 4-8 (h) are example illustrations of the impact of the load configurations (axles and trucks) on the magnitude and normalized magnitude (by total weight of the configuration) of longitudinal stresses at the bottom and top of the PCC slab, respectively. In order to compare the contribution of each axle type (carrying different weight) on loading stress, it is necessary to express the stress as psi/kip. It can be seen that the normalized stress magnitudes are lower as the axle configurations have more load carrying wheels, implying that at the same stress level, a multi-axle can carry heavier loads than a single or tandem axle. However, the impact of truck configurations is not shown in these figures because each truck configuration makes various numbers of passes at the point of interest on the pavement slab. For example, the truck type MI-16 (see Figure 3-4 (b)) will result in four peaks of stresses corresponding to one single axle (driving axle), one quad axle, and two tandem axles. Hence, normalization based on total weight is not valid. The normalization should be based on the number of passes made by each axle group.

Impact of load lateral placement on mechanistic responses is presented in Figure 4-9 (a). Stresses were calculated for several load locations across the lane width. It was found that the PCC shoulder resulted in the lowest stresses among the three lateral support conditions considered in the study for the load located along the wheel path. It was found that the magnitudes of longitudinal stresses for AC shoulder (12-ft lane with AC shoulder) were higher than that for widened lane (also AC shoulder but with 14-ft lane). This could be attributed to the fact that a widened lane (14 ft.) creates a pseudo-interior loading condition (the wheel path shifted 2 ft towards the centerline, resulting in the reduction of stresses from edge loading). An example sensitivity plot of temperature-induced stresses in Figure 4-9 (b) illustrates that lateral support condition does not have a significant impact on temperature-induced stress in longitudinal direction. A series of sensitivity plots of the impact of lateral load placement on stresses for different lateral support conditions are presented in Appendix G.

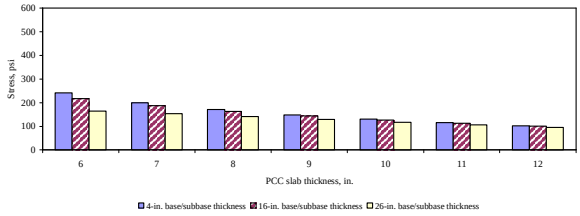

(a) Impact of base/subbase thickness, $\alpha(\Delta T/D) = 0x10^{-6}$ in.$^{-1}$

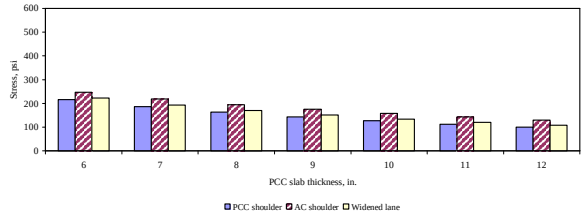

(b) Impact of lateral support condition, $\alpha(\Delta T/D) = 0x10^{-6}$ in.$^{-1}$

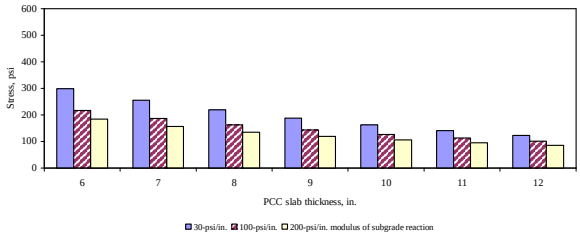

(c) Impact of modulus of subgrade reaction, $\alpha(\Delta T/D) = 0x10^{-6}$ in.$^{-1}$

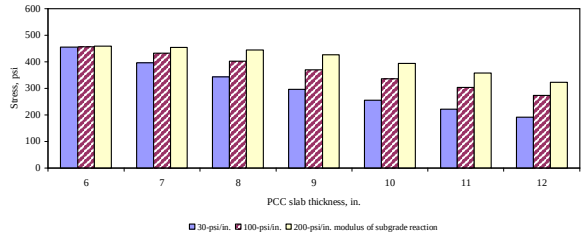

(d) Impact of modulus of subgrade reaction, $\alpha(\Delta T/D) = +20x10^{-6}$ in.$^{-1}$

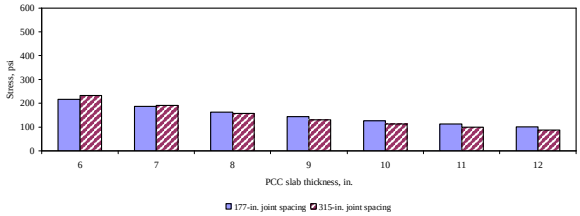

(e) Impact of joint spacing, $\alpha(\Delta T/D) = 0x10^{-6}$ in.$^{-1}$

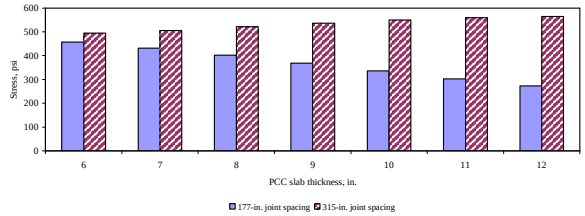

(f) Impact of joint spacing, $\alpha(\Delta T/D) = +20x10^{-6}$ in.$^{-1}$

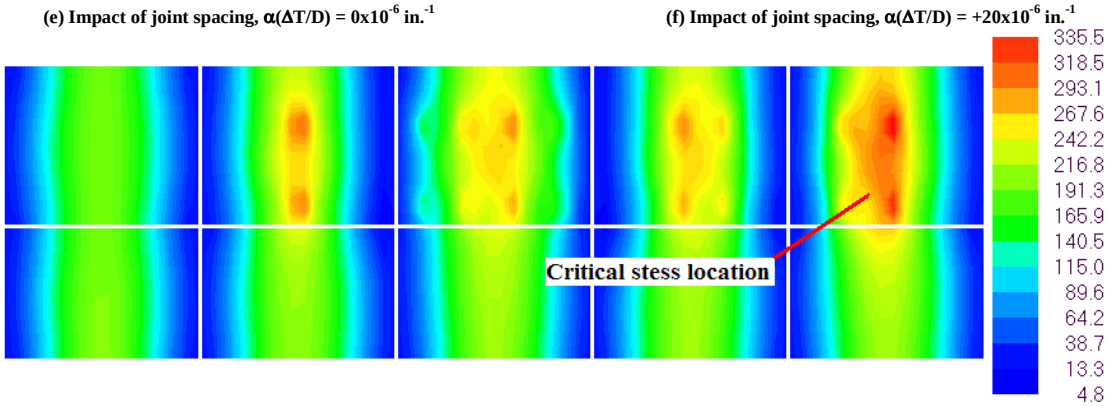

(g) Stress contour for 10-in. PCC slab, thermal strain gradient = $+20x10^{-6}$ in.$^{-1}$

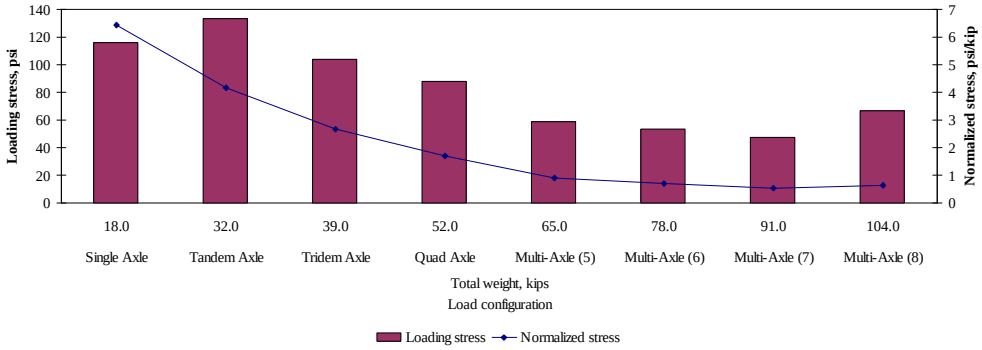

(h) 10-in. PCC slab, thermal strain gradient = $0x10^{-6}$ in.$^{-1}$

Figure 4-7: Example sensitivity plots of longitudinal stresses at the bottom of the PCC slab

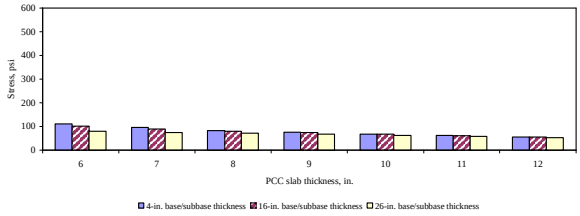

(a) Impact of base/subbase thickness, $\alpha(\Delta T/D) = 0x10^{-6}$ in.$^{-1}$

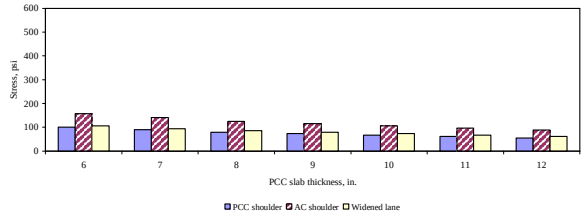

(b) Impact of lateral support condition, $\alpha(\Delta T/D) = 0x10^{-6}$ in.$^{-1}$

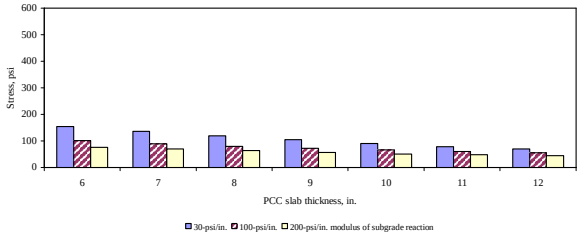

(c) Impact of modulus of subgrade reaction, $\alpha(\Delta T/D) = 0x10^{-6}$ in.$^{-1}$

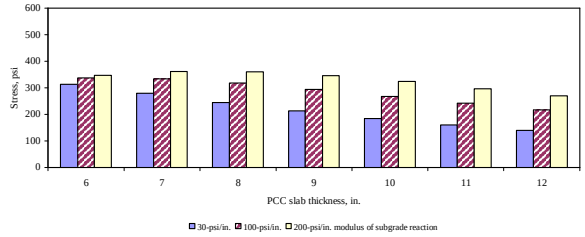

(d) Impact of modulus of subgrade reaction, $\alpha(\Delta T/D) = -20x10^{-6}$ in.$^{-1}$

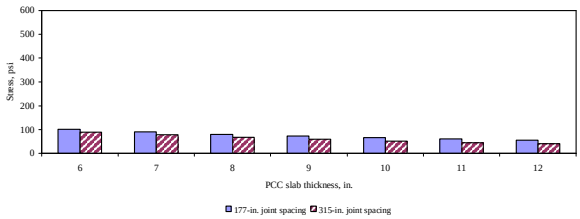

(e) Impact of joint spacing, $\alpha(\Delta T/D) = 0x10^{-6}$ in.$^{-1}$

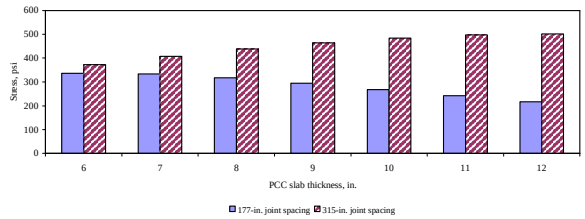

(f) Impact of joint spacing, $\alpha(\Delta T/D) = -20x10^{-6}$ in.$^{-1}$

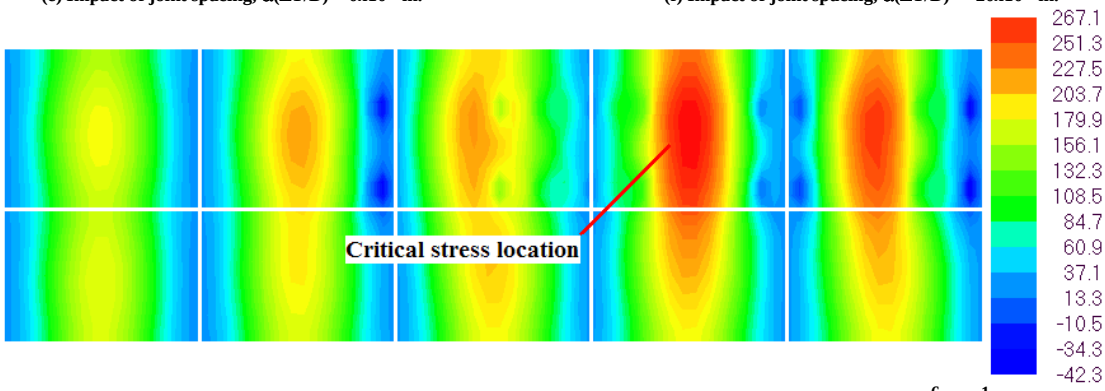

(g) Stress contour for 10-in. PCC slab, thermal strain gradient = $-20x10^{-6}$ in.$^{-1}$

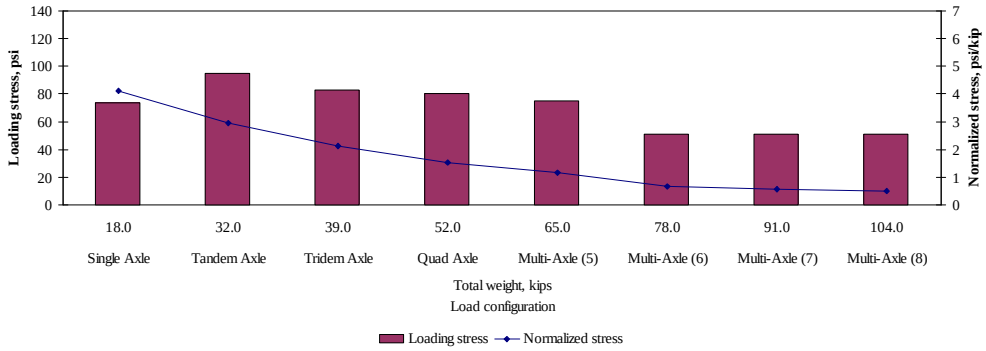

(h) 10-in. PCC slab, thermal strain gradient = $0x10^{-6}$ in.$^{-1}$

Figure 4-8: Example sensitivity plots of longitudinal stresses at the top of the PCC slab

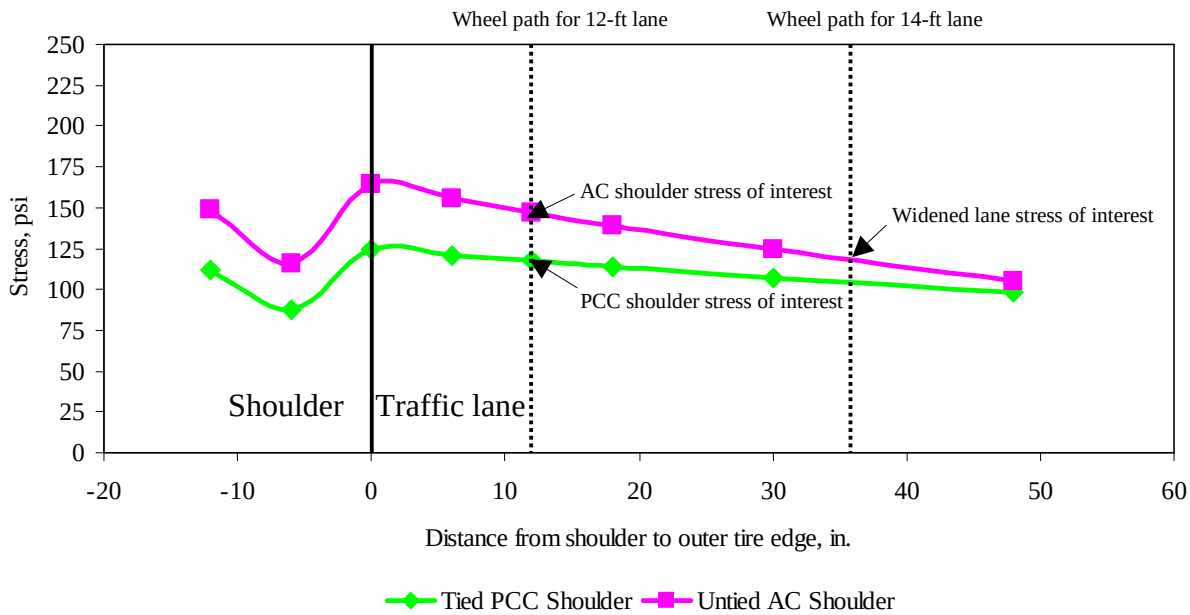

(a) Effect of load lateral placement on different lateral support conditions

Remarks: Longitudinal stresses at the bottom of the PCC slab, 10-in. PCC thickness, 16-in. base/subbase thickness, 100-psi/in. k-value, single axle, zero thermal gradient)

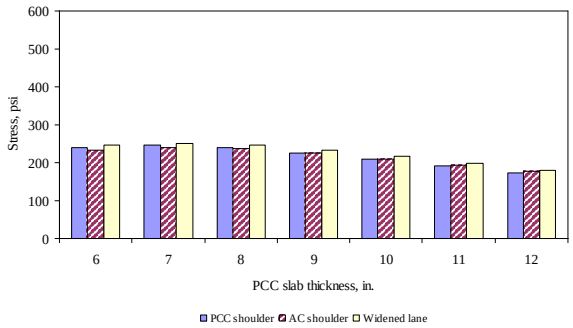

(b) Longitudinal temperature stress at the bottom of the PCC slab

Figure 4-9: Impact of lateral support condition

Impact of environmental factors

Environmental factors in this study are accounted in terms of thermal strain gradient (the product of CTE with positive or negative thermal gradients). As illustrated in Figures 4-10 (a) and (b), a positive gradient causes a downward curling of the slab, while a negative gradient causes an upward curling of the slab. The increase in magnitude of thermal gradient results in the increase in the magnitude of stresses, when positive and negative thermal gradients are considered in computation of stresses at the bottom and top of the PCC slab, respectively. As observed in the previous section (Figures 4-7 (d) and 4-8 (d)), the magnitude of the longitudinal stress appears to be impacted by the interaction between the thermal strain gradients, k-value and pavement thickness. This interactive trend is supported by the curling stress equations by Bradbury (Huang, 1993), where thermal curling stress is a function of finite slab correction factor. This

factor generally increases with the increase in the ratio of joint spacing (for longitudinal stresses) to radius of relative stiffness.

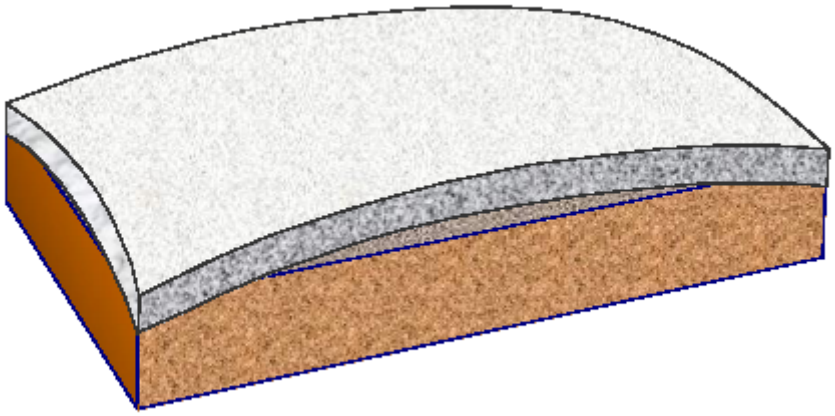

(a) Downward curling of slab due to a positive thermal gradient

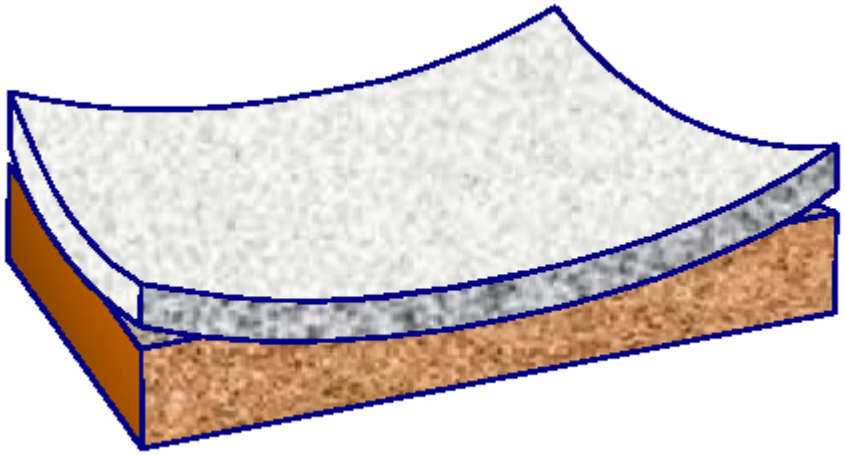

(b) Upward curling of slab due to a negative thermal gradient

Figure 4-10: Slab curling due to different types of thermal gradients (Yu et al, 2004)

Boundary support condition along the longitudinal joints of the slabs is characterized through AGG factor in ISLAB2000 program. It is crucial that an appropriate value of AGG factor is selected to represent the load transfer mechanism. The AGG factor can be empirically estimated as follows (Crovetti, 1994):

$$AGG = \left(\frac{\frac{1}{LTE} - 0.01}{0.012} \right)^{-\frac{1}{0.849}} \cdot k \cdot l \qquad (4\text{-}1)$$

Where	AGG	=	AGG factor
	LTE	=	Load transfer efficiency, percent
	ℓ	=	Radius of relative stiffness, in
	k	=	Modulus of subgrade reaction

The radius of relative stiffness is defined as follows:

$$l = \sqrt[4]{\frac{E \cdot h^3}{12\left(1-\mu^2\right) \cdot k}} \qquad (4\text{-}2)$$

Where	ℓ	=	Radius of relative stiffness, in
	E	=	Elastic modulus of layer 1
	h	=	Thickness of layer 1
	μ	=	Poisson's ratio for layer 1
	k	=	Modulus of subgrade reaction

In general, the typical values of LTE for tied PCC shoulder and untied AC shoulder vary from 25-90 % and 0-40 %, respectively. Based on equation 4-1, the ranges of AGG/kℓ were calculated as 0-0.77 and 0.34-16.5 for tied PCC shoulder and untied AC shoulder, respectively. Based on the inputs in the parametric study, the range of kℓ varies from 1188 to 8286 psi. A sensitivity study of the effect of AGG factor on magnitude of edge stresses is conducted for ranges of AGG factor from 5 to 7,000 psi (AC shoulder and widened lane) and from 300 to 2,500,000 psi (PCC shoulder). Based on these results, the AGG factors of 1,000,000 psi and 1,000 psi are selected for tied PCC shoulder and untied AC shoulder for the parametric study, respectively. Note that this sensitivity study is conducted for 177-in. joint spacing and 18-kips single axle at flat slab condition. Several sensitivity plots are generated as illustrated in Figures 4-11 (a) through 4-11 (c). It can be seen that the stress magnitude is not significantly sensitive to AGG factor for PCC shoulder and widened lane, while for AC shoulder the variation in stress magnitude could be up to 10% from stress magnitude computed based on the selected AGG factor (1,000 psi).

A complete documentation of interaction between all design parameters in the parametric study can be seen in Appendix F. Summary of the interaction is summarized in Table 4-2.

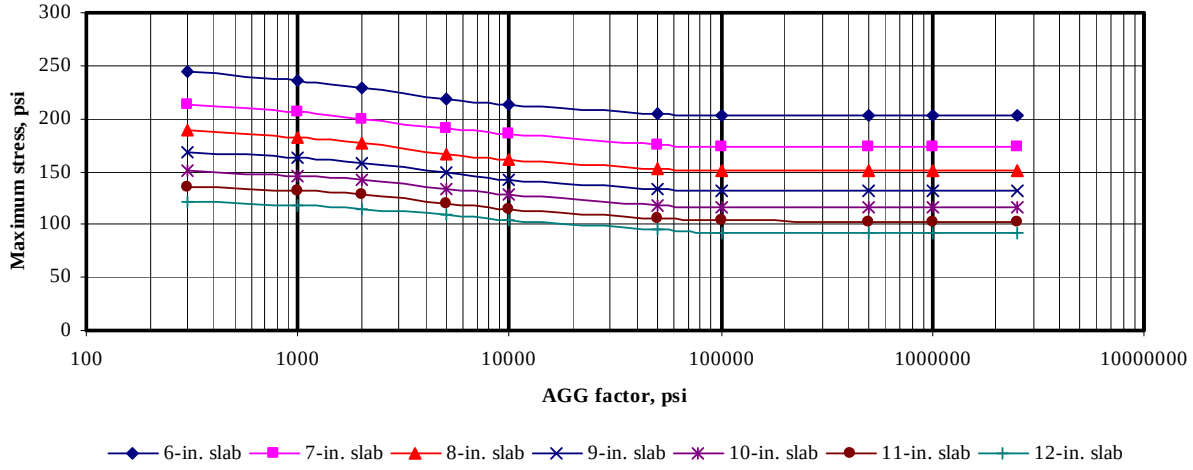

(a) PCC shoulder

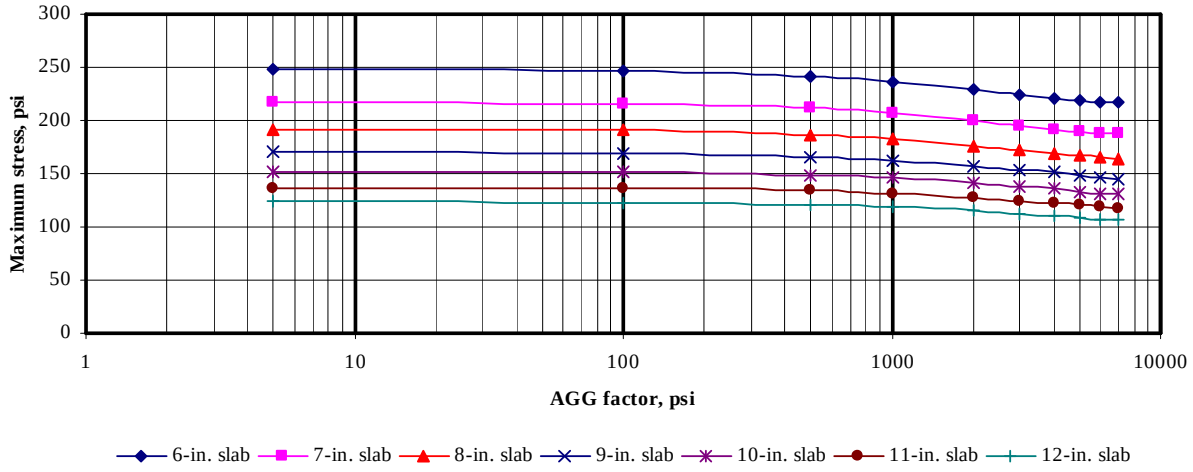

(b) AC shoulder

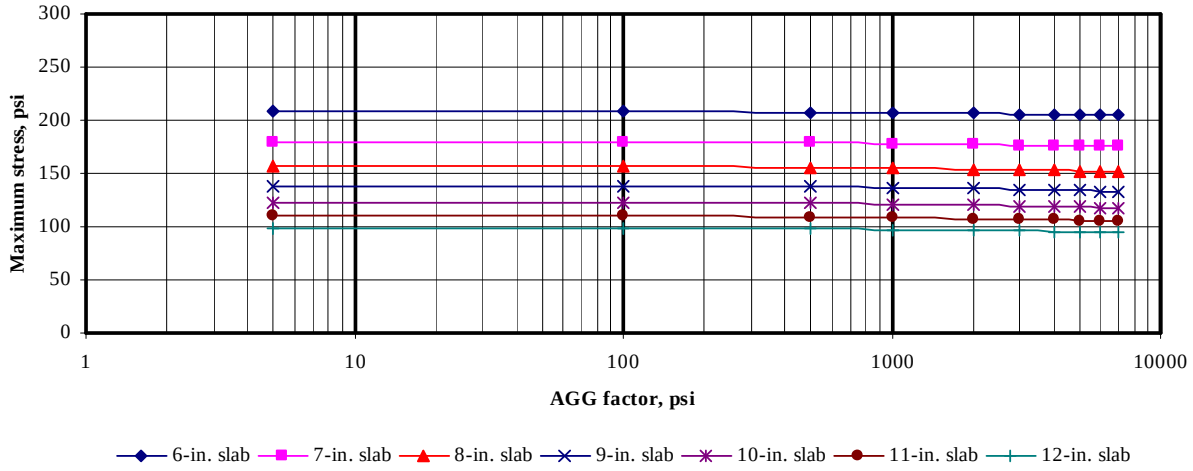

(c) Widened lane

Figure 4-11: Effect of longitudinal joint AGG factor on stress magnitude

Table 4-2: Summary of interaction between parameters on stresses

Parameters	Slab condition	Response type	Effects of parameters
PCC thickness versus base/subbase thickness	Flat slab	Longitudinal at bottom of PCC	Thicker base/subbase thickness results in lower stress, but smaller magnitude of stress reduction was observed with thicker PCC
		Longitudinal at top of PCC	Same as that for longitudinal stress at bottom of PCC
		Transverse at bottom of PCC	Same as that for longitudinal stress at bottom of PCC
	Curled slab	Longitudinal at bottom of PCC	With higher temperature differential (thicker PCC), thicker base/subbase thickness results in higher stress magnitude
		Longitudinal at top of PCC	Same as that for longitudinal stress at bottom of PCC
		Transverse at bottom of PCC	Same as that for longitudinal stress at bottom of PCC
PCC thickness versus modulus of subgrade reaction	Flat slab	Longitudinal at bottom of PCC	Higher value of modulus of subgrade reaction results in lower stress value. There is no significant interaction between these parameters observed.
		Longitudinal at top of PCC	Same as that for longitudinal stress at bottom of PCC
		Transverse at bottom of PCC	Same as that for longitudinal stress at bottom of PCC
	Curled slab	Longitudinal at bottom of PCC	Higher value of modulus of subgrade reaction results in higher stress value. Change in stress due to modulus of subgrade reaction is larger as temperature differential increases (PCC thickness increases), and eventually the change in stress will remain constant.
		Longitudinal at top of PCC	Same as that for longitudinal stress at bottom of PCC
		Transverse at bottom of PCC	Same as that for longitudinal stress at bottom of PCC
PCC thickness versus lateral support condition	Flat slab	Longitudinal at bottom of PCC	Higher stress value is observed in pavement with AC shoulder. There is no significant interaction between these parameters observed.
		Longitudinal at top of PCC	Same as that for longitudinal stress at bottom of PCC
		Transverse at bottom of PCC	The magnitude of stress are about the same for all three lateral support conditions. There is no significant interaction between these parameters observed.
	Curled slab	Longitudinal at bottom of PCC	Higher stress value is observed in pavement with AC shoulder. There is no significant interaction between these parameters observed.
		Longitudinal at top of PCC	Same as that for longitudinal stress at bottom of PCC
		Transverse at bottom of PCC	Higher stress value is observed in pavement with Widened lane. There is no significant interaction between these parameters observed.

Table 4-2: Summary of interaction between parameters on stresses (continued)

Parameters	Slab condition	Response type	Effects of parameters
Product of CTE with thermal gradient versus base/subbase thickness	177-in. joint spacing, curled slab	Longitudinal at bottom of PCC	Increase in product of CTE with thermal gradient linearly results in increase in stress magnitude. Interaction between these parameters is observed that increase in stress magnitude due to increase in product of CTE with thermal gradient is more intense with thicker base/subbase
		Longitudinal at top of PCC	Same as that for longitudinal stress at bottom of PCC
		Transverse at bottom of PCC	Same as that for longitudinal stress at bottom of PCC
	315-in. joint spacing, curled slab	Longitudinal at bottom of PCC	Increase in product of CTE with thermal gradient linearly results in increase in stress magnitude. However, the interaction observed for 177-in. joint spacing is not observed for this 315-in. joint spacing.
		Longitudinal at top of PCC	Increase in product of CTE with thermal gradient linearly results in increase in stress magnitude. However, the interaction observed for 177-in. joint spacing is not observed for this 315-in. joint spacing.
		Transverse at bottom of PCC	Same as that for 177-in. joint spacing
Product of CTE with thermal gradient versus base/subbase thickness	177-in. joint spacing, curled slab	Longitudinal at bottom of PCC	Increase in product of CTE with thermal gradient linearly results in increase in stress magnitude. Interaction between these parameters is observed that increase in stress magnitude due to increase in product of CTE with thermal gradient is more intense with higher value of moduluf of subgrade reaction
		Longitudinal at top of PCC	Same as that for longitudinal stress at bottom of PCC
		Transverse at bottom of PCC	Same as that for longitudinal stress at bottom of PCC
	315-in. joint spacing, curled slab	Longitudinal at bottom of PCC	Increase in product of CTE with thermal gradient linearly results in increase in stress magnitude. However, the interaction observed for this 315-in. joint spacing is not as intense as that for 177-in. joint spacing.
		Longitudinal at top of PCC	Increase in product of CTE with thermal gradient linearly results in increase in stress magnitude. However, the interaction observed for this 315-in. joint spacing is not as intense as that for 177-in. joint spacing.
		Transverse at bottom of PCC	Same as that for 177-in. joint spacing
Product of CTE with thermal gradient versus joint spacing	Curled slab	Longitudinal at bottom of PCC	Increase in product of CTE with thermal gradient linearly results in increase in stress magnitude. Interaction between these parameters is observed that increase in stress magnitude due to increase in product of CTE with thermal gradient is more intense with longer joint spacing.
		Longitudinal at top of PCC	Same as that for longitudinal stress at bottom of PCC
		Transverse at bottom of PCC	Increase in product of CTE with thermal gradient linearly results in increase in stress magnitude. Joint spacing has no significant impact on stress magnitude.

4.4 Possible Application of Analysis Results

Although pavements experience a wide variety of stress magnitudes, the preliminary results obtained from the parametric study can be used to obtain pavement cross-sections that will likely have the same stress level. Through the application of the interpolation scheme (to be discussed in the Chapter 5), several pavement design alternatives with the same level of loading stress can be obtained. For example, three cross-sections in Figure 4-12 have different design parameters, but they experience the same level of stress. This application offers the pavement engineers more design alternatives with the same behavior (response) from the mechanistic standpoint. An extensive set of equivalent stress cross-sections is presented in Appendix H.

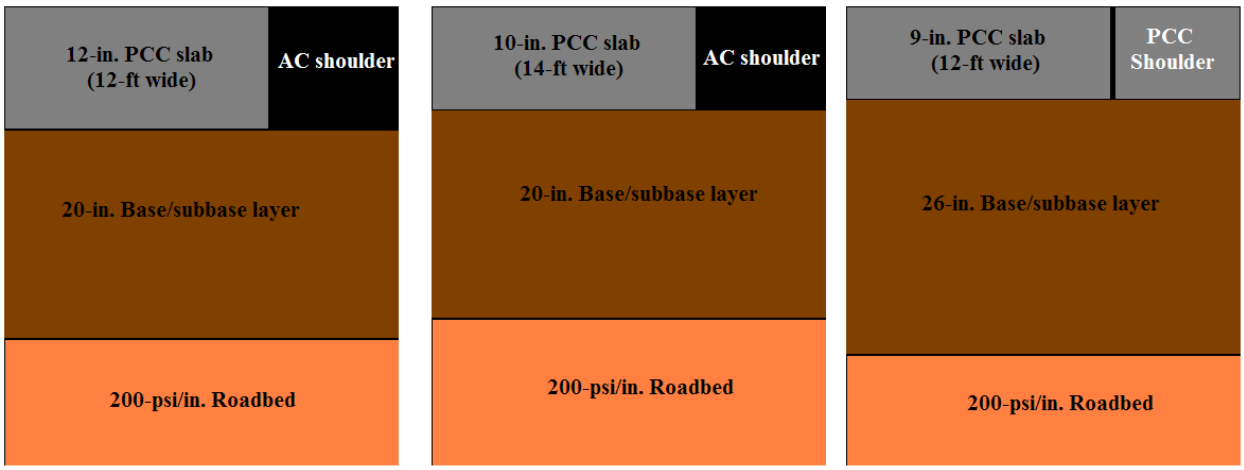

Figure 4-12: Example illustrations of equivalent stress sections (100 psi stress level under 18-kips single axle)

Chapter V

INTERPOLATION SCHEME

Interpolation scheme is a statistical procedure used to approximate unknown values (non-nodal points) in the vicinity of known values (nodal points). Interpolation scheme in this project is used because it is required to obtain mechanistic responses for all the combinations of the non-discrete inputs, not addressed in the final experimental matrix. The experimental matrix includes all possibilities of all the discrete design inputs: PCC thickness, joint spacing, lateral support condition, and load configuration. However, only three values were specified for each of these non-discrete inputs in the final experimental matrix:

- k-value (30 psi/in., 100 psi/in., 200 psi/in.),
- Base/subbase thickness (4 in., 16 in., 26 in.),
- Thermal strain gradients (0 in.$^{-1}$, ±10x10^{-6} in.$^{-1}$, ±20x10^{-6} in.$^{-1}$).

Since the interpolation process in this study is used to approximate the results that are not directly analyzed by the FE model across ranges of the three non-discrete input parameters: modulus of subgrade reaction, base/subbase thickness, thermal strain gradient, this interpolation scheme is a three-dimensional process.

5.1 Least-Squares Criteria

The statistical method least-square approximation, proposed by the German mathematician Carl Friedrich Gauss in 1795, is applied to develop and evaluate interpolation schemes in this study. In general, the method is unbiased and algebraically provides an approximation to a dependent (response) variable *Y* that has the lowest variance. This research study focuses on three response variables: longitudinal stress at the top of the PCC, longitudinal stress at the bottom of the PCC, and transverse stress at the bottom of the PCC. With a linear model, coefficients β_j for the least-squares solution satisfy the normal equations:

$$\frac{\partial\left(\sum_{i=1}^{n} e_i^2\right)}{\partial \beta_j} = 0 \quad , j = 0, 1, 2, \ldots, m \tag{5-1}$$

where Y_i is the value of variable *Y* at point *i*, $y_i = \beta_0 + \beta_1 \cdot x_i^1 + \beta_2 \cdot x_i^2 + \beta_3 \cdot x_i^3 + \ldots + \beta_m \cdot x_i^m$ is the predicted value at point *i*, $e_i = Y_i - y_i$ is error of the predicted value, and $x_i^1, x_i^2, x_i^3, \ldots x_i^m$ are independent (predictor) variables evaluated at point *i*, *i* = 1, 2, …, *n*.

The matrix formulation of the solution in the nonsingular case is:

$$y_i = \beta_0 + \beta_1 \cdot x_i^1 + \beta_2 \cdot x_i^2 + \beta_3 \cdot x_i^3 + \ldots + \beta_m \cdot x_i^m = \overline{x}_i \cdot \overline{\beta} \tag{5-2}$$

$$\bar{x}_i = \begin{Bmatrix} 1 & x_i^1 & x_i^2 & \dots & x_i^m \end{Bmatrix} \tag{5-3}$$

$$\bar{\beta} = \begin{Bmatrix} \beta_0 \\ \beta_1 \\ \beta_2 \\ \vdots \\ \beta_m \end{Bmatrix} = \left[X^T \cdot X\right]^{-1} \cdot X^T \cdot \bar{Y} \tag{5-4}$$

$$X = \begin{Bmatrix} \bar{x}_1 \\ \bar{x}_2 \\ \bar{x}_3 \\ \vdots \\ \bar{x}_n \end{Bmatrix} = \begin{Bmatrix} 1 & x_1^1 & x_1^2 & \cdots & x_1^m \\ 1 & x_2^1 & x_2^2 & \cdots & x_2^m \\ 1 & x_3^1 & x_3^2 & \dots & x_3^m \\ \vdots & \vdots & \vdots & & \vdots \\ 1 & x_n^1 & x_n^2 & \cdots & x_n^m \end{Bmatrix} \tag{5-5}$$

$$\bar{Y} = \begin{Bmatrix} Y_1 \\ Y_2 \\ Y_3 \\ \vdots \\ Y_n \end{Bmatrix} \tag{5-6}$$

The matrix formulation of the least-squares criteria is used to describe the interpolation process which will be discussed later.

5.2 Development of Interpolation Scheme

First, a sensitivity study was conducted to investigate the impact of the three non-discrete input parameters. The impact of modulus of subgrade reaction and base/subbase thickness on the magnitude of stresses were found to be highly non-linear as the change in the slope of the relationship was observed. On the other hand, initial trials showed the impact of thermal strain gradient to have little curvature. Therefore, the interpolation process is divided into two steps: (i) two-dimensional interpolation based on known anchor results obtained from the FE model across ranges of base/subbase thickness and modulus of subgrade reaction at each level of thermal strain gradient, and (ii) one-dimensional interpolation based on the interpolated results from step 1 across range of thermal strain gradient. The interpolation is illustrated in Figure 5-1. Using the least-squares criteria, several interpolation schemes were developed and compared as discussed later. The prototype of the interpolation scheme is explained below in matrix form.

<u>Step 1</u>:

$$\sigma\left(H^*, k^*, \alpha_i\right) = \bar{X}^* \cdot \hat{\beta} \tag{5-7}$$

Where $\sigma\left(H^*, k^*, \alpha_i\right)$ is mechanistic response for the target combination of base/subbase thickness and modulus of subgrade reaction at level α_i of thermal strain gradient

$\overline{X}*$ is the vector of predictor variables

$$\overline{X}* = \left\{ 1 \quad H* \quad H*^2 \quad \ln(k*) \quad H* \cdot \ln(k*) \quad H*^2 \cdot \ln(k*) \quad \frac{1}{k*} \quad \frac{H*}{k*} \quad \frac{H*^2}{k*} \right\} \tag{5-8}$$

Where H* is target base/subbase thickness
k* is target modulus of subgrade reaction
α_1 is anchor value 0 in.$^{-1}$ of thermal strain gradient
α_2 is anchor value ±10x10^{-6} in.$^{-1}$ of thermal strain gradient
α_3 is anchor value ±20x10^{-6} in.$^{-1}$ of thermal strain gradient
$\hat{\beta}$ is least-squares coefficient vector

$$\hat{\beta} = \begin{Bmatrix} \beta_0 \\ \beta_1 \\ \beta_2 \\ \beta_3 \\ \beta_4 \\ \beta_5 \\ \beta_6 \\ \beta_7 \\ \beta_8 \end{Bmatrix} = \left[X^T \cdot X \right]^{-1} \cdot X^T \cdot \hat{\sigma} \tag{5-9}$$

$$X = \begin{Bmatrix} \overline{X}(H_1,k_1) \\ \overline{X}(H_1,k_2) \\ \overline{X}(H_1,k_3) \\ \overline{X}(H_2,k_1) \\ \overline{X}(H_2,k_2) \\ \overline{X}(H_2,k_3) \\ \overline{X}(H_3,k_1) \\ \overline{X}(H_3,k_2) \\ \overline{X}(H_3,k_3) \end{Bmatrix} = \begin{bmatrix} 1 & H_1 & H_1^2 & \ln(k_1) & H_1 \cdot \ln(k_1) & H_1^2 \cdot \ln(k_1) & \frac{1}{k_1} & \frac{H_1}{k_1} & \frac{H_1^2}{k_1} \\ 1 & H_1 & H_1^2 & \ln(k_2) & H_1 \cdot \ln(k_2) & H_1^2 \cdot \ln(k_2) & \frac{1}{k_2} & \frac{H_1}{k_2} & \frac{H_1^2}{k_2} \\ 1 & H_1 & H_1^2 & \ln(k_3) & H_1 \cdot \ln(k_3) & H_1^2 \cdot \ln(k_3) & \frac{1}{k_3} & \frac{H_1}{k_3} & \frac{H_1^2}{k_3} \\ 1 & H_2 & H_2^2 & \ln(k_1) & H_2 \cdot \ln(k_1) & H_2^2 \cdot \ln(k_1) & \frac{1}{k_1} & \frac{H_2}{k_1} & \frac{H_2^2}{k_1} \\ 1 & H_2 & H_2^2 & \ln(k_2) & H_2 \cdot \ln(k_2) & H_2^2 \cdot \ln(k_2) & \frac{1}{k_2} & \frac{H_2}{k_2} & \frac{H_2^2}{k_2} \\ 1 & H_2 & H_2^2 & \ln(k_3) & H_2 \cdot \ln(k_3) & H_2^2 \cdot \ln(k_3) & \frac{1}{k_3} & \frac{H_2}{k_3} & \frac{H_2^2}{k_3} \\ 1 & H_3 & H_3^2 & \ln(k_1) & H_3 \cdot \ln(k_1) & H_3^2 \cdot \ln(k_1) & \frac{1}{k_1} & \frac{H_3}{k_1} & \frac{H_3^2}{k_1} \\ 1 & H_3 & H_3^2 & \ln(k_2) & H_3 \cdot \ln(k_2) & H_3^2 \cdot \ln(k_2) & \frac{1}{k_2} & \frac{H_3}{k_2} & \frac{H_3^2}{k_2} \\ 1 & H_3 & H_3^2 & \ln(k_3) & H_3 \cdot \ln(k_3) & H_3^2 \cdot \ln(k_3) & \frac{1}{k_3} & \frac{H_3}{k_3} & \frac{H_3^2}{k_3} \end{bmatrix} \tag{5-10}$$

Where H_1 is anchor value base/subbase thickness of 4 in.
H_2 is anchor value base/subbase thickness of 16 in.
H_3 is anchor value base/subbase thickness of 26 in.
k_1 is anchor value modulus of subgrade reaction of 30 psi/in.
k_2 is anchor value modulus of subgrade reaction of 100 psi/in.

k_3 is anchor value modulus of subgrade reaction of 200 psi/in.

$$\hat{\sigma} = \begin{Bmatrix} \sigma_{11} \\ \sigma_{12} \\ \sigma_{13} \\ \sigma_{21} \\ \sigma_{22} \\ \sigma_{23} \\ \sigma_{31} \\ \sigma_{32} \\ \sigma_{33} \end{Bmatrix} \tag{5-11}$$

Where σ_{ij} is known anchor value stress from FE analysis at H_i and k_j

<u>Step 2</u>:

$$\sigma(H^*, k^*, \alpha^*) = \overline{\alpha}^* \cdot \hat{\gamma} \tag{5-12}$$

Where $\sigma(H^*, k^*, \alpha^*)$ is mechanistic response for the target combination of base/subbase thickness, modulus of subgrade reaction, and product of α(ΔT/D)
$\overline{\alpha}^*$ is the vector of predictor variables based on α(ΔT/D)

$$\overline{\alpha}^* = \begin{Bmatrix} 1 & \alpha^* & \alpha^{*2} \end{Bmatrix} \tag{5-13}$$

$$\hat{\gamma} = \begin{Bmatrix} \gamma_0 \\ \gamma_1 \\ \gamma_2 \end{Bmatrix} = \begin{bmatrix} 1 & \alpha_1 & \alpha_1^2 \\ 1 & \alpha_2 & \alpha_2^2 \\ 1 & \alpha_3 & \alpha_3^2 \end{bmatrix}^{-1} \cdot \begin{Bmatrix} \sigma(H^*, k^*, \alpha_1) \\ \sigma(H^*, k^*, \alpha_2) \\ \sigma(H^*, k^*, \alpha_3) \end{Bmatrix} \tag{5-14}$$

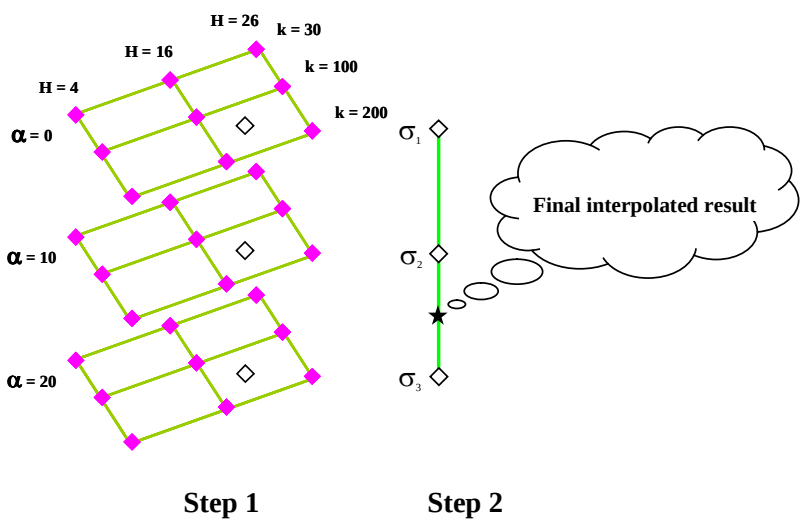

Figure 5-1: Interpolation process

Several interpolation schemes were developed following this prototype with different terms used in the prediction vectors (8) in step 1 and (13) in step 2. Examples of prediction vectors used in some of the schemes developed in this study are given in Table 5-1. It should be noted that the natural logarithm of modulus of subgrade reaction and the interaction terms with base/subbase thickness in the prediction matrices for schemes 15 and 16 are similar to terms suggested in the Westergaard's closed form stress equations (Huang, 1993). A significant drop in error due to the use of these terms was observed. Comparing the interpolated results with FE results at non-nodal points validates these two interpolation schemes. Also note that the solutions to the normal equations for schemes 15 and 16 produce perfect fits at the nine nodal points corresponding to each level of the product $\alpha(\Delta T/D)$. Several more schemes have also been investigated. Most of these schemes that contain high order interaction term(s) in "step 1", e.g. $H^{*2}k^{*2}$, $H^{*}k^{*3}$, $H^{*3}k^{*}$, were found to result in low predictive power.

Table 5-1: Example prediction matrices

Scheme No.	Prediction Matrix for Step 1	Prediction Matrix for Step 2
Scheme 5	$\{1 \quad (H^*) \quad (k^*) \quad (H^*)^2 \quad (k^*)^2 \quad (H^*k^*)\}$	$\{1 \quad \alpha^*\}$
Scheme 6	$\{1 \quad (H^*) \quad (k^*) \quad (H^*)^2 \quad (k^*)^2 \quad (H^*k^*) \quad (H^*/k^*)^{0.5}\}$	$\{1 \quad \alpha^*\}$
Scheme 9	$\{1 \quad (H^*) \quad (k^*) \quad (H^*)^2 \quad (k^*)^2 \quad (H^*k^*) \quad (H^{*2}k^*)\}$	$\{1 \quad \alpha^*\}$
Scheme 10	$\{1 \quad (H^*) \quad (k^*) \quad (H^*)^2 \quad (k^*)^2 \quad (H^*k^*) \quad (H^*k^{*2})\}$	$\{1 \quad \alpha^*\}$
Scheme 15	$\{1 \quad (H^*) \quad (H^*)^2 \quad (\ln k^*) \quad (H^*\ln k^*) \quad (H^{*2}\ln k^*) \quad (1/k^*) \quad (H^*/k^*) \quad (H^{*2}/k^*)\}$	$\{1 \quad \alpha^*\}$
Scheme 16	$\{1 \quad (H^*) \quad (H^*)^2 \quad (\ln k^*) \quad (H^*\ln k^*) \quad (H^{*2}\ln k^*) \quad (1/k^*) \quad (H^*/k^*) \quad (H^{*2}/k^*)\}$	$\{1 \quad \alpha^* \quad \alpha^{*2}\}$

5.3 Validation and Goodness of Fit

The validation process is illustrated in Figures 5-2 and 5-3. This process involves obtaining FE results at non-nodal points that were not used in developing interpolation schemes. Error is defined as the difference between the interpolated result and the FE result directly obtained from the ISLAB2000.

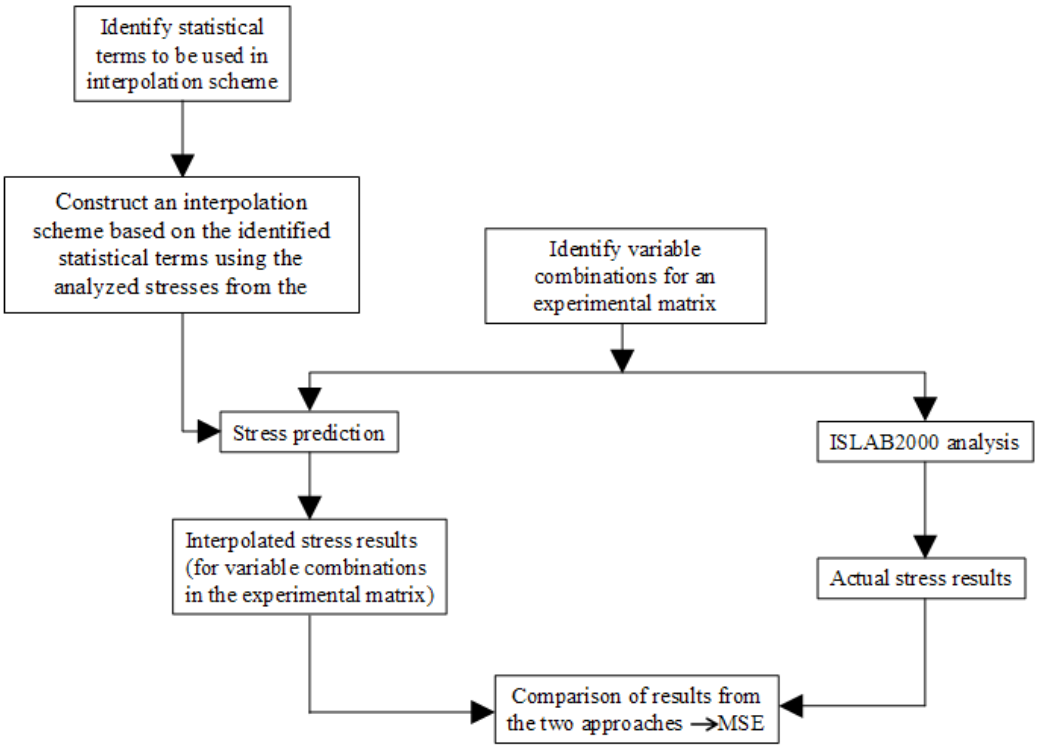

Figure 5-2: Validation procedure

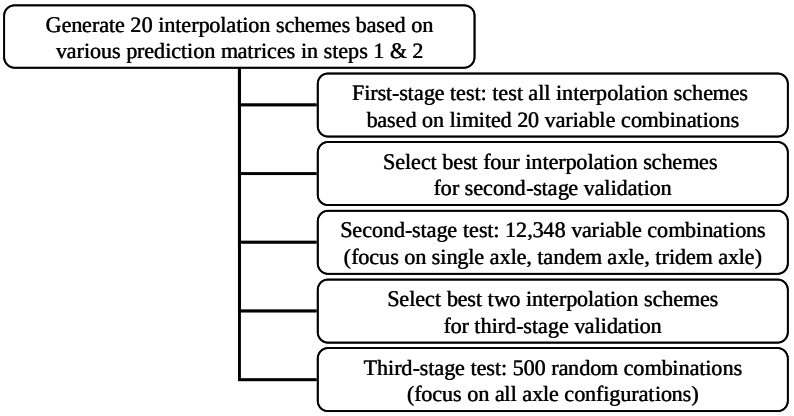

Figure 5-3: Overview of validation process

More than 12,000 non-nodal FE results have been obtained and used to validate and select from interpolation schemes. The three stages of the validation process are as follow:

Validation Stage 1: In the first stage, all interpolation schemes that were developed are validated with a limited number of non-nodal points. The validation matrix covers 20 non-nodal points with variations of all three non-discrete variables for a fixed combination of discrete variables (10-in. PCC thickness, 16-in. base/subbase thickness, 177-in. joint spacing, PCC shoulder, and single axle edge loading). Non-nodal points at the middle in between the anchor values are considered in this validation stage. These non-nodal points are believed to result in large magnitudes of errors since they are far from the anchor values. Mean square of errors (MSE), bias, and variance are the measures of the goodness of fit of the interpolation schemes considered in this study, which will be discussed later. These values were calculated for the errors (difference between the FE results and interpolated results) obtained from the validation process. Figures 5-4 (a) through (e) illustrate the validation results at the first stage for six most promising interpolation schemes. The comparison between FE and interpolated results illustrated in Figure 5-4 (a) suggests that all these schemes have high predictive power. However, based on MSE, bias, and variance in Figures 5-4 (b) through (e), schemes 5, 6, 15, and 16 appear to be the best four performing interpolation schemes, and consequently are selected for the next stage of validation.

Validation Stage 2: The validation matrix for this stage consists of 12,348 non-nodal points. The experimental matrix of "validation stage 2" is a complete factorial of all discrete variable and five values of each of the three non-discrete variables (including two mid points). The process focuses on single, tandem, and tridem axles for all non-discrete and discrete variables. The middle points between nodal points are also used for this validation stage. The validation results are illustrated in Figures 5-5 (a) through (e). Based on the validation results, the two best performing schemes are 15 and 16.

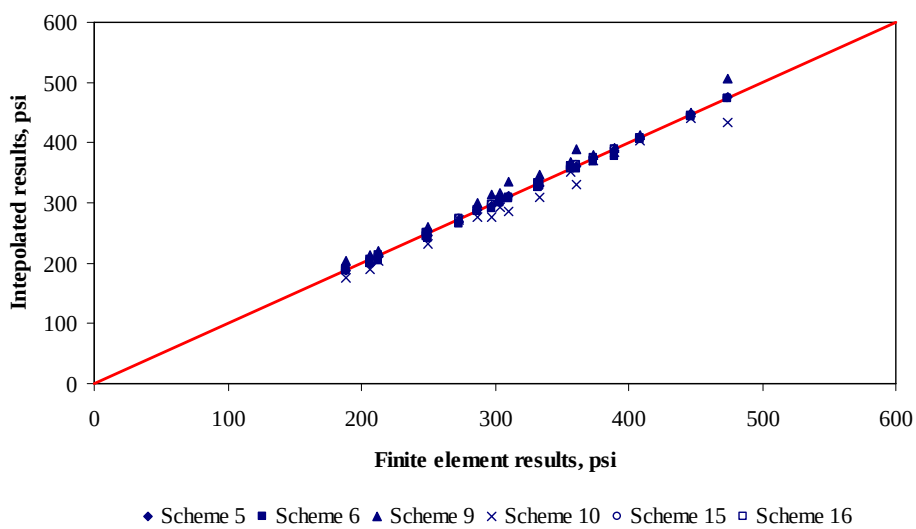

(a) Comparison between FE and interpolated results

Figure 5-4: Validation results – stage 1

Goodness of Fit	Scheme 5	Scheme 6	Scheme 9	Scheme 10	Scheme 15	Scheme 16
MSE, psi^2	6.34	32.29	202.31	267.70	1.24	1.22
Variance, psi^2	6.23	13.64	69.31	120.71	1.08	1.07
Absolute Bias, psi	0.33	4.32	11.53	12.12	0.40	0.39

(b) Summary of goodness of fit

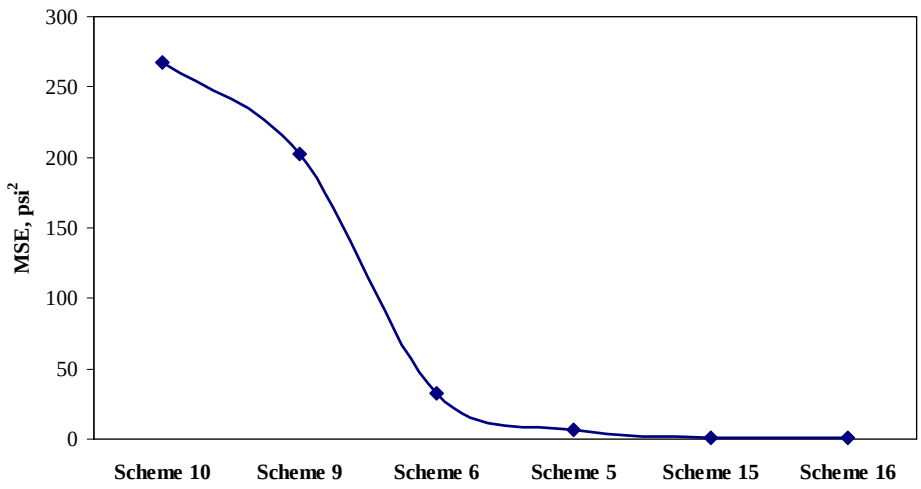

(c) Comparison of MSE

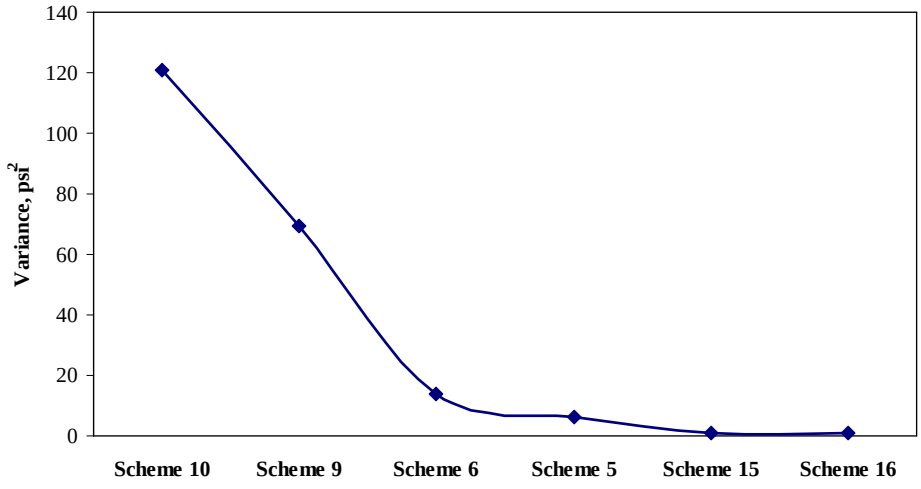

(d) Comparison of variance

Figure 5-4: Validation results – stage 1 (continued)

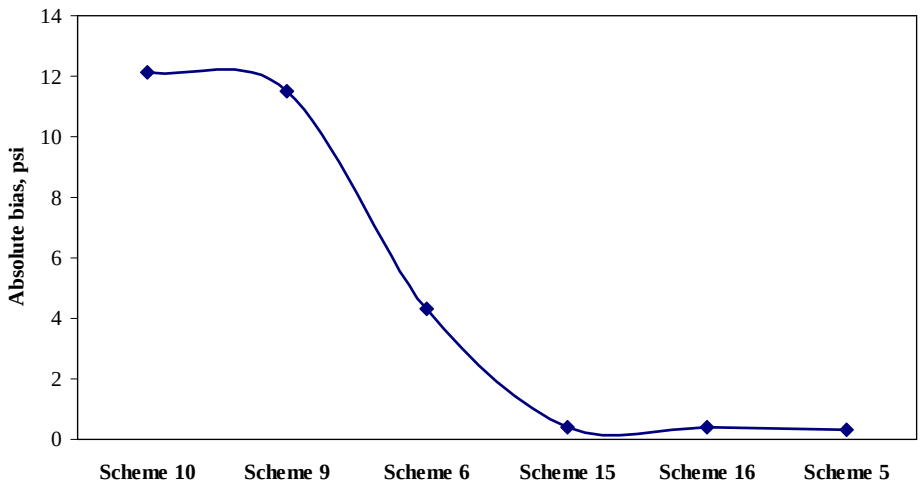

(e) Comparison of absolute value of bias

Figure 5-4: Validation results – stage 1 (continued)

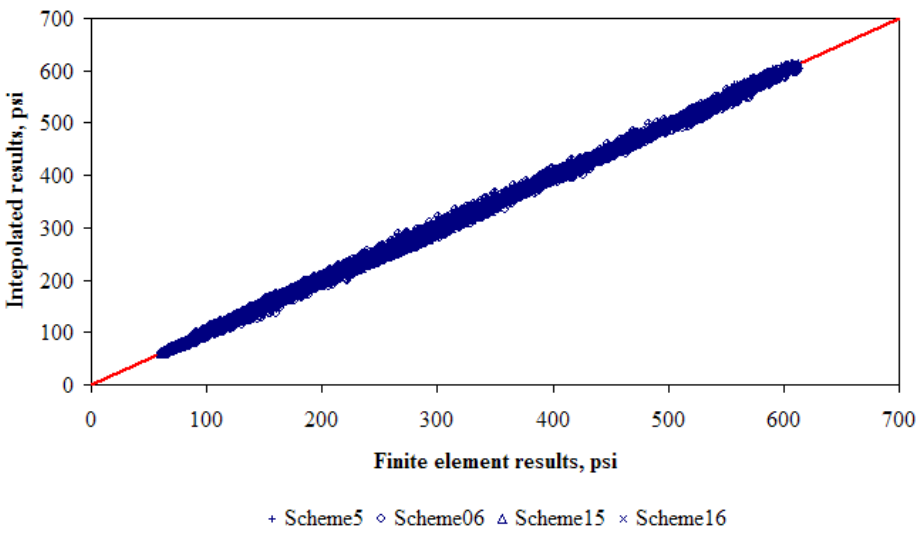

(a) Comparison between FE and interpolated results

Goodness of Fit	Scheme 5	Scheme 6	Scheme 15	Scheme 16
MSE, psi^2	16.47	41.43	4.15	3.11
Variance, psi^2	16.40	28.39	4.14	3.11
Absolute Bias, psi	0.25	3.61	0.11	0.01

(b) Summary of goodness of fit

Figure 5-5: Validation results – stage 2

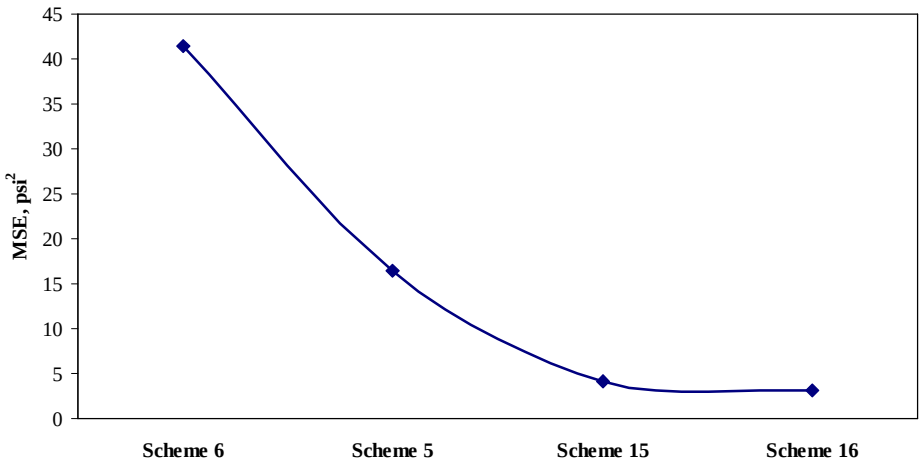

(c) Comparison of MSE

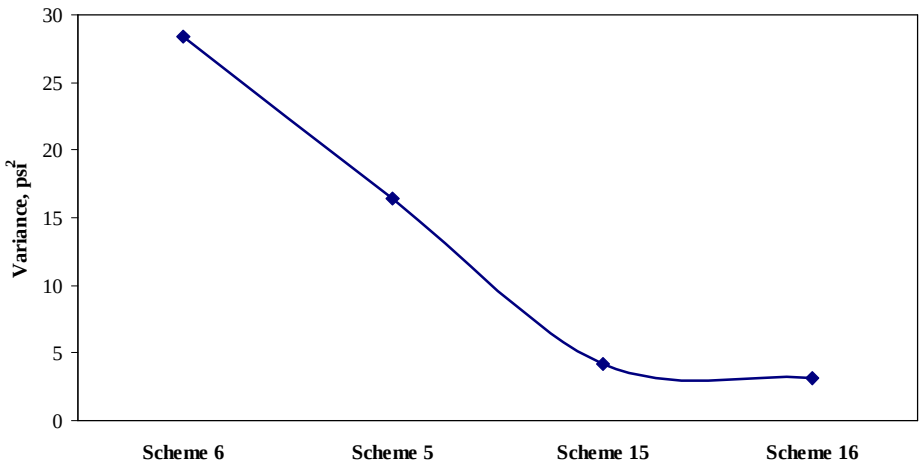

(d) Comparison of variance

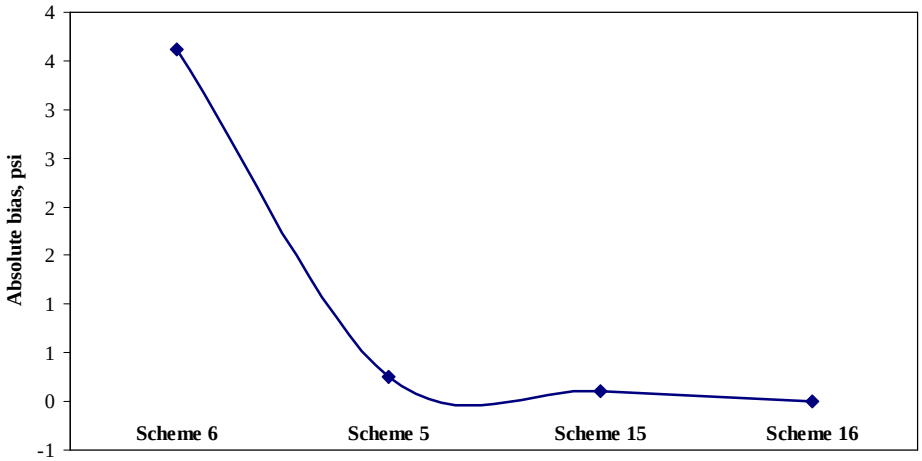

(e) Comparison of absolute value of bias

Figure 5-5: Validation results – stage 2 (continued)

<u>Validation Stage 3</u>: Instead of using the middle points between nodal points in the validation process, this validation stage considers non-nodal points that are randomly selected. This validation stage is based on 300 cases for single through tridem axles and 200 cases for quad through multi-axle (8). The validation results illustrated in Figures 5-6 (a) and (b) and Table 5-2 suggest that scheme 16 is the best performing interpolation scheme. It should be noted that the only difference between schemes 15 and 16 is the prediction matrix in step 2. The values of MSE, bias, and variance obtained from this validation stage were found to be larger than those obtained from the other stages. Since the values for all three non-discrete variables are randomly selected, this validation stage should produce a more realistic result compared to the other stages.

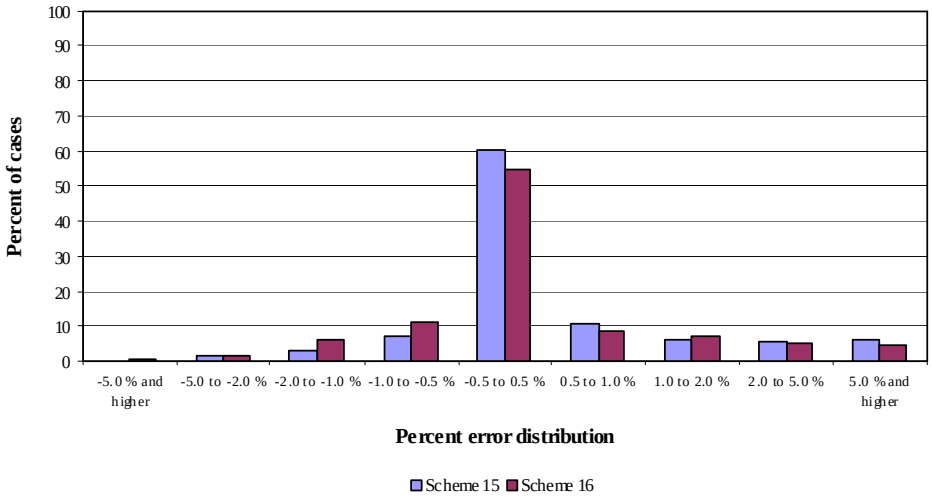

(a) Example error distribution

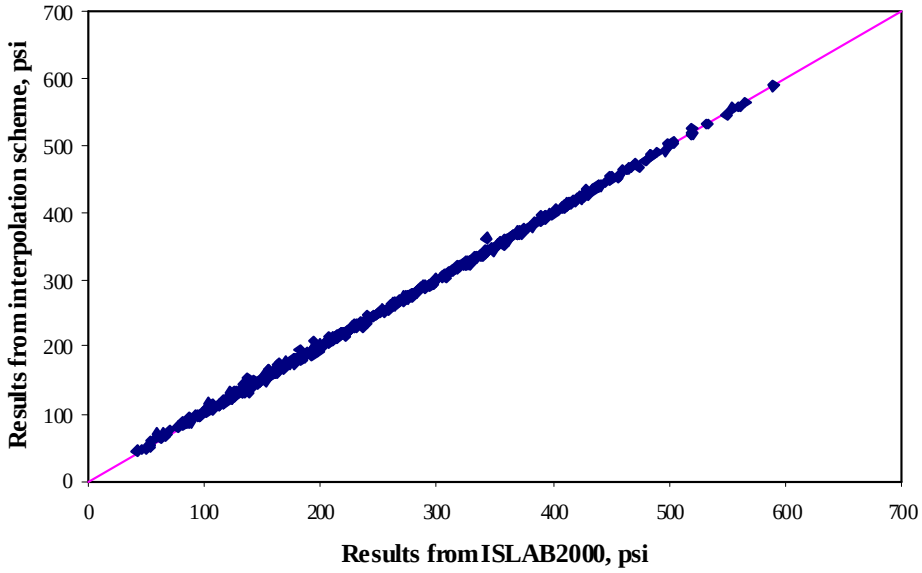

(b) Comparison between actual and interpolated results

Figure 5-6: Validation results – stage 3 (single axle through multi-axle (8))

Table 5-2: Comparison of MSE, bias, and variance

Cases No.	Statistic Results	Longitudinal stress at bottom		Transverse stress at bottom	
		Scheme15	Scheme16	Scheme15	Scheme16
1-500	MSE, psi^2	11.51	8.89	16.40	15.93
	Bias, psi	1.02	0.51	-0.89	-1.21
	Variance, psi^2	10.46	8.63	15.61	14.47
1-300	MSE, psi^2	3.90	3.38	9.70	8.77
	Bias, psi	0.16	0.02	-0.36	-0.59
	Variance, psi^2	3.87	3.38	9.57	8.41
301-500	MSE, psi^2	22.93	17.15	26.46	26.67
	Bias, psi	2.32	1.25	-1.68	-2.13
	Variance, psi^2	17.53	15.60	23.63	22.14

MSE, which is given by the average of the squared errors (differences between actual and interpolated values), is an overall measure of goodness of fit. MSE represents the overall measure of goodness of fit, estimated by the average of square of errors (difference between actual and interpolated values). The MSE can be decomposed into two parts: square of bias and variance. Bias is the average value of errors, while variance is the average of squared deviation of errors from average error. Based on the results from validation stage 3, scheme 16 was found to be most promising. Figures 5-6 (a) and (b) provide for a comparison between actual and interpolated values based on these schemes. These figures suggest that the interpolation schemes can be a reliable alternative for approximating mechanistic responses. Table 5-2 also shows that the interpolated results for single through tridem axles are exceptionally accurate and precise. The biases and variances associated with the longitudinal stress at the bottom of the PCC slab for scheme 16 are 0.0 psi and 3.38 psi^2, respectively. Overall maximum absolute biases based on this scheme are 0.6 psi and 2.1 psi for single through tridem axles and quad through multi-axle (8), respectively.

As the validation process has been completed, the interpolation scheme is used to generate a catalog of stresses by assigning a series of sets of design inputs that are not addressed in the experimental matrix into the interpolation scheme. The catalog of stresses can be found in Appendix I.

5.4 Example Use of Interpolation Scheme

Interpolation schemes can simply be implemented by carrying out the mathematical expressions as described earlier. For example, the longitudinal stress is estimated at the bottom of the PCC slab. The pavement cross-section includes a 275-mm (11-in.) PCC slab, 500-mm (20-in.) base/subbase thickness, 40.7-kPa/mm (150-psi/in.) k-value, 8.0-m (27-ft) joint spacing, tied PCC shoulder, thermal strain gradient of $6x10^{-7}$ mm^{-1} ($15x10^{-6}$ $in.^{-1}$), 142-kN (32-kips) tandem axle.

Step 1: Interpolation in 2-D space across the ranges of base/subbase thickness and k-value

Prediction vector was computed based on H* and k* at the target point (equation 5-8)

$$\overline{X}^* = \left\{ 1 \quad 500 \quad 500^2 \quad \ln(40.7) \quad 500 \cdot \ln(40.7) \quad 500^2 \cdot \ln(40.7) \quad \frac{1}{40.7} \quad \frac{500}{40.7} \quad \frac{500^2}{40.7} \right\}$$

A nine by nine matrix was computed based on H_i and k_j at nodal points (equation 5-10)

$$X = \begin{bmatrix} \overline{X}(100,8.13) \\ \overline{X}(100,27.1) \\ \overline{X}(100,54.2) \\ \overline{X}(400,8.13) \\ \overline{X}(400,27.1) \\ \overline{X}(400,54.2) \\ \overline{X}(650,8.13) \\ \overline{X}(650,27.1) \\ \overline{X}(650,54.2) \end{bmatrix} = \begin{bmatrix} 1 & 100 & 10000 & 2.10 & 210 & 20956 & 0.1230 & 12.30 & 1230 \\ 1 & 100 & 10000 & 3.30 & 330 & 32995 & 0.0369 & 3.69 & 369 \\ 1 & 100 & 10000 & 3.99 & 399 & 39927 & 0.0185 & 1.85 & 185 \\ 1 & 400 & 160000 & 2.10 & 838 & 335290 & 0.1230 & 49.20 & 19680 \\ 1 & 400 & 160000 & 3.30 & 1320 & 527925 & 0.0369 & 14.76 & 5904 \\ 1 & 400 & 160000 & 3.99 & 1597 & 638829 & 0.0185 & 7.38 & 2952 \\ 1 & 650 & 422500 & 2.10 & 1362 & 885374 & 0.1230 & 79.95 & 51968 \\ 1 & 650 & 422500 & 3.30 & 2145 & 1394053 & 0.0369 & 23.99 & 15590 \\ 1 & 650 & 422500 & 3.99 & 2595 & 1686908 & 0.0185 & 11.99 & 7795 \end{bmatrix}$$

Anchor stresses were obtained from FE analysis at H_i and k_j for α=0, 4 and 8x10^{-7} mm^{-1} (equation 5-11)

$$\hat{\sigma}_{\alpha=0} = \begin{Bmatrix} 1092.6 \\ 752.2 \\ 619.3 \\ 1074.0 \\ 738.9 \\ 608.0 \\ 1017.1 \\ 698.3 \\ 573.7 \end{Bmatrix} kPa \qquad \hat{\sigma}_{\alpha=4} = \begin{Bmatrix} 2192.8 \\ 2312.6 \\ 2320.8 \\ 2182.2 \\ 2298.5 \\ 2305.9 \\ 2150.9 \\ 2255.9 \\ 2266.8 \end{Bmatrix} kPa \qquad \hat{\sigma}_{\alpha=8} = \begin{Bmatrix} 3293.1 \\ 3857.2 \\ 3989.4 \\ 3290.4 \\ 3857.1 \\ 4035.2 \\ 3284.7 \\ 3813.5 \\ 3969.3 \end{Bmatrix} kPa$$

Then, stresses at target H* and k* corresponding to the three levels of α were computed (equations 5-7 and 5-9)

$$\sigma(500,40.7,0) = \overline{X}^* \cdot \left[\left[X^T \cdot X \right]^{-1} \cdot X^T \cdot \hat{\sigma}_{\alpha=0} \right] = 647.5 \quad kPa$$

$$\sigma(500,40.7,4) = \overline{X}^* \cdot \left[\left[X^T \cdot X \right]^{-1} \cdot X^T \cdot \hat{\sigma}_{\alpha=4} \right] = 2292.5 \quad kPa$$

$$\sigma(500,40.7,8) = \overline{X}^* \cdot \left[\left[X^T \cdot X \right]^{-1} \cdot X^T \cdot \hat{\sigma}_{\alpha=8} \right] = 3954.2 \quad kPa$$

Step 2: Interpolation in 1-D across the range of thermal strain gradient

Prediction vector was computed based on α* at the target point (equation 5-13)

$$\overline{\alpha}^* = \left\{ 1 \quad 6 \quad 6^2 \right\}$$

A least-squares coefficient vector was computed based on α_i at nodal points and computed stresses obtained from step 1 (equation 5-14)

$$\hat{\gamma} = \begin{bmatrix} 1 & 0 & 0 \\ 1 & 4 & 16 \\ 1 & 8 & 64 \end{bmatrix}^{-1} \cdot \begin{Bmatrix} 647.5 \\ 2292.5 \\ 3954.2 \end{Bmatrix} = \begin{Bmatrix} 647.5 \\ 409.1 \\ 0.526 \end{Bmatrix}$$

Then, the target stress at H*, k* and α* was computed (equation 5-12)

$$\sigma(H^*, k^*, \alpha^*) = \{1 \quad 6 \quad 36\} \cdot \begin{Bmatrix} 647.5 \\ 409.1 \\ 0.526 \end{Bmatrix} = 3121.2 \quad kPa$$

The stress computed using interpolation scheme is 3121.2 kPa (452.353 psi), while the result directly obtained from FE analysis is 3121.8 kPa (452.436 psi). The error of interpolated result in this example is 0.6 kPa (0.1 psi) or 0.02%.

Chapter VI

POTENTIAL IMPLEMENTATION OF STUDY RESULTS

The mechanistic responses obtained from the parametric study not only provide an opportunity to study the interaction between structural, environmental and loading factors on the mechanistic responses as discussed in previous chapters but also can be directly applied to mechanistic-empirical design process of JCP. This chapter reviews the mechanistic-empirical design procedure for JCP and also illustrates how mechanistic responses are used in the process.

6.1 Mechanistic-Empirical Design Concept

The concept of mechanistic-empirical design process is to relate mechanistic responses to certain pavement performance that are considered in design. For each type of performance (e.g. fatigue cracking), the design process is based on damage calculated using mechanistic responses (e.g. longitudinal stresses at bottom of the slab) and accumulated over the entire analysis period as a function of pavement structural features, material properties, axle weights, axle configurations, and thermal gradients that the pavement actually experience. The damage calculation is done using the Miner's hypothesis as shown in (6-1):

$$Damage = \sum_i \sum_j \sum_k \sum_l \sum_m \sum_n \frac{n_{ijklmn}}{N_{ijklmn}}, \qquad (6\text{-}1)$$

where: n_{ijklmn} = Applied number of load repetitions at condition i, j, k, l, m, n
N_{ijklmn} = Allowable number of load repetitions at condition i, j, k, l, m, n
i = Age (year)
j = Season (winter, spring, summer, and fall)
k = Axle configuration (single axle, tandem axle, tridem axle, and etc.)
l = Load level (kips)
m = Thermal gradient (^{o}F/in.)
n = Traffic path

With the application of interpolation scheme as discussed in the previous chapter, mechanistic responses can be computed based on the information for each load repetition at the condition i, j, k, l, m, n. The damage calculation also requires additional data from three sources: material models, hourly axle spectra from WIM (Weigh-in-Motion) database, and hourly thermal gradient generated using EICM (Enhanced Integrated Climatic Model). The computed mechanistic responses, then, are used to calculate the allowable number of load repetitions, N_{ijklmn}. Figure 6-1 illustrates a schematic overview of the damage calculation as a part of the mechanistic-empirical design process.

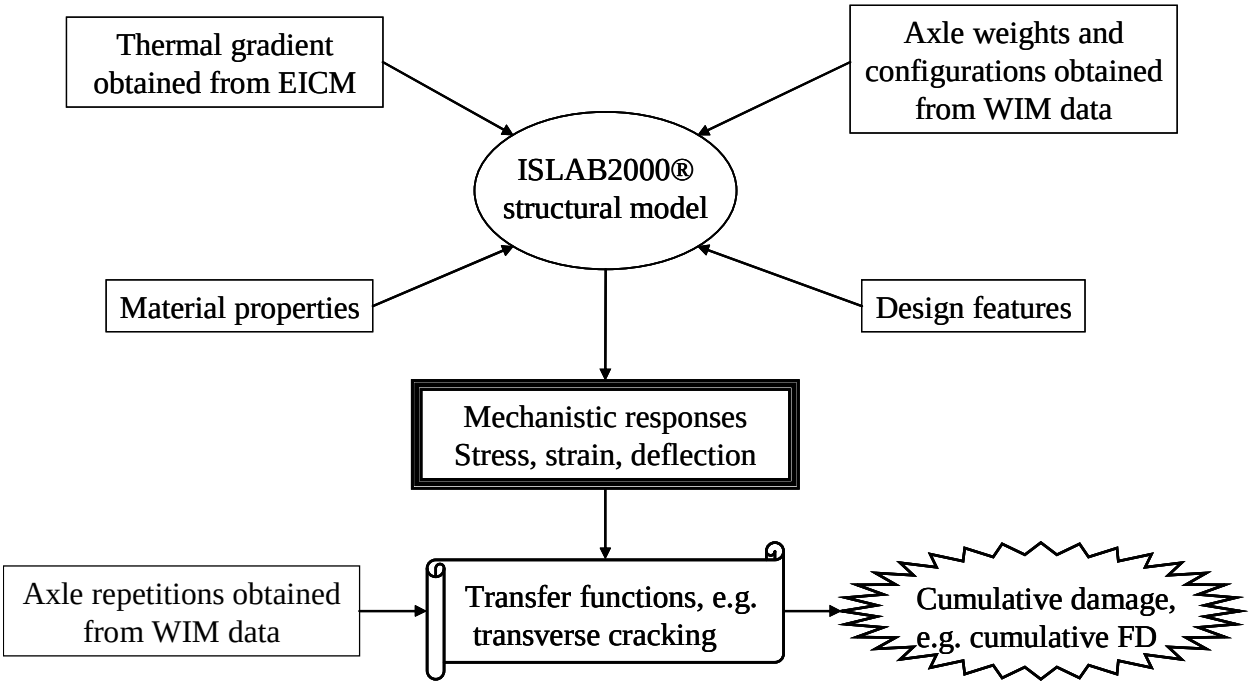

Figure 6-1: Schematic illustration of damage calculation process

The allowable repetitions, N_{ijklmn}, can be obtained by computing mechanistic response at the condition i, j, k, l, m and n and inputting the computed response into performance transfer functions. For fatigue cracking, the input to the transfer function is the ratio of tensile stress to 28-day modulus of rupture, R. Several researchers have suggested equations for fatigue transfer function of plain concrete as follows:

1) Vesic and Sexana (1970): $N = 225{,}000 \times R^{-4}$ (6-2)

2) Portland Cement Association (1975): $Log_{10} N = 11.78 - 12.11 \times R$ (6-3)

3) Zero-Maintenance Project (1977): $Log_{10} N = 17.61 - 17.61 \times R$ (6-4)

4) Khazanovich and Yu (2001): $Log_{10} N = 2.13 \cdot R^{-1.2}$ (6-5)

5) NCHRP 1-37 A (2004): $Log_{10} N = 2 \cdot R^{-1.22} + 0.4371$ (6-6)

Figures 6-2 and 6-3 show the comparison of allowable repetitions and fatigue damage calculated based on these transfer functions at varying values of the R-ratio. It appears that the allowable repetitions and fatigue damage calculated based on the fatigue transfer function suggested in NCHRP 1-37A (Rao et al, 2004) are more conservative than the other models for the range of the R-ratio between 0.60 and 0.85. For the R-ratio greater than 0.85, the results obtained from the Portland Cement Association model are the most conservative.

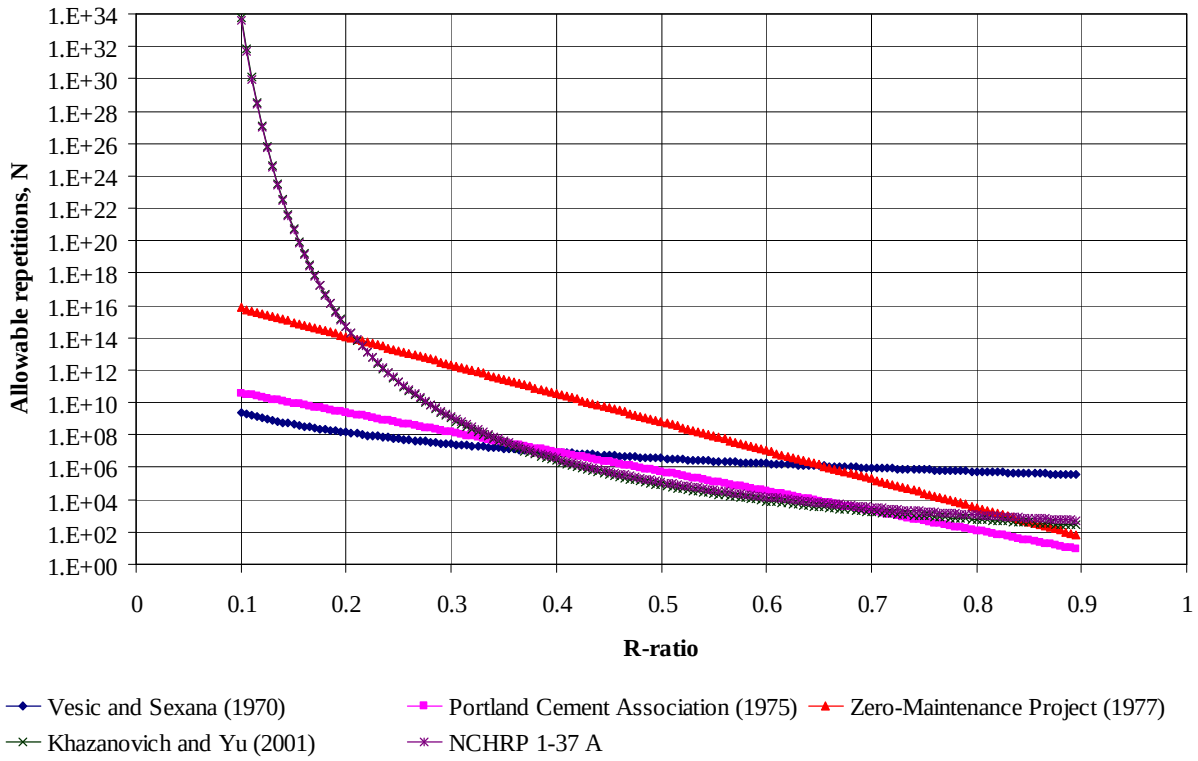

Figure 6-2: Comparison of allowable repetitions based on different fatigue transfer functions

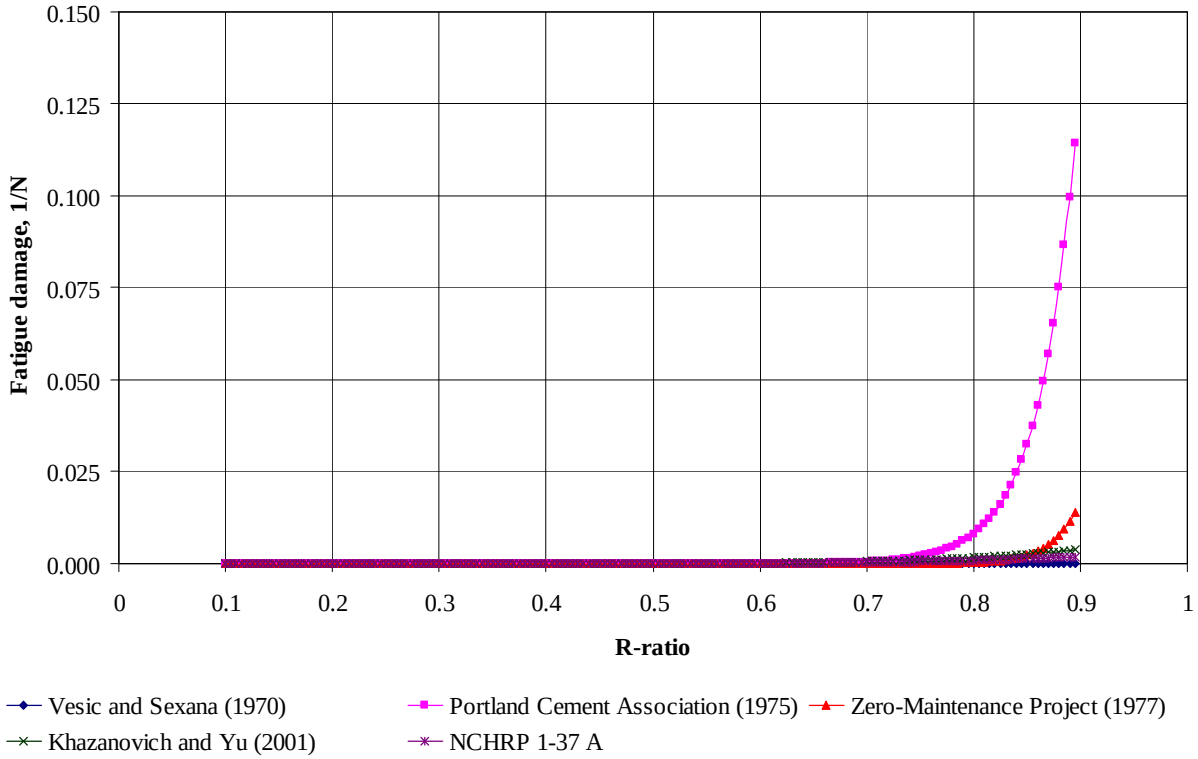

Figure 6-3: Comparison of fatigue damage based on different fatigue transfer functions

6.2 Weigh-in-Motion (WIM) Data Synthesis

As a part of the demonstration of the fatigue damage calculation, WIM data are synthesized for the Michigan SPS-2 sections (US-23 Northbound) from 1998 to 2000. The hourly traffic spectra are generated for each month and each axle type on 3-hour basis. Figures 6-4 and 6-5 are examples of the load spectra. The rest of load spectra are available in Appendix J.

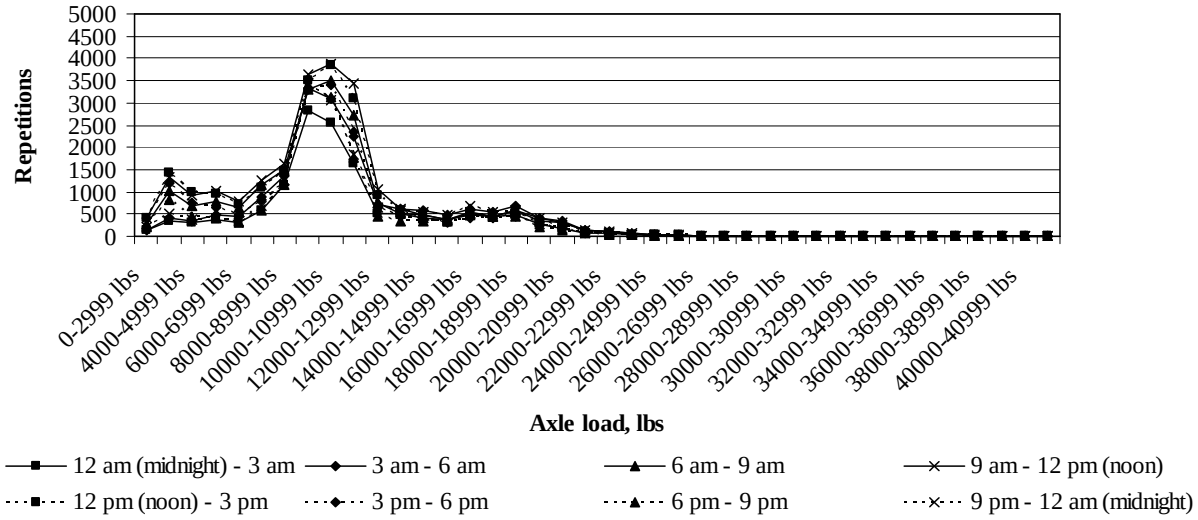

Figure 6-4: Load spectrum from SPS2 sections for single axle in July, 1998

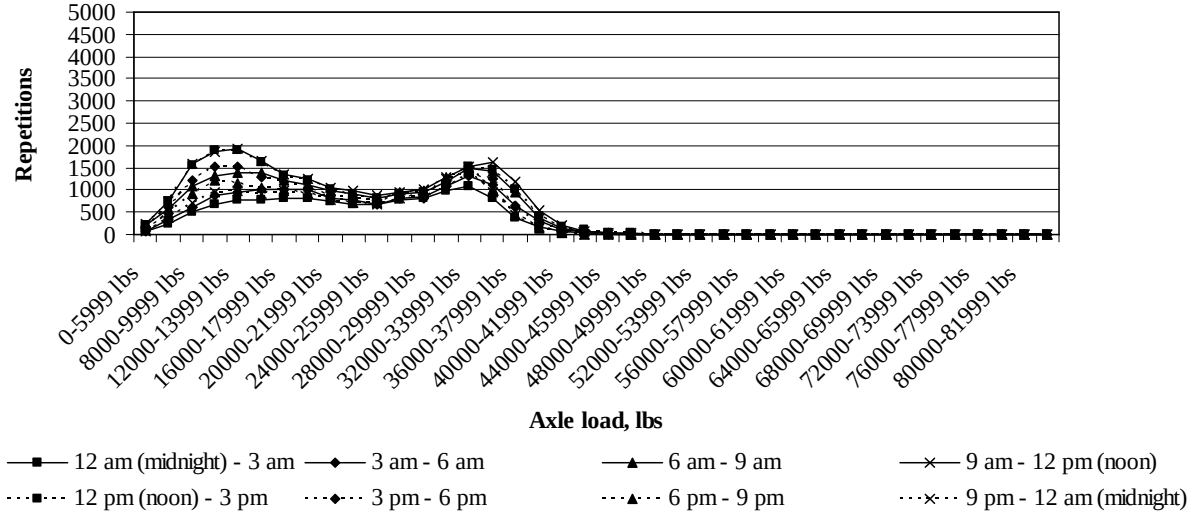

Figure 6-5: Load spectrum from SPS2 sections for tandem axle in July, 1998

The axle repetitions obtained of the WIM database are summarized in Tables 6-1 through 6-8 for each axle configuration. These tables show that the combination of single axle, tandem axle and tridem axle are majority number of repetitions for the SPS-2 sections.

Table 6-1: Summary of single axle load repetitions from SPS-2 section

Load range, lbs	Time interval									
	7/98-9/98	10/98-12/98	1/99-3/99	4/99-6/99	7/99-9/99	10/99-12/99	1/00-3/00	4/00-6/00	7/00-9/00	10/00-12/00
0-4999	73,897	32,139	34,057	66,686	64,857	49,400	34,017	52,423	68,877	58,896
5000-7999	60,122	30,905	34,364	58,049	58,986	52,168	46,874	42,322	58,098	55,975
8000-10999	214,552	127,964	141,516	225,246	208,159	206,808	142,597	153,711	219,733	208,158
11000-13999	99,780	55,168	65,935	106,207	100,406	91,723	69,660	72,201	93,886	94,095
14000-16999	44,970	27,668	30,027	48,737	43,026	38,696	38,084	29,325	38,642	34,699
17000-19999	30,322	16,948	19,744	32,313	31,365	30,560	29,086	23,056	32,010	26,885
20000-22999	9,427	4,683	6,560	9,720	9,756	9,254	6,412	6,144	9,188	7,113
23000-25999	2,018	1,100	1,467	2,264	2,334	1,744	1,106	991	1,471	1,172
26000-28999	594	307	488	561	628	496	276	221	300	275
29000-31999	133	68	149	158	148	116	73	53	60	54
32000-34999	36	20	46	34	29	26	18	12	20	11
35000-37999	5	4	16	9	13	5	4	4	10	3
38000-40999	4	1	4	2	2	3	0	1	0	0
>41000	1	0	4	1	4	0	0	0	0	0

Table 6-2: Summary of tandem axle load repetitions from SPS-2 section

Load range, lbs	Time interval									
	7/98-9/98	10/98-12/98	1/99-3/99	4/99-6/99	7/99-9/99	10/99-12/99	1/00-3/00	4/00-6/00	7/00-9/00	10/00-12/00
0-9999	65,457	55,233	39,411	52,386	54,205	53,444	31,429	24,211	44,844	38,954
10000-15999	113,470	97,841	62,729	100,599	99,644	98,989	79,753	70,261	101,550	102,054
16000-21999	81,779	72,875	50,835	82,935	75,736	74,204	67,743	61,949	81,472	83,218
22000-27999	73,319	64,717	47,237	74,352	64,502	60,455	53,444	49,981	64,713	65,338
28000-33999	98,301	91,484	65,400	105,950	95,230	89,498	77,218	73,024	96,309	91,395
34000-39999	41,867	35,275	27,330	44,421	48,277	48,201	41,889	33,371	49,251	43,921
40000-45999	7,619	4,633	3,391	5,619	6,485	4,388	2,907	2,161	3,776	3,129
46000-51999	695	399	377	505	626	399	287	210	330	339
52000-57999	105	64	83	78	95	62	53	35	55	52
58000-63999	27	22	14	19	18	17	16	8	11	5
64000-69999	6	4	4	8	2	5	2	2	1	1
70000-75999	1	0	1	0	1	0	0	0	0	0
76000-81999	1	0	0	0	0	0	0	0	0	0
>82000	0	0	0	0	0	0	0	0	0	0

Table 6-3: Summary of tridem axle load repetitions from SPS-2 section

Load range, lbs	Time interval									
	7/98-9/98	10/98-12/98	1/99-3/99	4/99-6/99	7/99-9/99	10/99-12/99	1/00-3/00	4/00-6/00	7/00-9/00	10/00-12/00
0-17999	7,305	4,891	1,547	3,049	3,495	4,312	2,237	2,188	2,906	3,486
18000-26999	1,340	727	475	799	798	684	654	610	686	631
27000-35999	1,507	1,394	992	1,438	1,059	1,317	1,074	1,200	1,374	1,596
36000-44999	4,833	5,160	2,889	6,679	5,588	5,483	3,817	5,352	7,466	7,245
45000-53999	4,194	4,160	1,924	3,894	4,224	3,469	1,605	1,735	3,662	2,825
54000-62999	695	587	244	465	487	443	206	251	439	343
63000-71999	84	53	38	57	72	53	28	32	92	47
72000-80999	10	8	5	8	11	12	1	7	10	4
81000-89999	1	2	5	3	4	2	1	1	3	2
90000-98999	3	0	0	0	0	0	0	4	3	0
>99000	0	0	1	0	0	0	0	1	1	0

Table 6-4: Summary of quad axle load repetitions from SPS-2 section

Load range, lbs	Time interval									
	7/98-9/98	10/98-12/98	1/99-3/99	4/99-6/99	7/99-9/99	10/99-12/99	1/00-3/00	4/00-6/00	7/00-9/00	10/00-12/00
0-23999	848	678	379	453	535	767	325	316	493	413
24000-35999	442	323	239	499	448	407	438	382	460	371
36000-47999	631	701	436	761	877	728	477	403	685	703
48000-59999	2,497	2,837	1,454	3,437	3,790	3,071	1,691	2,534	3,692	3,105
60000-71999	1,309	1,160	486	1,020	1,218	1,030	673	916	2,050	1,506
72000-83999	89	62	38	115	82	45	22	66	157	94
84000-95999	3	1	7	6	6	4	2	3	12	11
96000-107999	2	1	1	5	1	7	0	0	1	1
108000-119999	0	4	0	0	1	0	0	0	1	0
120000-131999	0	0	0	0	0	0	0	0	0	0
>132000	0	0	0	0	0	0	0	0	0	0

Table 6-5: Summary of multi-axle (5) load repetitions from SPS-2 section

Load range, lbs	Time interval									
	7/98-9/98	10/98-12/98	1/99-3/99	4/99-6/99	7/99-9/99	10/99-12/99	1/00-3/00	4/00-6/00	7/00-9/00	10/00-12/00
0-29999	634	316	221	306	337	473	237	238	283	273
30000-44999	62	19	45	41	39	71	41	23	40	23
45000-59999	73	79	68	158	99	160	75	97	96	135
60000-74999	686	779	386	1,142	1,207	983	513	710	1,053	1,018
75000-89999	267	199	137	242	409	175	86	123	223	113
90000-104999	17	18	16	14	12	11	5	3	7	8
105000-119999	3	3	4	8	2	1	0	1	2	0
120000-134999	0	0	0	0	0	0	0	0	0	0
135000-149999	0	0	0	0	0	0	0	0	0	0
150000-164999	0	0	0	0	0	0	0	0	0	0
>165000	0	0	0	0	0	0	0	0	0	0

Table 6-6: Summary of multi-axle (6) load repetitions from SPS-2 section

Load range, lbs	Time interval									
	7/98-9/98	10/98-12/98	1/99-3/99	4/99-6/99	7/99-9/99	10/99-12/99	1/00-3/00	4/00-6/00	7/00-9/00	10/00-12/00
0-35999	79	5	2	1	11	23	8	2	7	2
36000-53999	58	10	88	29	15	23	40	19	33	16
54000-71999	139	114	147	163	200	131	79	96	170	103
72000-89999	666	833	450	657	898	660	415	825	1,110	810
90000-107999	345	152	84	135	181	175	51	191	332	107
108000-125999	4	2	0	0	7	13	1	0	1	2
126000-143999	0	0	0	0	0	1	0	0	0	0
144000-161999	0	0	0	0	0	0	0	0	0	0
162000-179999	0	0	0	0	0	0	0	0	0	0
180000-197999	0	0	0	0	0	0	0	0	0	0
>198000	0	0	0	0	0	0	0	0	0	0

Table 6-7: Summary of multi-axle (7) load repetitions from SPS-2 section

Load range, lbs	Time interval									
	7/98-9/98	10/98-12/98	1/99-3/99	4/99-6/99	7/99-9/99	10/99-12/99	1/00-3/00	4/00-6/00	7/00-9/00	10/00-12/00
0-41999	4	6	2	4	4	6	6	1	4	4
42000-62999	23	6	9	21	29	18	23	13	31	21
63000-83999	128	104	62	115	77	81	93	118	197	155
84000-104999	249	100	46	147	211	168	140	139	308	394
105000-125999	25	21	6	5	15	9	6	6	16	20
126000-146999	0	0	0	0	1	0	0	0	1	0
147000-167999	0	0	0	0	0	0	0	0	0	0
168000-188999	0	0	0	0	0	0	0	0	0	0
189000-209999	0	0	0	0	0	0	0	0	0	0
210000-230999	0	0	0	0	0	0	0	0	0	0
>231000	0	0	0	0	0	0	0	0	0	0

Table 6-8: Summary of multi-axle (8) load repetitions from SPS-2 section

Load range, lbs	Time interval									
	7/98-9/98	10/98-12/98	1/99-3/99	4/99-6/99	7/99-9/99	10/99-12/99	1/00-3/00	4/00-6/00	7/00-9/00	10/00-12/00
0-47999	10	4	4	5	10	2	12	4	6	2
48000-71999	35	20	18	53	43	42	42	24	30	39
72000-95999	295	355	195	331	277	330	293	293	416	419
96000-119999	248	251	174	406	337	381	199	331	391	252
120000-143999	8	11	9	8	11	2	3	8	17	6
144000-167999	0	2	0	0	0	0	0	0	0	0
168000-191999	0	0	0	0	0	0	0	0	0	0
192000-215999	0	0	0	0	0	0	0	0	0	0
216000-239999	0	0	0	0	0	0	0	0	0	0
240000-263999	0	0	0	0	0	0	0	0	0	0
>264000	0	0	0	0	0	0	0	0	0	0

6.3 Hourly Thermal Gradients

As a part of fatigue damage calculation, hourly thermal gradients are generated through the use of Enhanced Integrated Climatic Model (EICM). The hourly thermal gradients are obtained for four dense-graded aggregate base (DGAB) SPS-2 sections (26-0213 through 26-0216). The details of these sections are as shown in Table 6.9 below:

Table 6-9: Design features and material properties for the SPS-2 sections

Description	26-0213	26-0214	26-0215	26-0216
PCC thickness, in.	8	8.1	10.7	11.1
Base thickness, in.	6.1	5.8	6.2	5.9
Joint spacing, ft	15	15	15	15
Lateral support condition	Widened lane	AC shoulder	AC shoulder	Widened lane
One-year modulus of rupture*, psi	915	1000	915	1000**
Design 14-day modulus of rupture, psi	550	900	550	900
k-value, psi/in.	See Table 6-10			

Remark: * Obtained from "SPS-2 Construction Report" (Soil and Materials Engineering, Inc., 1995)
** Assumed equal to the modulus of rupture of section 26-0214, since this information is not available in the construction report

Table 6-10: Seasonal backcalculated k-value obtained from LTPP database (FHWA, 2001)

Month	26-0213	26-0214	26-0215	26-0216
January	248	300	254	267
February	203	215	244	221
March	203	215	244	221
April	203	215	244	221
May	158	130	235	174
June	158	130	235	174
July	158	130	235	174
August	203	215	244	221
September	203	215	244	221
October	203	215	244	221
November	248	300	254	267
December	248	300	254	267

Figure 6-6 illustrates an example of hourly thermal gradient distribution obtained from EICM. The rest of hourly thermal gradient distributions are also available in Appendix K.

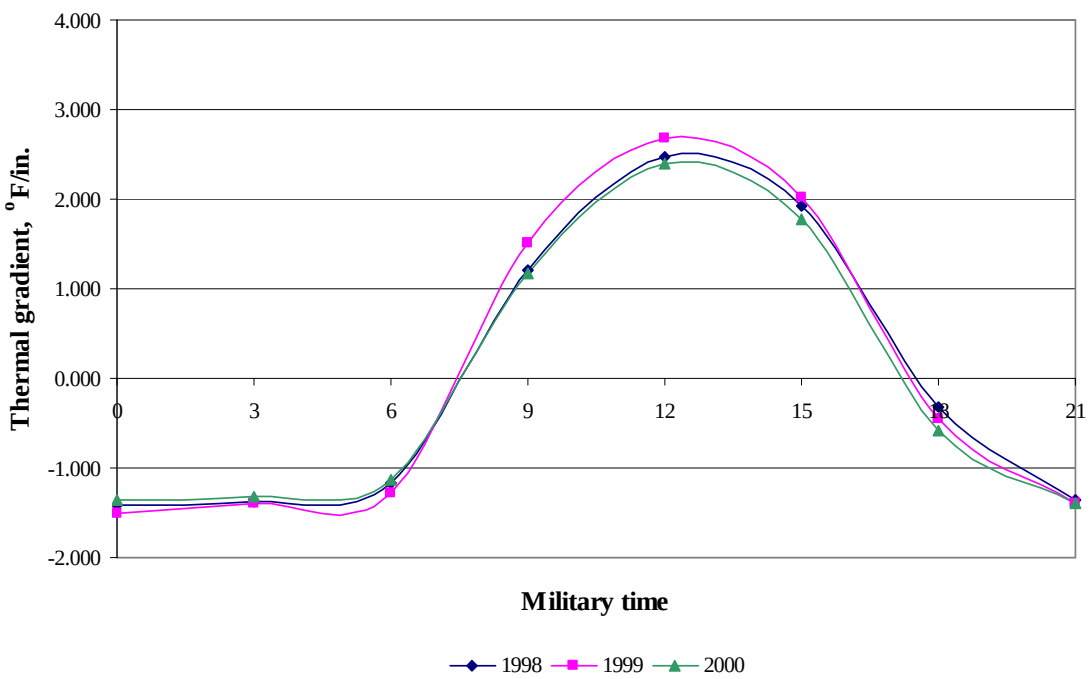

Figure 6-6: Hourly thermal gradients generated by EICM for 8-in. sections in September

6.4 Mechanistic-Empirical Procedure for JCP - Example

Mechanistic-empirical design procedure for JCP relies on relationship between cumulative damage and level of distress. For example, fatigue damage could be calculated using the NCHRP 1-37 A transfer function (Equation 6-6) based on the magnitude of longitudinal stress at the bottom of the slab corresponding to axle type, axle weight, seasonal k-value and hourly thermal gradient for each axle repetition over the analysis period, which could be obtained from the catalog of stresses. This results in the allowable number of load repetitions at a specified condition, N, in the Miner's hypothesis (Equation 6-1). Along with the number of axle repetitions, n, which could be obtained through the WIM database or any available traffic database, cumulative damage could be calculated. The schematic of the process is shown in Figure 6-7.

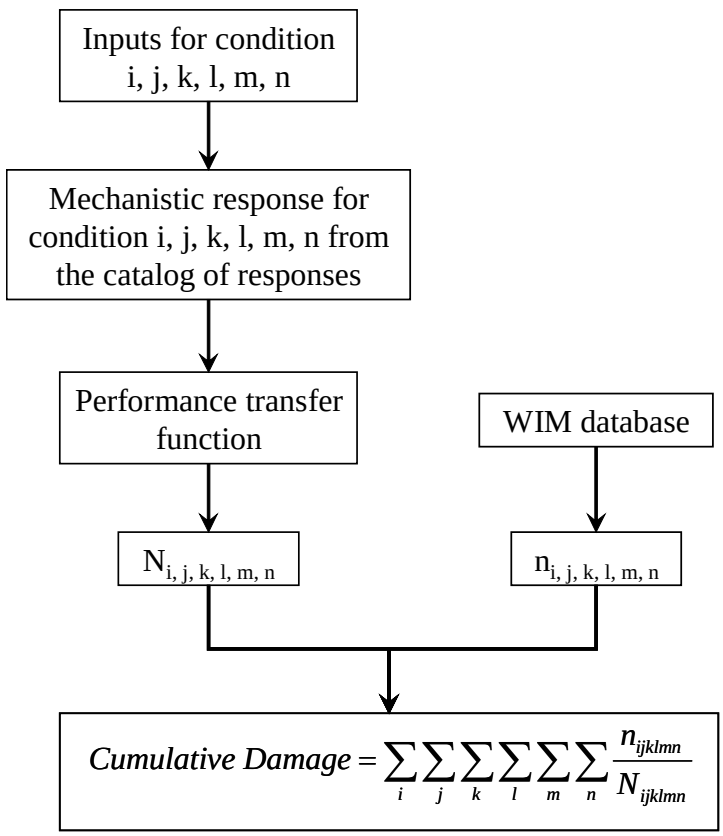

Figure 6-7: Cumulative damage calculation process

The next step is to plot the computed cumulative damage against distress (e.g. cracking). It is widely believed that a cumulative damage of 1.0 relates to a failed pavement. On a plot of cumulative damage versus distress, the cumulative damage of 1.0 may not match with the cracking threshold established by the agency; hence the performance curve needs to be calibrated. The calibration process is illustrated in Figure 6-8. For example, Figures 6-9 and 6-10 illustrate an example characteristic fatigue curve before and after calibration process for 50% slabs cracked considered as the rehabilitation distress level.

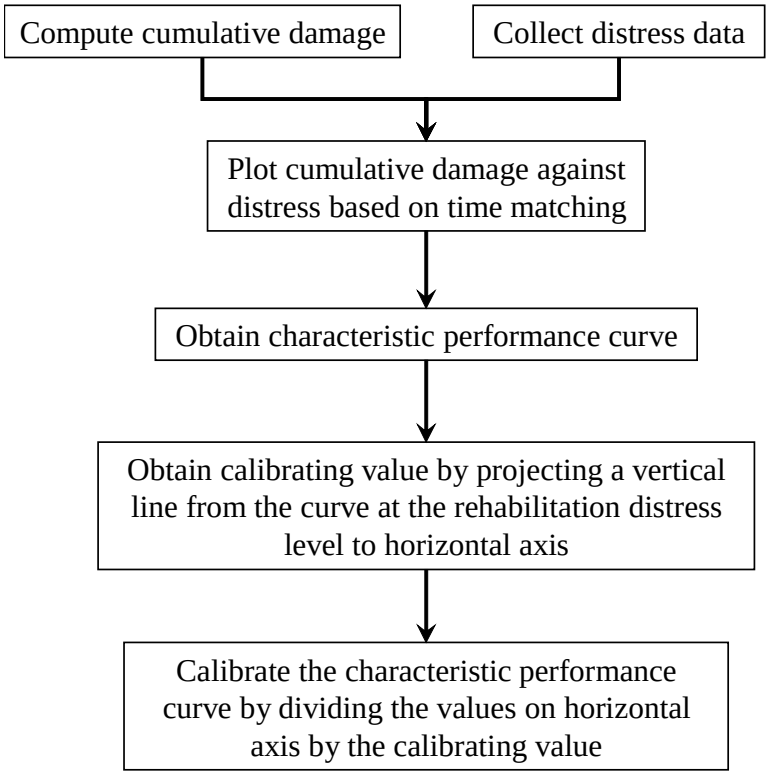

Figure 6-8: Calibration process for the relationship between cumulative damage and distress

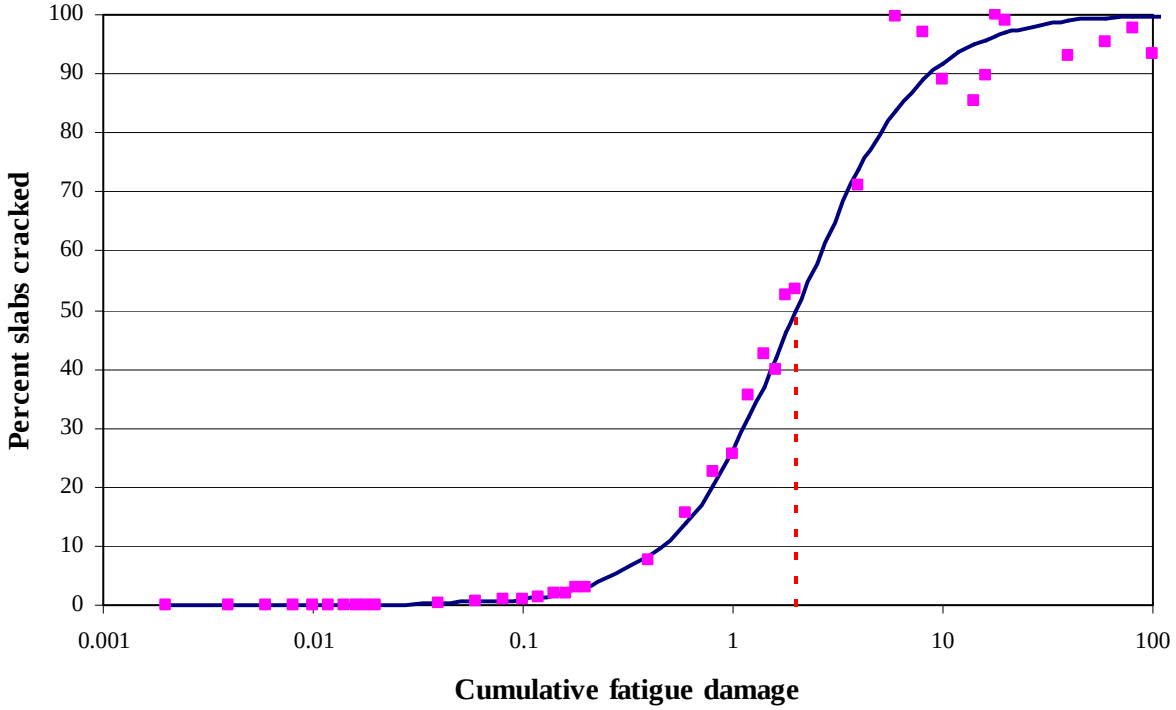

Figure 6-9: Example characteristic fatigue curve before calibration process

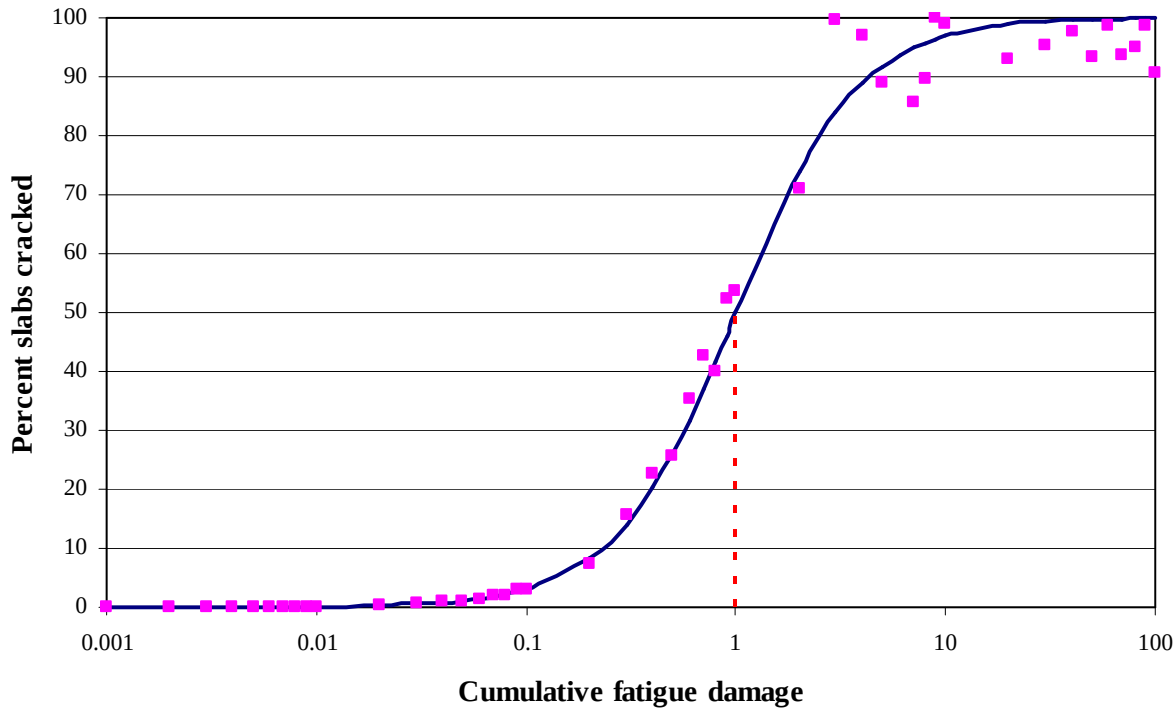

Figure 6-10: Example characteristic fatigue curve after calibration process

The design process for faulting and spalling are also based on cumulative damage concept. However, the relationship between cumulative damage and these distresses is expressed in different forms from cracking. Based on NCHRP 1-37 A (Khazanovich et al, 2004), the design process for faulting and spalling could be summarized as follows:

Design of Faulting

$$Fault_m = \sum_{i=1}^{m} \Delta Fault_i \tag{6-7}$$

$$\Delta Fault_i = C_{34} \times \left(FAULTMAX_{i-1} - Fault_{i-1}\right)^2 \times DE_i \tag{6-8}$$

$$FAULTMAX_i = FAULTMAX_0 + C_7 \times \sum_{j=1}^{m} DE_j \times \log\left(1 + C_5 \times 5.0^{EROD}\right)^{C_6} \tag{6-9}$$

$$FAULTMAX_0 = C_{12} \times \delta_{curling} \times \left[\log\left(1 + C_5 \times 5.0^{EROD}\right) \times \log\left(\frac{P_{200} \times WetDays}{P_s}\right)\right]^{C_6} \tag{6-10}$$

Where:
$Fault_m$ = mean joint faulting at the end of month m, in.
$\Delta Fault_i$ = incremental change (monthly) in mean transverse joint faulting during month i, in.
$FAULTMAX_i$ = maximum mean transverse joint faulting for month i, in.
$FAULTMAX_0$ = initial maximum mean transverse joint faulting, in.
EROD = base/subbase erodibility factor

DE = differential elastic deformation energy

$$DE = \frac{1}{2} \cdot k \cdot (W_L + W_{UL}) \cdot (W_L - W_{UL})$$

k = modulus of subgrade reaction, kPa/mm
W_L = deflection of loaded slab, mm
W_{UL} = deflection of unloaded slab, mm
$\delta_{curling}$ = maximum mean monthly slab corner upward deflection PCC due to temperature curling and moisture warping
P_s = overburden on subgrade, lb.
P_{200} = percent subgrade material passing #200 sieve
WetDays = average annual number of wet days (greater than 0.1 in. rainfall)
C_1 through C_7 and C_{12}, C_{34} are calibration constants:

$C_{12} = C_1 + C_2 * FR^{0.25}$
$C_{34} = C_3 + C_4 * FR^{0.25}$
$C_1 = 1.29$, $C_2 = 1.1$, $C_3 = 0.0001725$, $C_4 = 0.0008$, $C_5 = 250$, $C_6 = 0.4$, $C_7 = 1.2$

FR = base freezing index defined as percentage of time the top base temperature is below freezing (32 ^oF) temperature

Design of Spalling

$$SPALL = \left[\frac{AGE}{AGE + 0.01} \right] \cdot \left[\frac{100}{1 + 1.005^{(-12*AGE+SCF)}} \right] \tag{6-11}$$

Where:
SPALL = percentage joints spalled (medium- and high-severities)
AGE = pavement age since construction, years
SCF = scaling factor based on site-, design-, and climate-related variables

$$SCF = -1400 + 350 \cdot AIR\% \cdot (0.5 + PREFORM) + 3.4 \cdot f'_c \cdot 0.4$$
$$- 0.2(FTCYC \cdot AGE) + 43 \cdot h_{PCC} - 536 \cdot WC_Ratio$$

AIR% = PCC air content, percent
PREFORM = 1 if preformed sealant is present; 0 if not
f'_c = PCC compressive strength, psi
FTCYC = average annual number of freeze-thaw cycles
h_{PCC} = PCC slab thickness, in.
WC_Ratio = PCC water/cement ratio

Seven illustrative examples to demonstrate the calculation process for fatigue damage, faulting damage and spalling damage are presented. Relevant inputs and details, including calculation results for these examples are summarized in Table 6-11.

Table 6-11: Summary of illustrative examples

Example	Type of Damage			Inputs	Results	Remarks
	Fatigue	Faulting	Spalling			
1	X			10-in. slab thickness, 16-in. aggregate base, 100-psi/in. roadbed, 177-in. joint spacing, 12-ft lane with tied PCC shoulder, positive thermal gradient of 2 ^{o}F/in., i) 18-kips single axle, 32-kips tandem axle and 39-kips tridem axle	Allowable number of axle repetitions: 3.81 million for single axle, 0.83 million for tandem axle and 8.24 million for tridem axle	Fatigue damage due to different axle configurations
2	X			Same as Example 1 but with i) 12-ft lane with untied AC shoulder and ii) 14-ft lane with untied AC shoulder and only under 39-kips tridem axle	Allowable number of axle repetitions: 0.87 million for 12 ft lane with untied AC shoulder and 3.07 million for 14-ft lane with untied AC shoulder	Fatigue damage due to different lateral support conditions
3	X			Same as Example 1 but with 8, 9, 11 and 12-in. slab thickness and only under 32-kips tandem axle	Allowable number of axle repetitions: 0.056 million for 8 in. slab, 0.193 million for 9-in. slab, 4.60 million for 11-in. slab and 32.53 million for 12-in. slab	Fatigue damage due to different slab thickness
4		X		Same as Example 1 but consider typical traffic spectra and climatic conditions in Michigan	Predicted faulting at the end of 20-years period: 0.1671 in.	Transverse joint faulting damage calculation
5		X		Same as Example 4 but with i) 1.5-in. dowel dia. at 12 in. spacing, ii) 1.25-in. dowel dia. at 18 in. spacing, iii) 1.5-in. dowel dia. at 18 in. spacing	Predicted faulting at the end of 20-years period: 0.0935 in. for 1.5-in. dowel dia. at 12 in. spacing, 0.1682 in. for 1.25-in. dowel dia. at 18 in. spacing, 0.0941 in. for 1.5-in. dowel dia. at 18 in. spacing	Transverse joint faulting damage due to different joint designs
6		X		Same as Example 4 but with lean concrete base (LCB) and asphalt treated base (ATB)	Predicted faulting at the end of 20-years period: 0.1066 in. for LCB and 0.1280 in. for ATB	Transverse joint faulting damage due to different base types
7			X	3% air content, no preformed sealant, 2,000-psi concrete compressive strength, average freeze thaw cycles per year of 250, 8-in. slab and 0.45 water/cement ratio	Predicted percent slabs spalled at the end of 20-years period: 3%	Transverse joint spalling damage

<u>Illustrative Example 1</u> (fatigue damage due to different axle configurations)

Analyze the number of load repetitions of 18-kips single axle, 32-kips tandem axle, and 39-kips tridem axle that could be carried at daytime thermal gradient of 2 ^{o}F/in. by a pavement system with the following features:

- 10-in. slab thickness,
- 16-in. aggregate base,
- 100-psi/in. roadbed soil,

- 177-in. joint spacing,
- 12-ft lane,
- tied PCC shoulder,
- and 1.25-in. dowel diameter at 12 in. center to center spacing.

Note that the concrete coefficient of thermal expansion and 28-day modulus of rupture were found to be 5 in./in./^{o}F and 550 psi, respectively.

From the catalog of stresses in Appendix I, the magnitudes of the longitudinal stresses at the bottom of the PCC slab are:

For 18-kips single axle:	219.2	psi
For 32-kips tandem axle:	230.3	psi
For 39-kips tridem axle:	198.0	psi

The stress ratios for the three axle configurations are calculated as follows:

For 18-kips single axle: $R_{\text{18-kips single axle}} = \dfrac{219.2}{550} = 0.399$

For 32-kips tandem axle: $R_{\text{32-kips tandem axle}} = \dfrac{230.3}{550} = 0.419$

For 39-kips tridem axle: $R_{\text{39-kips tridem axle}} = \dfrac{198.0}{550} = 0.360$

Considering the performance transfer function in equation (6-6), the number of load repetitions of 18-kips single axle, 32-kips tandem axle and 39-kips tridem axle that could be carried for the given conditions could be analyzed as follows:

Recall that $Log_{10} N = 2 \cdot R^{-1.22} + 0.4371$ or $N = 10^{\left[2 \cdot R^{-1.22} + 0.4371\right]}$

For 18-kips single axle: $N_{\text{18-kips single axle}} = 10^{\left[2 \cdot (0.399)^{-1.22} + 0.4371\right]} = 3.81 \quad \textit{million cycles}$

For 32-kips tandem axle: $N_{\text{32-kips tandem axle}} = 10^{\left[2 \cdot (0.419)^{-1.22} + 0.4371\right]} = 1.67 \quad \textit{million cycles}$

For 39-kips tridem axle: $N_{\text{39-kips tridem axle)}} = 10^{\left[2 \cdot (0.360)^{-1.22} + 0.4371\right]} = 24.71 \quad \textit{million cycles}$

However, the number of repetitions needed to account for the number of repetitions within each axle group. For example, each tandem and tridem axle results in peak stress level two and three times, respectively. The number of repetitions for each axle could be adjusted as follows:

Adjusted number of repetitions, $N_{adjusted} = \dfrac{N}{\text{number of repetitions within each axle}}$

For 18-kips single axle: $N_{\text{18-kips single axle}} = \dfrac{3.81}{1} = 3.81 \quad \textit{million cycles}$

For 32-kips tandem axle: $N_{\text{32-kips tandem axle}} = \frac{1.67}{2} = 0.83 \quad \textit{million cycles}$

For 39-kips tridem axle: $N_{\text{39-kips tridem axle)}} = \frac{24.71}{3} = 8.24 \quad \textit{million cycles}$

Figure 6-11 illustrates the number of allowable repetitions and the weight of each axle. It can be seen that the pavement could carry more repetitions of 39-kips tridem axle, when compared with the others. The more number of wheels in an axle reduce the level of stress and consequently increase the number of allowable repetition.

With the use of WIM database, the actual number of load repetitions, n, could be additionally applied to the allowable number of repetitions, N, to compute the damage, n/N. Then, the summation of the damage over conditions, i, j, k, l, m, and n will provide cumulative damage as described in Figure 6-7. With availability of pavement performance data (percent slabs cracked for this case), the cumulative damage could be plotted against the performance data. After that, calibration process is required to match the cumulative damage of one with the rehabilitation distress level, illustrated in Figure 6-8.

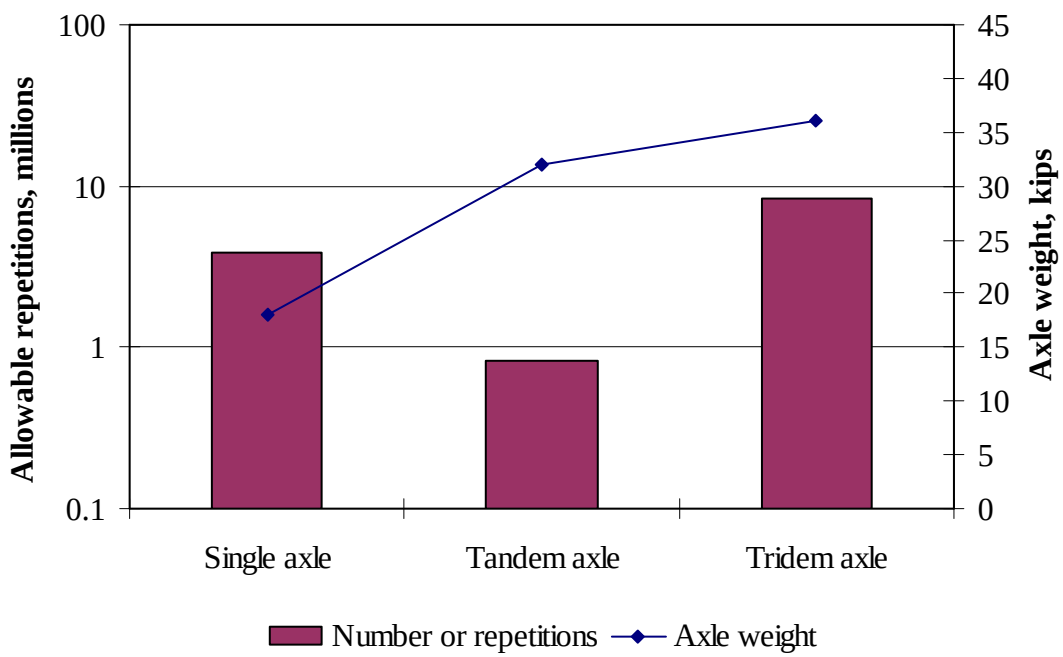

Figure 6-11: Comparison of results for Example 1

<u>Illustrative Example 2</u> (fatigue damage due to different lateral support conditions)

Analyze the number of load repetitions of 39-kips tridem axle that could be carried at daytime thermal gradient of 2 ^{o}F/in. by pavement systems in Example 1 but with 12-ft lane with untied AC shoulder and 14-ft lane with untied AC shoulder.

From the catalog of stresses in Appendix I, the magnitudes of the longitudinal stresses at the bottom of the PCC slab are:

For 12-ft lane with untied AC shoulder: 224.1 psi
For 14-ft lane with untied AC shoulder: 208.6 psi

The stress ratios for the two lateral support conditions are calculated as follows:

For 12-ft lane with untied AC shoulder: $R_{\text{12-ft lane with united AC shoulder}} = \dfrac{224.1}{550} = 0.407$

For 14-ft lane with untied AC shoulder: $R_{\text{14-ft lane with untied AC shoulder}} = \dfrac{208.6}{550} = 0.379$

Considering the performance transfer function in equation (6-6), the number of load repetitions of 39-kips tridem axle that could be carried for the given conditions could be analyzed as follows:

Recall that $Log_{10} N = 2 \cdot R^{-1.22} + 0.4371$ or $N = 10^{\left[2 \cdot R^{-1.22} + 0.4371\right]}$

For 12-ft lane with untied AC shoulder:

$N_{\text{12-ft lane with united AC shoulder}} = 10^{\left[2 \cdot (0.407)^{-1.22} + 0.4371\right]} = 2.62 \quad \textit{million cycles}$

For 14-ft lane with untied AC shoulder:

$N_{\text{14-ft lane with united AC shoulder}} = 10^{\left[2 \cdot (0.379)^{-1.22} + 0.4371\right]} = 9.21 \quad \textit{million cycles}$

However, the number of repetitions needed to account for the number of repetitions within each axle group. The number of repetitions for each axle could be adjusted as follows:

Adjusted number of repetitions, $N_{adjusted} = \dfrac{N}{\text{number of repetitions within each axle}}$

For 12-ft lane with untied AC shoulder:

$N_{\text{12-ft lane with united AC shoulder}} = \dfrac{2.62}{3} = 0.87 \quad \textit{million cycles}$

For 14-ft lane with untied AC shoulder:

$N_{\text{14-ft lane with united AC shoulder}} = \dfrac{9.21}{3} = 3.07 \quad \textit{million cycles}$

Figure 6-12 illustrates the number of allowable repetitions for each lateral support condition, including the 12-ft lane with tied PCC shoulder from Example 1. It can be seen that the pavement with 12-ft lane with tied PCC shoulder could carry more repetitions of 39-kips tridem axle, when compared with the others. For the untied AC shoulder pavements, the 14-ft lane pavement could carry more load repetitions than the 12-ft pavement. The two-foot shifting of the wheel path away from the edge creates the pseudo-interior loading condition for the 14-ft lane pavement and consequently reduces the level of stress.

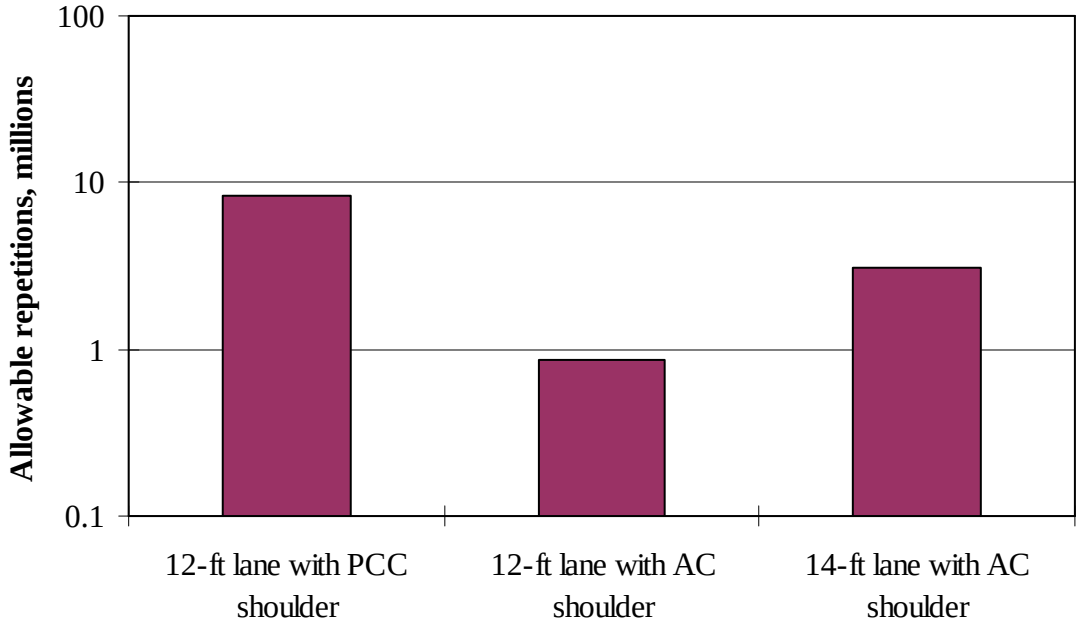

Figure 6-12: Comparison of results for Example 2

<u>Illustrative Example 3</u> (fatigue damage due to different slab thickness)

Analyze the number of load repetitions of 32-kips tandem axle that could be carried at daytime thermal gradient of 2 ^{o}F/in. by pavement systems in Example 1 but with 8, 9, 11, and 12-in. PCC slab.

From the catalog of stresses in Appendix I, the magnitudes of the longitudinal stresses at the bottom of the PCC slab are:

For 8-in. slab: 277.2 psi
For 9-in. slab: 253.3 psi
For 11-in. slab: 208.6 psi
For 12-in. slab: 188.7 psi

The stress ratios for the four slab thicknesses are calculated as follows:

For 8-in. slab: $R_{8\text{-in.}} = \dfrac{277.2}{550} = 0.504$

For 9-in. slab: $R_{9\text{-in.}} = \dfrac{253.3}{550} = 0.461$

For 11-in. slab: $R_{11\text{-in.}} = \dfrac{208.6}{550} = 0.379$

For 12-in. slab: $R_{12\text{-in.}} = \dfrac{188.7}{550} = 0.343$

Considering the performance transfer function in equation (6-6), the number of load repetitions of 39-kips tridem axle that could be carried for the given conditions could be analyzed as follows:

Recall that $Log_{10} N = 2 \cdot R^{-1.22} + 0.4371$ or $N = 10^{\left[2 \cdot R^{-1.22} + 0.4371\right]}$

For 8-in. slab: $N_{8\text{-in.}} = 10^{\left[2 \cdot (0.504)^{-1.22} + 0.4371\right]} = 0.112 \quad \textit{million cycles}$

For 9-in. slab: $N_{9\text{-in.}} = 10^{\left[2 \cdot (0.461)^{-1.22} + 0.4371\right]} = 0.387 \quad \textit{million cycles}$

For 11-in. slab: $N_{11\text{-in.}} = 10^{\left[2 \cdot (0.379)^{-1.22} + 0.4371\right]} = 9.21 \quad \textit{million cycles}$

For 12-in. slab: $N_{12\text{-in.}} = 10^{\left[2 \cdot (0.343)^{-1.22} + 0.4371\right]} = 65.05 \quad \textit{million cycles}$

However, the number of repetitions needed to account for the number of repetitions within each axle group. The number of repetitions for each axle could be adjusted as follows:

Adjusted number of repetitions, $N_{adjusted} = \dfrac{N}{\text{number of repetitions within each axle}}$

For 8-in. slab: $N_{8\text{-in.}} = \dfrac{0.112}{2} = 0.056 \quad \textit{million cycles}$

For 9-in. slab: $N_{9\text{-in.}} = \dfrac{0.387}{2} = 0.193 \quad \textit{million cycles}$

For 11-in. slab: $N_{11\text{-in.}} = \dfrac{9.21}{2} = 4.60 \quad \textit{million cycles}$

For 12-in. slab: $N_{12\text{-in.}} = \dfrac{65.05}{2} = 32.53 \quad \textit{million cycles}$

Figure 6-13 illustrates the number of allowable repetitions for each slab thickness, including the 10-in. slab from Example 1. The number of allowable load repetitions is very sensitive to the slab thickness. It can be seen that load carrying capacity of the pavement is logarithmically related to the slab thickness as a linear relationship could be observed on a semi-logarithmic plot.

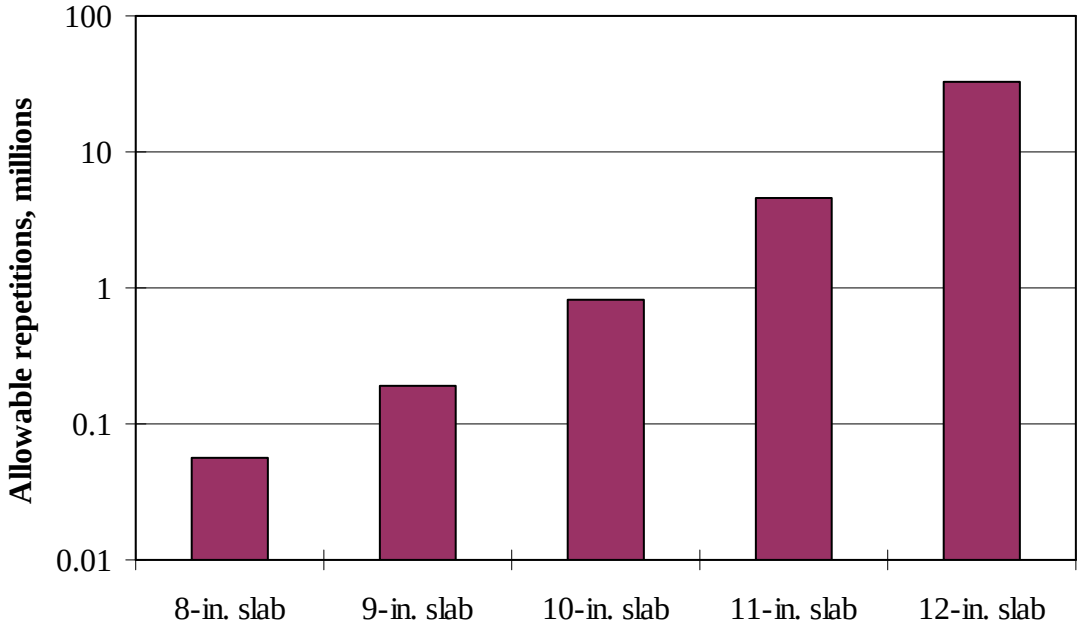

Figure 6-13: Comparison of results for Example 3

<u>Illustrative Example 4</u> (faulting damage)

Analyze the joint faulting of pavement systems in Example 1 at the end of a design period of 20 years.

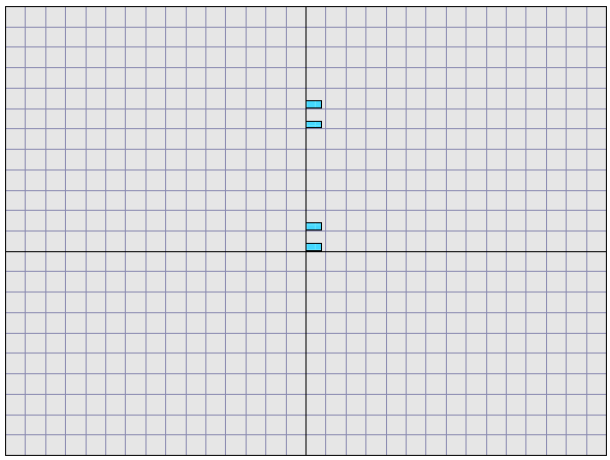

Figure 6-14: Overview of analysis of joint faulting for Example 4

The analysis joint faulting damage involves the calculation of differential elastic deformation energy, which is a function of slab corner deflections obtained from FE analysis with loading at the transverse joint, e.g. 18-kips single axle as shown in Figure 6-14.

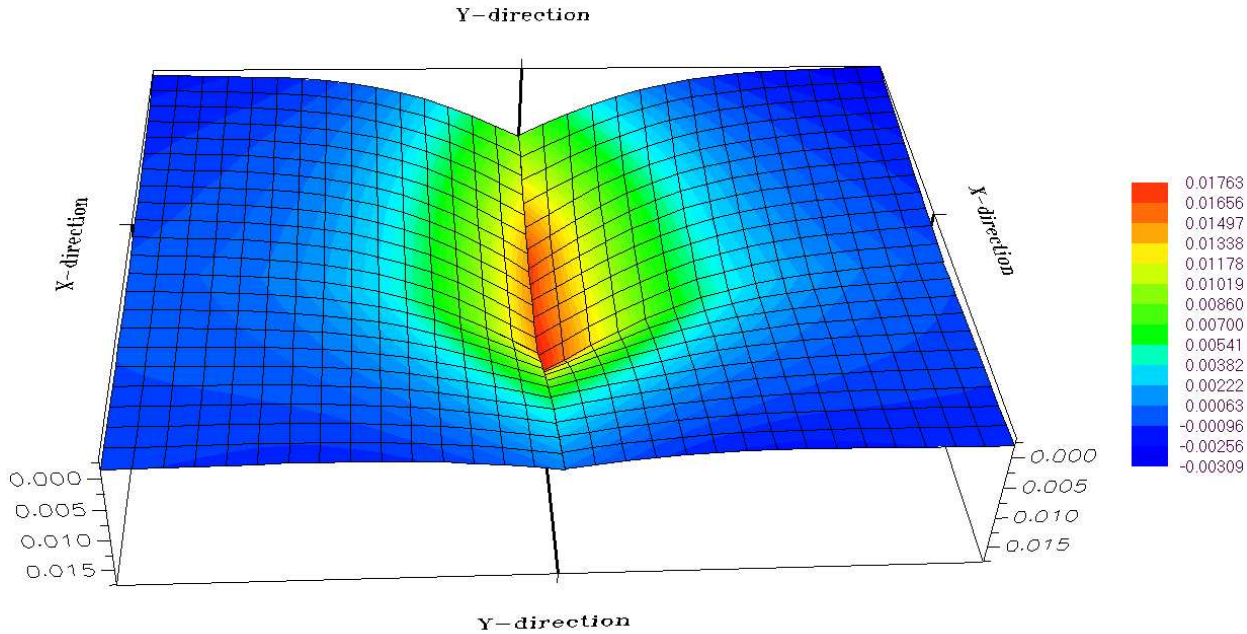

Figure 6-15: Slab deflection results for Example 4

From the results shown in Figure 6-15, the slab deflections on both loaded and unloaded sides at the corners of the slabs could be obtained as follows:

Unloaded deflection, $W_{UL} = 0.013797\ in. = 0.35044\ mm$

Loaded deflection, $W_L = 0.017627\ in. = 0.44773\ mm$

For the given modulus of subgrade reaction (100 psi/in. or 27.145 kPa/mm), the differential elastic deformation energy could be calculated as follows:

Differential elastic deformation energy, $DE = \frac{1}{2} \cdot k \cdot (W_L + W_{UL}) \cdot (W_L - W_{UL})$

$$DE = \frac{1}{2} \cdot (27.145) \cdot (0.44773 + 0.35044) \cdot (0.44773 - 0.35044) = 1.053871\ kPa \cdot mm$$

If a typical load spectrum and a typical climatic condition for Michigan are assumed for this example, the faulting calculation could be conducted using Equations 6-7 through 6-10. It should be noted that an erodibility index of 3 (erosion resistant) is assumed for this example.

The predicted faulting is illustrated in Figure 6-16. The predicted faulting is 0.1671 in. at the end of the design period.

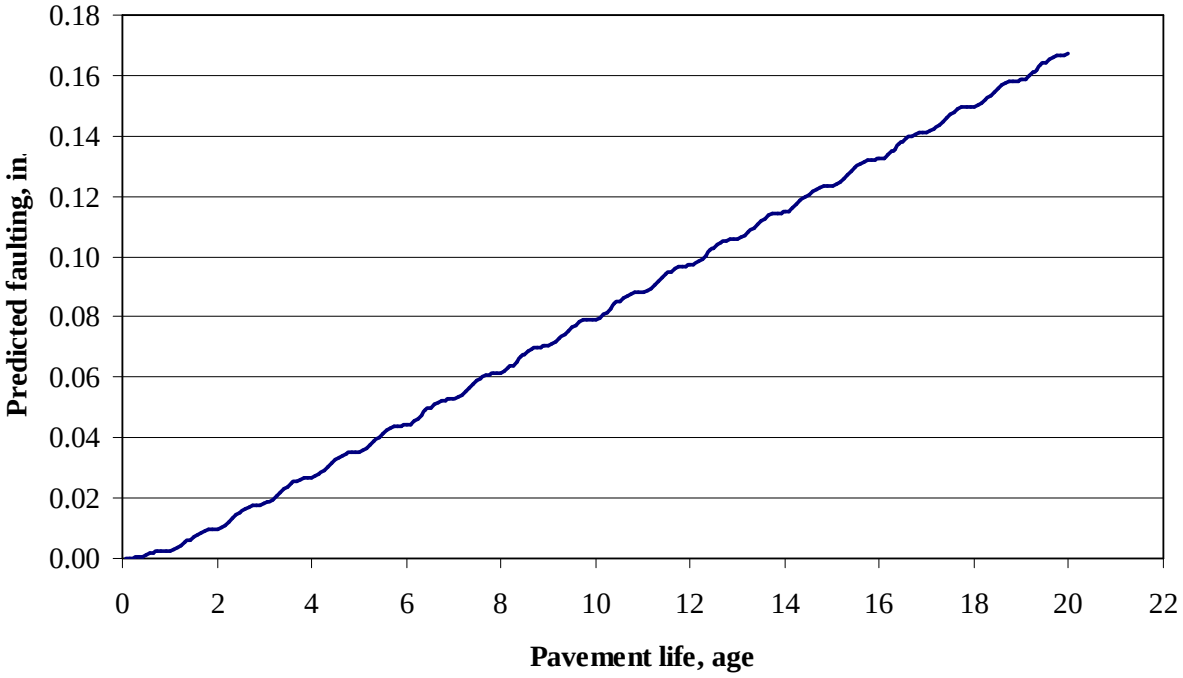

Figure 6-16: Predicted faulting for Example 4

<u>Illustrative Example 5</u> (faulting damage due to different joint designs)

Repeat Example 4 but with three of the following transverse joint designs:

- 1.5-in. dowel diameter at 12 in. center to center spacing,
- 1.25-in. dowel diameter at 18 in. center to center spacing and
- 1.5-in. dowel diameter at 18 in. center to center spacing.

Figure 6-17 illustrates the differential elastic deformation energy for the three joint designs as well as the joint design from Example 4 at the end of the design period of 20 years. It can be seen that the increase in the dowel diameter size result in a decrease in the differential elastic deformation energy, while dowel spacing has only slight impact on the differential elastic deformation energy. The predicted faulting is illustrated in Figure 6-18.

It is important to note that the variation in the joint design directly affects the slab deflections on both loaded and unloaded sides and consequently the differential elastic deformation energy. As illustrated in Figure 6-19, the decrease in the differential elastic deformation energy results in reduced faulting magnitudes.

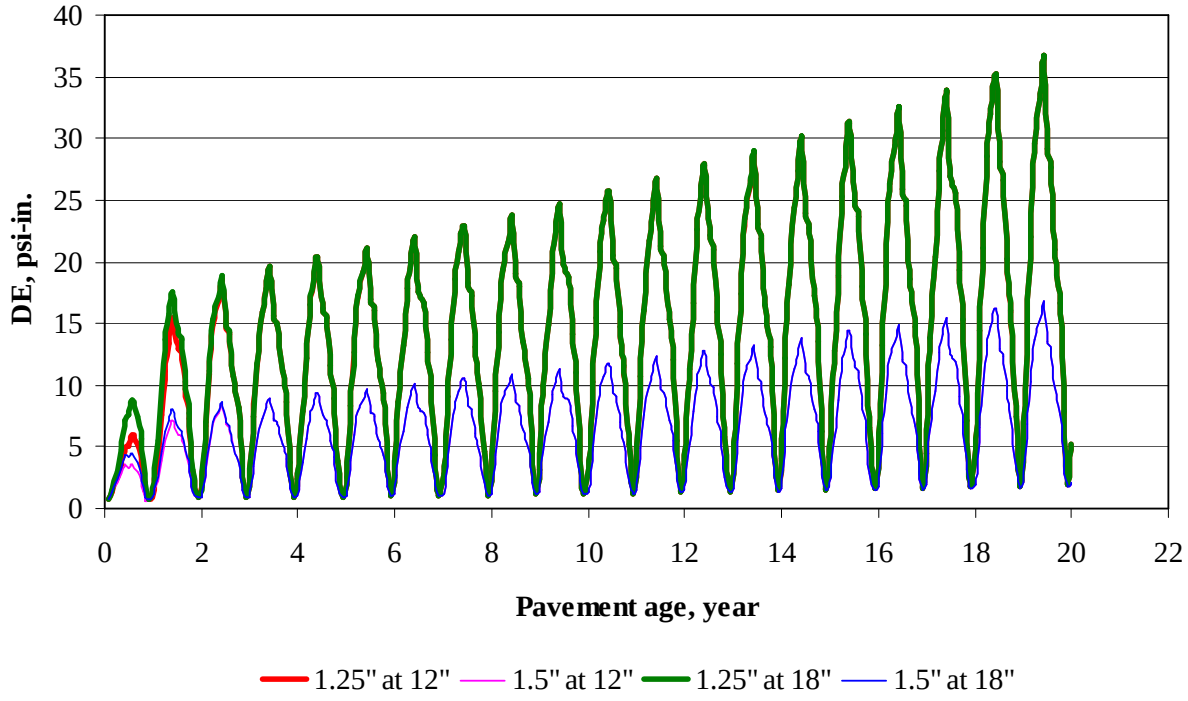

Figure 6-17: Differential elastic deformation energy for Example 5

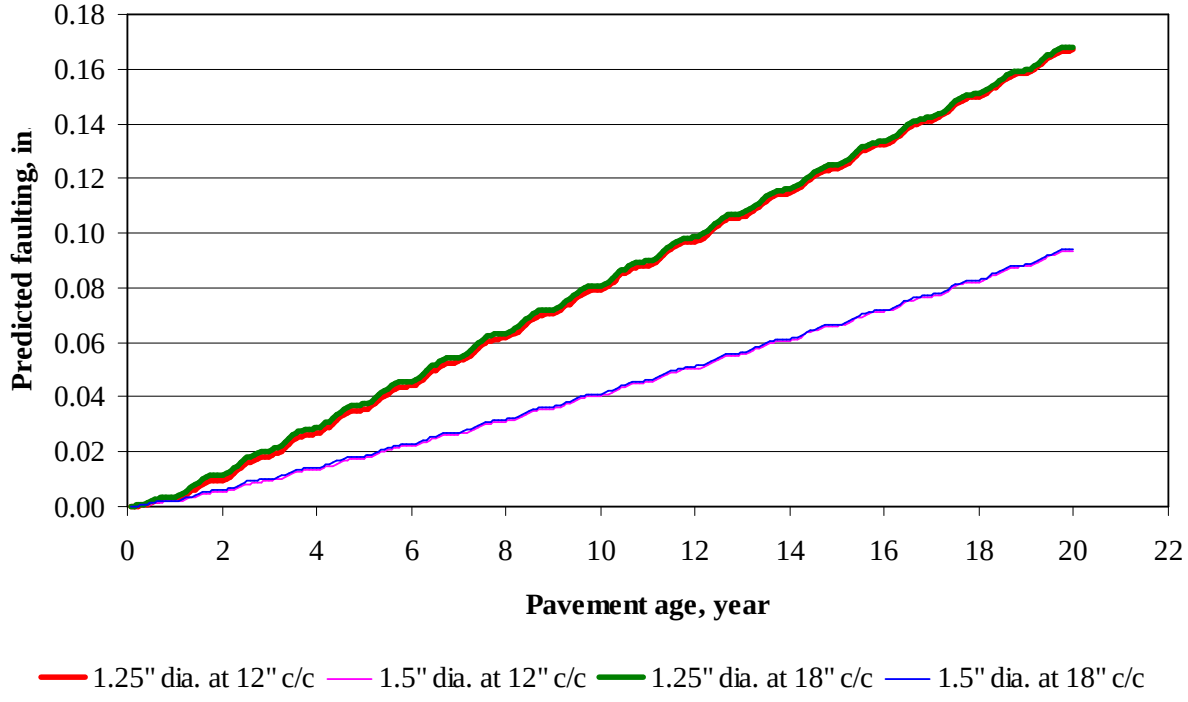

Figure 6-18: Predicted faultings for Example 5

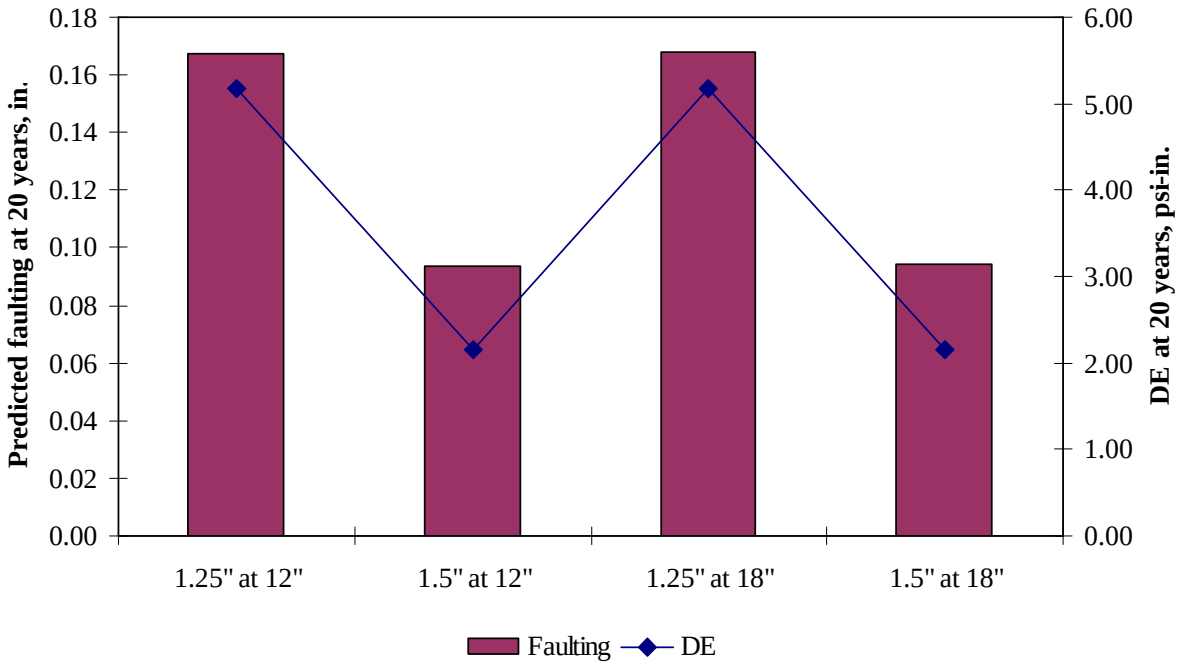

Figure 6-19: Predicted faultings and differential elastic deformation energy at the end of 20 years

<u>Illustrative Example 6</u> (faulting damage due to different base types)

Repeat Example 4 but with lean concrete base (elastic modulus of 2,000,000 psi, Poisson's ratio of 0.15 and erodibility index of 1 or "extremely resistant") and asphalt treated base (elastic modulus of 300,000 psi, Poisson's ratio of 0.30 and erodibility index of 2 or "very erosion resistant"). Then, also compare the results with Example 4, which is an aggregate base section.

Figure 6-20 illustrates the differential elastic deformation energy for the three base types. The differential elastic deformation energies for all base types were observed to be approximately equal. However, differential elastic deformation energy is not only a function of slab deflections, but also a function of modulus of subgrade reaction. In this case, the three pavement systems have different values of modulus of subgrade reaction. Therefore, the ratio of differential elastic deformation energy to modulus of subgrade reaction, DE/k, is illustrated in Figure 6-21 to eliminate the impact of modulus of subgrade reaction and focus on the slab deflections.

Predicted faulting for the three pavement systems is illustrated in Figure 6-22. It can be seen in Figure 6-23 that the level of the predicted faulting at the end of 20 years of design period corresponds to the ratio DE/k.

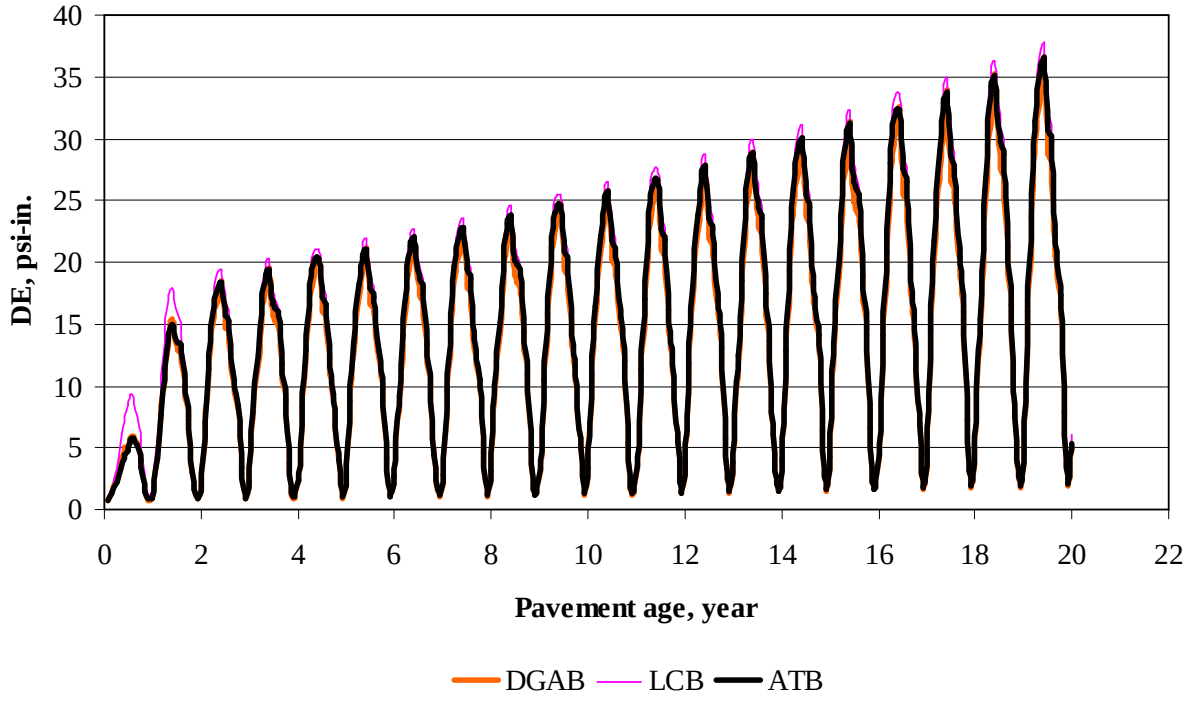

Figure 6-20: Differential elastic deformation energy for Example 6

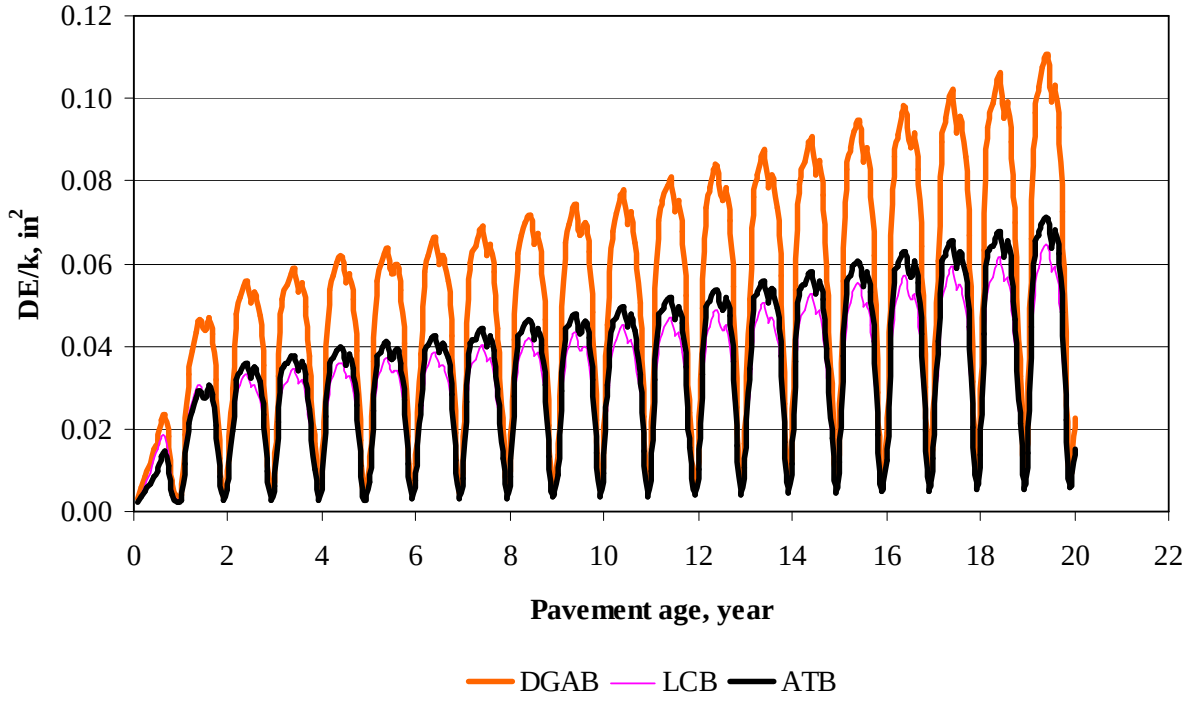

Figure 6-21: Ratio DE/k for Example 6

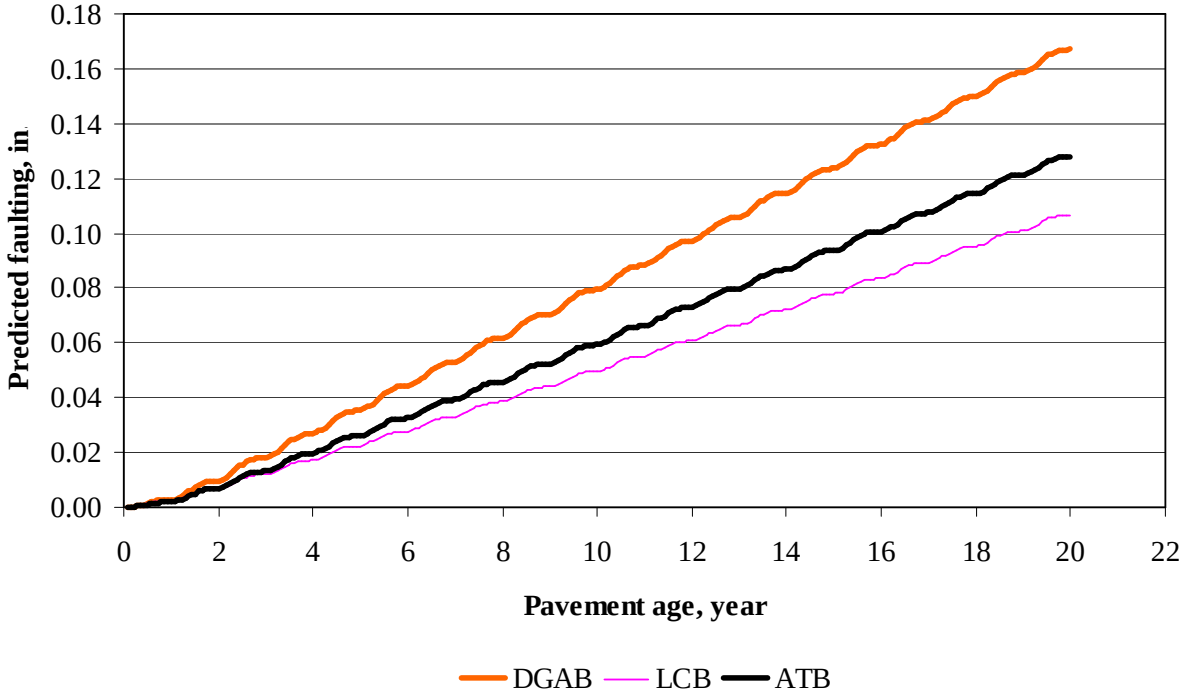

Figure 6-18: Predicted faultings for Example 6

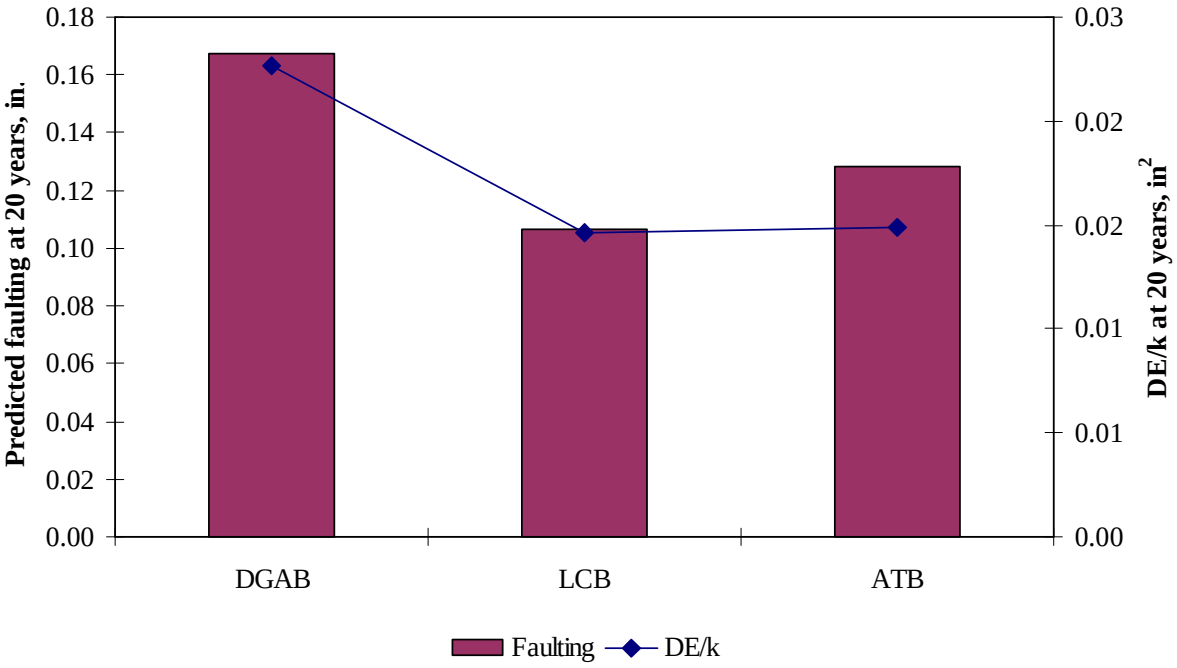

Figure 6-19: Predicted faultings and ratio DE/k at the end of 20 years

<u>Illustrative Example 7</u> (spalling damage)

Analyze percentage of joints spalled at the end of 20 years of design period for a pavement system with 3% air content, no preformed sealant, 2,000-psi compressive strength, an average of 250 freeze thaw cycles per year, 8-in. slab, and 0.45 water/cement ratio.

Scaling factor can be computed based on the given information as follows:

$$\begin{aligned} SCF &= -1400 + 350 \cdot AIR\% \cdot (0.5 + PREFORM) + 3.4 \cdot f'_c \cdot 0.4 \\ &\quad - 0.2(FTCYC \cdot AGE) + 43 \cdot h_{PCC} - 536 \cdot WC_Ratio \\ SCF &= -1400 + 350 \cdot (3) \cdot (0.5 + 0) + 3.4 \cdot (2{,}000) \cdot 0.4 \\ &\quad - 0.2(250 \cdot 20) + 43 \cdot 8 - 536 \cdot (0.45) \\ &= 947.8 \end{aligned}$$

Percentage joints spalled can be compute as follow:

$$SPALL = \left[\frac{AGE}{AGE + 0.01}\right] \cdot \left[\frac{100}{1 + 1.005^{(-12*AGE+SCF)}}\right]$$

$$SPALL = \left[\frac{20}{20 + 0.01}\right] \cdot \left[\frac{100}{1 + 1.005^{(-12*20+947.8)}}\right] = 3\%$$

Chapter VII

SUMMARY OF FINDINGS AND RECOMMENDATIONS FOR FUTURE RESEARCH

7.1 Summary of Findings

The primary objective of this research study was to conduct a preliminary parametric study to investigate the impact of the interaction between structural, environmental, and load factors on pavement responses using ISLAB2000 structural model. This was accomplished through performing structural analysis of 43,092 input combinations and the use of interpolation scheme. The secondary objective is to develop a technology transfer package that will introduce the rigid pavement analysis tools to the MDOT pavement engineers, demonstrate the versatility of the rigid pavement analysis tool and summarize a variety of pavement design scenarios in a workbook for the MDOT pavement engineers. An elaborate tutorial for the use of ISLAB2000 program and several step-by-step examples were included in the technology transfer package to fulfill this objective. The package should enable engineers to apply the ISLAB2000 program to analyze JCP systems. In addition, several MDOT designs were selected as practice problems, for which the key answers were also provided.

The analysis results of this study lead to several findings, which can be categorized into three groups: robustness and user friendliness of the ISLAB2000 program, parametric study results and interpolation scheme.

Findings Related to Robustness and User Friendliness of the ISLAB2000 Program

- The ISLAB2000 program is robust and user friendly. The results from the ISLAB2000 structural model compare well with the Westergaard solutions (after considering the relevant assumptions) and other widely accepted FE structural models.

- The variations of stresses and deflections obtained from the ISLAB2000 structural model, when using mesh size of 12 in., were found to be about 4% and 3%, respectively.

Findings Related to Parametric Study Results

- The critical load location is influenced by joint spacing and truck or axle configuration. The fractional factorial analysis indicated that the critical load location is not influenced by slab thickness, base/subbase thickness, modulus of subgrade reaction, lateral support condition, and thermal gradient or thermal strain gradient.

- For a flat slab condition, when the slab thickness changes from 9 to 12 in. the resulting stress is reduced by approximately in about 35% lower stresses. For a constant thermal gradient,

pavements constructed with different slab thickness have different temperature differentials, and therefore, the pavement responses could not be compared.

- For a flat slab condition, pavement cross-sections with thicker base/subbase thickness (from 4 to 26 in.) resulted in about 5-30% lower stresses and as the slab thickness increases the impact of base/subbase thickness becomes less significant.

- Pavements constructed with 27 feet joint spacing resulted in about 33% higher longitudinal stresses as compared to pavements constructed with 15 feet joint spacing for curled slab conditions at a thermal strain gradient value of $+10x10^{-6}$ in.$^{-1}$. The severity depends on the level of thermal curling or thermal strain gradient.

- For the load located along the wheel path (approximately 20" from the traffic stripe), pavements constructed with PCC shoulders resulted in the lowest stresses among the three lateral support conditions (12' lane with tied PCC shoulders, 12' lane with AC shoulders and 14' lane with AC shoulders) that are considered in the study. Although the pavements were constructed with the same AC shoulder, the magnitudes of longitudinal stresses for pavements with 12-ft lane (standard lane) were higher than that for pavements with 14-ft lane (widened lane). As the wheel path shifted 2 ft towards the centerline for pavements with widened lane, a pseudo-interior loading condition was created, resulting in the reduction of stresses from edge loading. Pavements constructed with AC shoulders (12-ft lane with AC shoulder) resulted in about 13% and 9% higher longitudinal stress values than pavements constructed with PCC shoulder (12-ft lane with tied PCC shoulder) and widened lane (14-ft lane with untied AC shoulder), respectively.

- Lateral wander (or lateral placement) of traffic load resulted in about 10% and 30% higher edge stresses as the load moves from the wheel path towards longitudinal joint (lane/shoulder joint) for tied PCC shoulder and AC shoulder, respectively.

Findings Related to Interpolation Scheme

- In the validation process considering all axle types, the bias (average error), variance, and mean square of errors (MSE) of the best scheme (scheme 16) were 0.51 psi, 8.63 psi^2, and 8.89 psi^2, respectively, indicating that the interpolation scheme was highly accurate and precise in computing pavement response as compared with the results directly obtained from the ISLAB2000 program.

- If only single, tandem and tridem axles were considered, the bias, variance and MSE of the best scheme were found to be 0.02 psi, 3.38 psi^2, and 3.38 psi^2, respectively.

7.2 Recommendations for Future Research

This research study focuses on pavement responses and several factors that affect them. Although pavement response plays a significant role in the mechanistic-empirical design process, it is necessary to integrate the pavement response with several other components in order for it to become practical. Pavement responses need to be used an inputs to transfer function, which relate responses to performance. However, the transfer function coefficients need to be localized and therefore it is important to ensure the constants reflect climatic and loading conditions in Michigan. Calibration process also needs to take place to ensure MDOT policies are met in the calculation process. The following research topics are recommended:

1) The CTE values for concrete mixes and also aggregate (as concrete making material) used in paving Michigan roads need to be determined and cataloged, since CTE plays a critical role in the thermal analysis of jointed concrete pavements. The slab movement and joint opening are also influenced by the CTE of concrete.

2) An extensive traffic database, e.g. WIM database, should be made available for the pavement network as hourly axle spectra is a key input for damage computations. The hourly axle spectra allow for calculation of pavement responses that account for daily and seasonal conditions of climate, roadbed and material. The axle repetitions from the axle spectra and the corresponding pavement responses are the inputs to the cumulative damage calculation.

3) Develop and calibrate transfer functions for key jointed concrete pavement distresses that reflect Michigan practice. The process involves statistical correlation of the cumulative damages to the measured distresses corresponding to the time periods to obtain a calibrated model that can be used for Michigan jointed concrete pavement design.

REFERENCES

American Association of State Highway and Transportation Officials (AASHTO). AASHTO Guide for Design of Pavement Structures. Washington, DC, USA, 1993.

Armaghani, J.M; Larsen, T.J; Smith, L.L. Temperature Response of Concrete Pavements. Transportation Research Record 1121, TRB, National Research Council, Washington, DC, USA, 1987, pp. 23-33.

Channakeshava, C.; Barzegar, F.; Voyiadjis, G.Z. Nonlinear FE analysis of plain concrete pavements with doweled joints. Journal of Transportation Engineering, v 119, n 5, American Society of Civil Engineers, New York, NY, USA, 1993, pp. 763-781.

Crovetti, J. A.; Darter, M. I. Void detection for jointed concrete pavements. Transportation Research Record 1041, TRB, National Research Council, Washington, DC, USA, 1985, pp. 59-68.

Darter, M.I; Hall, K.T; Kuo, C. Support Under Concrete Pavements. University of Illinois, Urbana-Champaign, Illinois, USA, 1994.

Darter, M; Khazanovich, L; Snyder, M; Rao, S; Hallin, J. Development and Calibration of a Mechanic Design Procedure for Jointed Plain Concrete Pavements. 7th International Conference on Concrete Pavements, Orlando, FL, USA, 2001.

Davids, W.G.; Mahoney, J.P. Experimental verification of rigid pavement joint load transfer modeling with EverFe. Transportation Research Record 1684, TRB, National Research Council, Washington, DC, USA, 1999, pp. 81-89.

Huang, Y.H. Pavement Analysis and Design. Prentice-Hall, Englewood, NJ, USA, 1993.

Ioannides, A.M.; Thompson, M.R.; Barenberg, E.J. Westergaard solutions reconsidered. Transportation Research Record 1043, TRB, National Research Council, Washington, DC, USA, 1985, pp. 13-23.

Khazanovich, L.; Yu, H.T. Modeling of jointed plain concrete pavement fatigue cracking in PaveSpec 3.0. Transportation Research Record 1778, TRB, National Research Council, Washington, DC, USA, 2001, pp. 33-42.

Khazanovich, L; Darter, M.I.; Yu, T. Mechanistic-empirical for transverse joint faulting prediction. Presented at the 83rd Annual Meeting of the TRB, Washington, DC, USA, 2004.

Michigan Center for Truck Safety. Truck driver's guidebook, 6th edition. Michigan Center for Truck Safety, Lansing, MI, USA, 2001.

Mirambell, E. Temperature and Stress Distributions in Plain Concrete Pavements Under Thermal and Mechanical Loads. 2nd International Workshop on the Theoretical Design of Concrete Pavements, Siquenza, Spain, 1990.

NCHRP. Calibrated Mechanistic Structural Analysis Precedures for Pavement. NCHRP 1-26, Vol. 1, Final Report; Vol. 2, Appendices, University of Illinois, Urbana-Champaign, Illinois, USA, 1990.

Oh, B.H. Cumulative damage theory of concrete under variable-amplitude fatigue loadings. ACI Materials Journal, v 88, n 1, American Concrete Institute, Detroit, MI, USA, 1991, pp. 41-48.

Rao, C; Barenberg, E.J; Snyder, M.B; Schmidt, S. Effects of Temperature and Moisture on the Response of Jointed Concrete Pavements. 7th International Conference on Concrete Pavements, Orlando, FL, USA, 2001.

Rao, C; Selezneva, O; Darter, M.I. Calibration of a mechanistic empirical performance model for CRCP punchouts. Presented at the 83rd Annual Meeting of the TRB, Washington, DC, USA, 2004.

Strategic Highway Research Program. Specific pavement studies experimental design and research plan for experiment SPS-2 strategic study of structural factors for rigid pavements. National Research Council, Washington, DC, USA, 1990.

Tabatabaie, A.M.; Barenberg, E.J. Structural analysis of concrete pavements systems. Journal of Transportation Engineering, v 106, n 5, American Society of Civil Engineers, New York, NY, USA, 1980, pp. 493-506.

Tayabji, S.D.; Colley, B.E. Improved rigid pavement joints. Transportation Research Record 930, TRB, National Research Council, Washington, DC, USA, 1983, pp. 69-78.

Ullidtz, P. Pavement Analysis. Elsevier, New York, NY, USA, 1987.

Westergaard, H.M. Stresses in concrete pavements computed by theoretical analysis. Public Road, v 7, 1926, pp. 25-35.

Yu, T.; Khazanovich, L.; Darter, M.I. Consideration of JPCP curling and warping in the 2002 Design Guide. Presented at the 83rd Annual Meeting of the TRB, Washington, DC, USA, 2004.